BIOMEDICAL APPLICATIONS OF NITRIC OXIDE PRODUCTION SYSTEM IN THE PROMOTION OF CARDIOVASCULAR HOMEOSTASIS AND BONE REGENERATION

RAO JINGDONG

PhD

The Hong Kong Polytechnic University

2024

The Hong Kong Polytechnic University
Department of Biomedical Engineering

Biomedical applications of nitric oxide production system in the promotion of cardiovascular homeostasis and bone regeneration

RAO Jingdong

A thesis submitted in partial fulfilment of the requirements for the degree of Doctor of Philosophy

Aug 2023

CERTIFICATE OF ORIGINALITY

I hereby declare that this thesis is my own work and that, to the best of my knowledge and belief, it reproduces no material previously published or written, nor material that has been accepted for the award of any other degree or diploma, except where due acknowledgement has been made in the text.

_____ (Signed)

RAO Jingdong (Name of student)

Abstract

Nitric oxide (NO) is a ubiquitous, bioactive gas that plays a crucial role in various biological systems. However, inadequate NO levels are associated with various disease complications. Therefore, the introduction of NO into a therapeutic system has great potential for disease treatment. In this dissertation, we propose three projects focused on cardiovascular stent and bone scaffold with NO-generating and releasing capabilities.

The first project aimed to address the inadequate NO donors (RSNO) *in vivo*, which may impair catalytic NO generation by glutathione peroxidase (GPx)-like substances such as copper (Cu). GPx has peroxidase activity and can decompose endogenous RSNO to NO. Similarly, Cu(II) can be reduced into Cu(I) to then decompose RSNO. Therefore, Cu has GPx-like properties in catalyzing NO production. To maintain cardiovascular homeostasis, we constructed an endothelium-mimicking coating (DCAH) on the surface of cardiovascular stent. The nanometer-thin coating consisted of a dopamine-copper (DC) network with immobilized L-arginine and glycocalyx heparin. The coating could catalyze NO generation in the presence of endogenous RSNO. The arginine served as an NO precursor to release NO by endothelial nitric oxide synthase (eNOS), guaranteeing sufficient NO supply when RSNO were not present. Furthermore, the introduction of heparin could increase the eNOS level, which facilitated arginine decomposition into NO. The long-term and sufficient NO production could inhibit smooth muscle cells (SMC) growth as well as platelet adhesion, combating stent thrombosis and restenosis.

The second project aimed to address the slow re-reendothelialization after stenting. Building on the results of the first project, we found that a sufficient number of (endothelial cells) ECs grown on the material could spontaneously produce NO. Moreover, the pathological progression after endothelial destruction also calls for rapid EC adhesion to facilitate re-reendothelialization. Therefore, we grafted vascular endothelial growth factor (VEGF) onto DCAH to prepare an AHV coating. In this system, VEGF promoted EC adhesion at the early stage, which spontaneously produced NO and formed an uncompromised endothelium on the stent surface. The AHV stent

coating targeted vascular repair phases to further promote rapid reendothelialization, long-term inhibition of platelet adhesion and SMC migration and proliferation.

The third project addressed the challenge of coordinating both osteogenesis and angiogenesis as well as rebuilding a bone microenvironment rich in various active molecules such as VEGF, NO, and bone morphogenetic protein-2 (BMP-2). Inspired by the second project, where a stent could capture cells for reendothelialization, we designed a triply periodic minimal surface (TPMS) scaffold with N-Cadherin (N-CAD) and TPSLEQRTVYAK peptide (TPS) coatings to attract endothelial progenitor cells (EPCs) and bone mesenchymal stem cells (BMSCs), respectively. This scaffold recreated a bone-friendly environment by spontaneously producing NO, VEGF and BMP-2 from the adherent cells through paracrine effects. The captured cells could undergo differentiation to promote osteogenesis and angiogenesis, thus facilitating bone regeneration.

In summary, we have developed a series of NO production platforms based on the bio-functions of NO in the cardiovascular system and bone tissues. These platforms aim to reshape a healthy microenvironment and ultimately improve therapeutic outcomes in cardiovascular intervention and bone tissue engineering.

List of Publications

1. **Jingdong Rao**,‡ Xiaohui Mou,‡ Yongyi Mo, Ho-Pan Bei, Li Wang, Chuyang Y. Tang, Kai-Hang Yiu, Zhilu Yang,* Xin Zhao*. Gas station in blood vessels: an endothelium mimicking, self-sustainable nitric oxide fueling stent coating for prevention of thrombosis and restenosis, Biomaterials, 2023, accepted.
2. **Jingdong Rao**,‡ Di Suo,‡ Qing Ma,‡ Yongyi Mo, Ho-Pan Bei, Li Wang, Chuyang Y. Tang, Kai-Hang Yiu, Zhilu Yang,* Xin Zhao*. Riding a vascular time train to spatiotemporally attenuate thrombosis and restenosis by double presentation of therapeutic gas and biomacromolecules. Under revision.
3. Yuhe Yang,‡ **Jingdong Rao**,‡ Huaqian Liu,‡ Zhifei Dong, Zhen Zhang, Ho-Pan Bei, Chunyi Wen, Xin Zhao. Biomimicking design of artificial periosteum for promoting bone healing[J]. Journal of Orthopaedic Translation, 2022, 36: 18-32.
4. Di Suo,‡ **Jingdong Rao**,‡ Haimang Wang, Ziheng Zhang, Polly Hang-Mei Leung, Hongyu Zhang, Xiaoming Tao, Xin Zhao. A universal biocompatible coating for enhanced lubrication and bacterial inhibition[J]. Biomaterials Science, 2022, 10(13): 3493-3502.
5. Quanjing Mei,‡ **Jingdong Rao**,‡ Ho Pan Bei, Yaxiong Liu, and Xin Zhao*.3D Bioprinting Photo-Crosslinkable Hydrogels for Bone and Cartilage Repair. International Journal of Bioprinting, 2021, 7(3).

* Corresponding author

‡ These authors contributed equally

Acknowledgements

First and foremost, I would like to express my heartfelt appreciation to my supervisor, Dr. Xin ZHAO, whose guidance has been instrumental in shaping my academic life. Under Dr. ZHAO's supervision, I have cultivated the invaluable skill of independent thinking and significantly bolstered the rigor of my scientific research. Furthermore, my sense of responsibility and aptitude for teamwork have undergone remarkable improvement. Moreover, Dr. ZHAO has been an unwavering source of support in my scientific endeavors, she often shares intriguing studies and engages us in stimulating discussions about fresh ideas and experimental designs. Additionally, Dr. ZHAO's support and encouragement for female researchers have been truly inspiring, serving as a compelling role model for me and it is a true honor to be a student of Dr. ZHAO.

Furthermore, I would like to extend my sincere thanks to every member in Dr. ZHAO's research group. Firstly, I am immensely grateful to Dr. Yuhe YANG for his invaluable advice for my project and encouragement in my study. I would like to express my gratitude to Mr. Tianpeng XU, whose guidance has been instrumental in navigating my experiments. Miss Di SUO's assistance in both my experiments and daily life has been invaluable, and I am sincerely thankful for her unwavering support. I'd like to thank Mr. Shang LV and Mr. Huaqian LIU for their valuable advice towards the experimental designing. Likewise, Dr. Quanjing MEI's guidance in TA work have equipped me with the skills to fulfill my duties. I am deeply indebted to Mr. Bei Ho PAN for his guidance and assistance in my writing endeavors. Additionally, Miss Yongyi MO's support in my experiments has been greatly appreciated. I would like to acknowledge the contributions of Mr. Shuai ZHAO, Miss Xintong ZHOU, Mr. Zhenhua CHEN, Mr. Ho Yin YUEN, Mr. Chun Hei LAM, Miss Ching Yui WONG, Miss Maria Gan and Miss Shanshan ZHANG, who have been instrumental in both my experiments and lab life. Interacting with students from diverse research backgrounds has truly broadened my horizons, and I feel privileged to have had the opportunity to know such remarkable friends.

Moreover, I would like to express my gratitude to Prof. Zhilu YANG from

Dongguan Key Laboratory of Smart Biomaterials and Regenerative Medicine, The Tenth Affiliated Hospital of Southern Medical University for his invaluable support on my project. I would also like to express my appreciation to his students, Mr. Xiaohui MOU and Mr. Qing MA, for their assistance in the animal experiments. Furthermore, I am deeply thankful to the Prof. Huaiyu WANG from Shenzhen Institutes of Advanced Technology, Chinese Academy of Sciences and his student Miss. Qing LIAO, for their support and contributions to the animal experiments.

I am deeply grateful to my parents and relatives for their unwavering care and support throughout my academic journey. Your unconditional support has served as my strongest foundation and provided me with endless power. I extend my heartfelt appreciation to you all for being my source of comfort and encouragement. Furthermore, I would like to express my sincere thanks to my friends and roommates, Miss. Xiaoyan WU, Dr. Xiaoyi YANG, and Miss Junyu CHEN. During the most challenging times of the epidemic, your remarkable support and encouragement have been instrumental in dispelling feelings of loneliness and making me feel a sense of belonging.

Lastly, I would like to appreciate all the professors who generously dedicated your valuable time to review my thesis and participate in the oral defense. Your valuable advice and guidance help me in my academic life.

Table of Contents

List of Abbreviations

Abbreviation	Full name
316L SS	316L stainless steel
3D	Three-dimensional
ALP	Alkaline phosphatase
ANG	Angiogenin
ARS	Alizarin Red S
ATR-FTIR	Attenuated total reflection Fourier transform infrared spectroscopy
AV	Arteriovenous
BCIP/NBT	5-bromo-4-chloro-3-indolyl-1-phosphate and nitroblue tetrazolium
BMP	Bone morphogenetic protein
BMP-2	Bone morphogenetic protein-2
BMSCs	Bone mesenchymal stem cells
Ca^{2+}	Calcium ion
Calcein-AM	Calcein acetoxymethyl ester
CCK-8	Cell counting kit-8
CD31	Cluster of differentiation 31
cGMP	Cyclic guanosine phosphate
CLSM	Confocal laser scanning microscope
Cu	Copper
CVD	Cardiovascular disease
CVS(s)	cardiovascular stent(s)
Cy5	Cyanine 5
DA	Dopamine
DAF-FM DA	3-Amino,4-aminomethyl-2',7'-difluorescein diacetate
DAPI	4’,6-diamidino-2-phenylindole

DBCO	Dibenzocyclooctyl
EC(s)	Endothelial cell(s)
ECM	Extracellular matrix
ECM	Endothelial cell culture medium
EDC	N-(3-dimethylaminopropyl)-N-ethylcarbodiimide
EDX	Energy-dispersed X-ray
ELISA	Enzyme-linked immunosorbent assay
eNOS	Endothelial nitric oxide synthase
EPCs	Endothelial progenitor cells
EPR	Electron paramagnetic resonance
Fg-γ	Fibrinogen gamma chain
FITC	Fluorescein isothiocyanate
FN	Fibrinogen
FXa	Factor Xa
Gal	Galactosidase
GelMA	Gelatin methacrylate
GPx	Glutathione peroxidase
GSH	Glutathione
GSNO	S-nitrosoglutathione
GSSG	Glutathione disulfide
HD	Hexamethylene diamine
HRP	Horseradish peroxidase
HUASMCs	Human umbilical artery smooth muscle cells
HUVECs	Human umbilical vein endothelial cells
iNOS	Induced NOS
L-NMMA	NG-Monomethyl-L-arginine acetate
MALDI-TOF	Matrix assisted laser desorption/ionization-time of flight mass spectrometer
MES	2-(N-morpholino) ethanesulfonic acid hydrate

Micro-CT	Micro-computed tomography
N3	Azide
NADPH	Nicotinamide adenine dinucleotide phosphate
N-CAD	N-Cadherin peptide
nHAMA	Hydroxyapatite methacrylate nanoparticles
NHS	N-hydroxysuccinimide
NIR	Near infrared
nNOS	Neuronal NOS
NO	Nitric oxide
NONOates	N-diazeniumdiolates
NOS	Nitric oxide synthase
OCN	Osteocalcin
PA	Peptide amphiphile
PBS	Phosphate-buffered saline
PDA	Polydopamine
PI	Pyridine iodide
PPP	Platelet-poor plasma
PRP	Platelet-rich plasma
PVC	Polyvinyl chloride
QCM-D	Quartz crystal microbalance with dissipation equipment
qRT-PCR	Quantitative reverse transcription-polymerase chain reaction
RGD	Arginine-glycine-aspartic acid
RNA	Ribose nucleic acid
RSNOs/SNO	S-nitrosothiols
Runx2	Runt-related transcription factor 2
Se	Selenium
SEM	Scanning electron microscopy
sGC	soluble guanylyl cyclase
SMC(s)	Smooth muscle cell(s)

SNAP	S-nitroso-N-acetylpenicillamine
TMB	3,3′,5,5′-tetramethylbenzidine solution
TPMS	Triply periodic minimal surface
TPS	TPSLEQRTVYAK peptide
Tris-HCl	tris-(hydroxymethyl)-aminomethane hydrochloride
TRITC	Tetramethylrhodamine-isothiocyanate
UPEA	Unsaturated polyester amide
UV	Ultraviolet
VEGF	Vascular endothelial growth factor
VWF	Von Willebrand factor
WCA	Water contact angle
Wnt	Wingless-related integration site
XPS	X-ray photoelectron spectroscopy
ZnO	Zinc oxide
β-TCP	β-tricalcium phosphate

Chapter 1 Introduction

1.1 Brief introduction of NO

NO is a gas molecule that is colorless, non-irritating, chemically active but has a very short half-life (3-5 s).[1] It was first believed that NO was caused by natural (such as lightning) and industrial (such as fossil fuels) activities, and people defined it as a harmful gas that destroys the atmosphere, pollutes the environment, and even induces cancer.[2, 3] However, the passage of time has unveiled the enormous therapeutic potential of NO. In 1986, Robert Furchgott and Louis Ignarro first proposed that NO is a potential source of relaxation factors, which opened up a broad new research field.[4] Thus, NO was the first gas molecule to be recognized as a signaling medium in living organisms, followed by more and more scientists exploring the physiological applications of NO.[5] In 1992, NO was recognized the top achievement of "Molecule of the Year" by *Science*.[6] In 1998, the Nobel Prize in Physiology or Medicine was awarded to Robert Furchgott, Ferid Murad and Louis Ignarro for their discovery that NO is a relaxing factor obtained from endothelium. Along with the boom in NO research, people have realized that NO has an irreplaceable role in the cardiovascular, nervous, immune, respiratory and digestive systems.[7-11]

In mammals, NO is endogenously generated by two pathways. The main route depends on NO synthase (NOS) and is known as the L-arginine-NOS-NO pathway. NOS includes endothelial NOS (eNOS), neuronal NOS (nNOS) and induced NOS (iNOS), which are widely present in ECs, macrophages, neurophagocytes and nerve cells (Fig. 1-1A).[12, 13] Under the influence of nicotinamide adenine dinucleotide phosphate (NADPH) and oxygen , NOS can mediate oxidative processes to convert Arginine into NO.[14] Another NO generation pathway is NOS-independent (nitrate-nitrite-NO pathway), which is mainly regulated by diet such as green vegetables (Fig. 1-1B).[15] After eating, facultative anaerobic bacteria on the tongue convert nitrate to nitrite, which is further reduced into NO by acidic environment and several proteins.[16] All in all, these NO generation routes maintain the stable state of this reactive molecule, thus regulating the physiological homeostasis of human body.

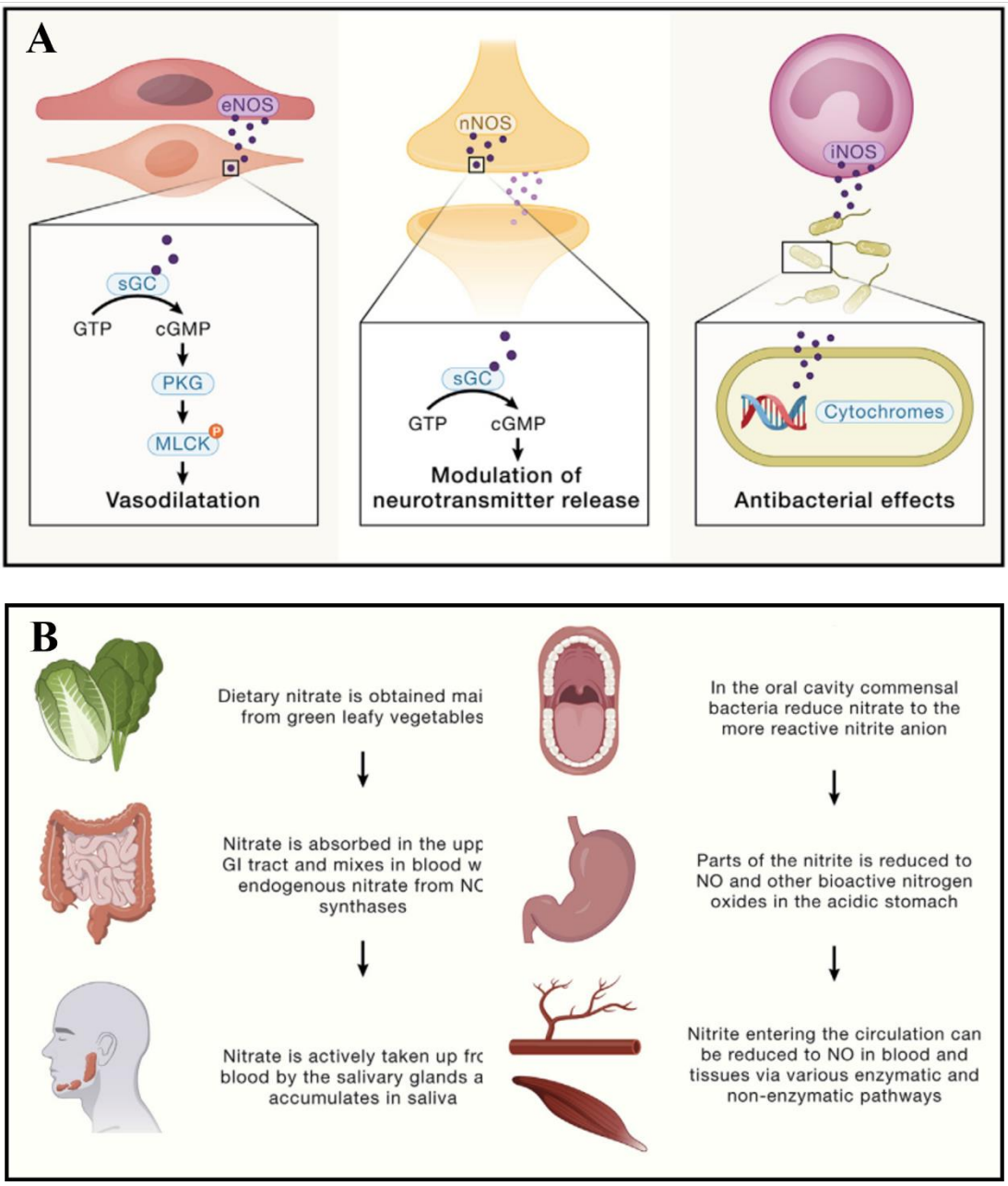

Fig. 1-1. NO production from (A) NOS-dependent pathway and (B) the nitrate-nitrite-nitric oxide pathway. Figures are reproduced from Ref. [17] with permission. Copyright 2022, Elsevier.

1.2 Physiological functions of NO

Due to being a free radical, NO has a broad range of biological reactivities with prosthetic groups, deoxyribonucleic acid (DNA), oxygen, superoxide, and transition metals.[18] NO exerts its physiological effects through cyclic guanosine phosphate (cGMP)-dependent and independent mechanisms. The cGMP-dependent pathway plays a critical role in many cell types by mediating local and systemic signaling, and regulating various physiological functions such as cell proliferation, apoptosis, anti-bacterial defense, intestinal peristalsis, muscle relaxation, bone tissue growth, platelet adhesion, and vascular dynamics (Fig. 1-2), etc.[19] Meanwhile, NO's reactivity with superoxide, oxygen, thiols, and transition metals (e.g., iron and zinc) results in an independent pathway that regulates immune responses, maintains normal cell metabolism, and sustains redox homeostasis, etc.[20] Overall, as a gas transmitter, NO has broad physiological effects like fighting off infection, inflammation, platelets, thrombosis, while facilitating vascular protection and relaxation, wound healing, osteogenesis and even treatment of cancer.[21]

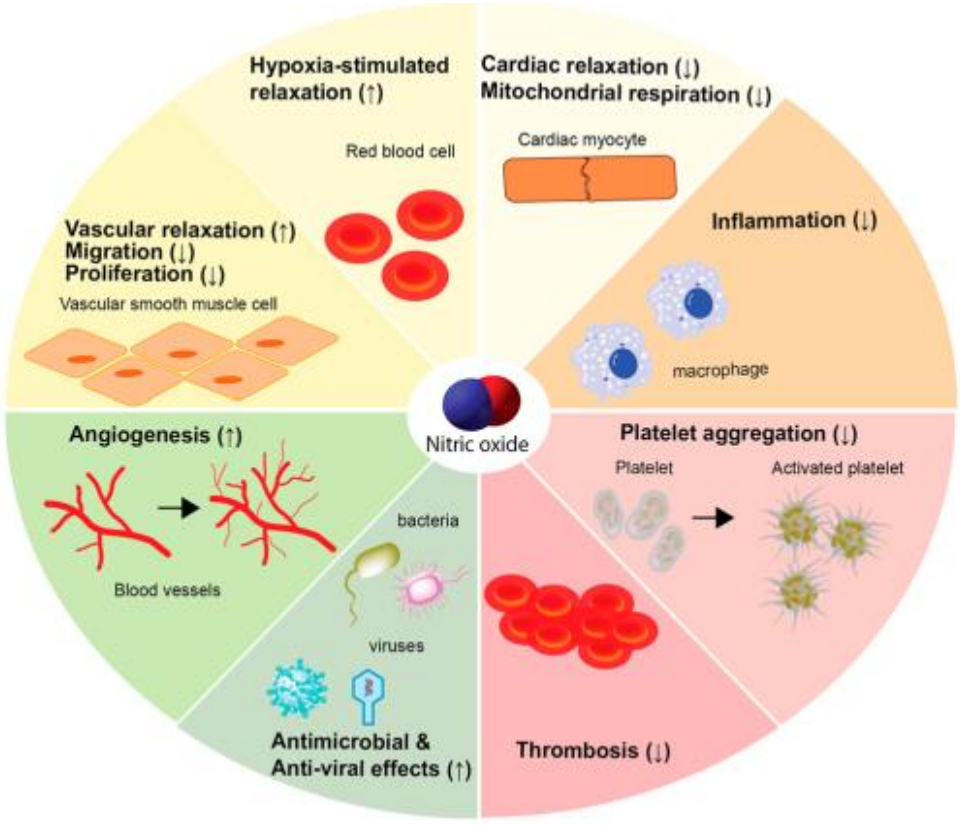

Fig. 1-2. Physiological functions of NO. NO have a wide range of physiological effects

such as the thrombosis inhibition, anti-inflammatory, antibacterial, vascular relaxation, angiogenesis, etc. Figure is adapted with permission from Ref. [22]. Copyright 2021, American Chemical Society.

1.2.1 Cardiovascular homeostasis

The cardiovascular system stands as the "typical NO-dependent system" because the physiological effect of NO was discovered by vascular endothelial experiments, and the first drug to treat angina pectoris, nitroglycerin, was a typical NO donor.[23] The cardiovascular system depends heavily on eNOS-induced NO generation to keep blood pressure and blood flow at normal levels, thereby mediating vessel remodeling. The generated NO also regulate activities of SMCs, platelet, leukocyte and immune cells.[24, 25] For example, NO produced from vascular ECs can diffuse into SMCs and activate cGMP pathway, which promotes the smooth muscle relaxation and dilates blood vessels.[26] Cardiovascular diseases can impair endothelial homeostasis, and the oxidative stress will damage NOS system, leading to dysfunction of endothelium and reducing NO amount and its bioavailability.[27, 28]

1.2.2 Bone repair

NO can affect the local release of cytokines, increase osteoblast proliferation, osteocalcin synthesis as well as mineralized matrix formation during bone growth and repair.[29] Studies have shown significant iNOS expression within 24 h after fracture, attracting bone cells to the injured site and starting the repair process. Subsequently, eNOS expression is elevated in bone cells and ECs in lesion site, thereby increasing blood supply.[30] The two main mechanisms for the ongoing remodeling of bone tissue are bone remodeling and bone resorption, which can maintain bone health and repair bone microdamage. NO can also control bone resorption through reducing osteoclast activity and promote bone formation via improving osteogenesis.[31] In addition, NO is a key mediator of osteogenic differentiation following exercise and mechanical stimulation. Bone marrow cells and osteoblasts can release NO under the influence of

flow and shear stress, leading to osteoblast stimulation.[32]

1.2.3 Others

Other than cardiovascular function and bone growth, NO can influence many diseases and conditions including cancer and wounds. NO has a complex effect in cancer, as the concentration of NO determines whether it is a tumor promoter or suppressor.[33] High NO concentrations lead to reactive nitrogen, which can interact with reactive oxygen to cause nitrosation, resulting in impairment of DNA, enzymes, and cellular functions.[34] Conversely, low NO concentrations increase anti-apoptotic ability of cancer cells and promote vascularization, thereby facilitating nutrient transportation and promoting tumor growth.[35] In addition, NO is crucial for the regulation of the wound healing process.[36] In the inflammation stage, NO influences immune responses. During the proliferative phase, NO-dependent keratinocyte and fibroblast proliferations promote re-epithelialization and collagen deposition.[37] Furthermore, NO plays a crucial function in angiogenesis by encouraging EC migration and proliferation.[38] Studies have demonstrated that the decline in endogenous NO production caused by extensive infection and insufficient blood supply can lead to delayed wound healing.[39] Hence, supplementing NO to the wound lesion is a promising therapeutic approach.

As mentioned above, NO has many physiological functions. As a gas transmitter, NO can freely permeate cell membranes to directly exert therapeutic effects to targeted sites. However, given that NO has an extremely short half-life (i.e., seconds), its influence range is only limited to about 100 μm,[40] an effective NO-based therapy must deliver to a specific site, keep NO stable, and control the NO concentration as well as its release rate for a sustained period.

1.3 NO production pathways

Controlled NO release has grown to be a popular subject in regenerative medicine, and the incorporation of NO-producing moieties into biomedical materials will serve as a functional platform for various disease therapies. Normally, NO production strategies can be divided into NO release and NO generation, where NO-releasing substance (e.g., NO donor) can serve as a limited storage, while NO generation uses catalytic species or genetic engineering to achieve endogenous NO supply. These NO production strategies can deliver and maintain physiological NO concentrations at specific sites.

1.3.1 NO release strategy

For NO release, small molecules or nanocarriers can pre-load NO and then release it automatically or under control at the targeted site.[41-43] NO donors are the most commonly approaches to locally transport and discharge NO via means such as enzymatic cleavage, pH response, temperature, light or metal catalysis.[44] Currently, common NO donors include nitriles, metal-nitroso complexes, N-diazeniumdiolates (NONOates), and s-nitrosothiols (RSNOs/SNOs). NONOates can be prepared by compressing NO gas with secondary amine elements at 5 atm pressure; under physiological circumstances, they spontaneously decompose to release two molecules of NO per donor.[45] Due to the ease of characterization and modification, NONOates have become the most attractive NO donors. Meanwhile, RSNO is an endogenous NO transporter that can maintain the balance of NO *in vivo*.[46] Inspired by RSNOs, researchers have synthesized RSNO-like compounds by reacting NO_2, N_2O_4 or N_2O_3 with thiol-substances.[47, 48] The two most commonly used stable synthetic RSNOs include s-nitrosoglutathione (GSNO) and S-nitroso-N-acetylpenicillamine (SNAP), whose NO release activities depend on heat, light and metal catalysis.[49]

Because heat, acid or physiological conditions (such as oxidative stress) can decompose NO donors, researchers have developed enzyme-based therapy with NO prodrugs to ensure NO donor stability and controlled release.[50] Such prodrugs are fabricated by linking NO donors with enzyme-sensitive ligands to remain stable in

normal condition, but trigger NO release when a specific enzyme is present. For example, Wang et al. synthesized glycosylated NONOate (Gal-NONOate) and designed a surface coating of galactosidase (Gal), which can be used on various medical materials. After *in vivo* implantation, the NO prodrug was injected intravenously, and after it circulated to the implant site, the enzyme catalyzed the breakdown of Gal-NONOate to release NO *in situ*.[51] In another study, Matson et al. proposed a matrix metalloprotease-2 (MMP-2)-sensitive, NO-releasing peptide, which consisted of NO-donating residues. The peptide had a burst NO release in 2 days, then slowly over the course of 30 days.[52]

Although NO donors are convenient, their long-term therapeutic effects are not satisfactory because they have relatively low NO flux, and their instability greatly limits long-term use. Although prodrugs have improved the stability of NO donors, the large dose of systemic administration poses a potential risk of side effects. Most importantly, NO donors can only provide a depletable NO reservoir. Therefore, there is a need to achieve a reliable long-term and sufficient NO supply.

1.3.2 NO generation strategy

To overcome the drawbacks of NO release strategies, researchers have developed NO-generating elements that leverage the continuous supply of endogenous NO sources to achieve long-term effects.

In the cardiovascular system, NOS determines NO generation. Among them, eNOS promotes NO production from ECs,[53] whereas iNOS is rarely found in the vasculature under normal physiological circumstances, but can produce considerable NO amounts over a long time once its expression is enhanced.[54] Many researchers have investigated NOS-related gene therapy. In a study, DiMuzio et al. used eNOS genes to transfect endothelial-like cells, initiating a dramatic increase in eNOS expression and resulting in NO production.[55] In addition, Levy et al. constructed a gene delivery platform, where they loaded iNOS-cDNA on an adeno-associated virus serotype 2 vector to deliver iNOS and produce a large amount of NO *in vitro*.[56]

However, the high technical requirements and cost of these NOS gene strategies necessitate more efficient NO production pathways.

Another approach involves RSNOs, which are endogenous NO donors in blood and represent a continuous source of NO. Both selenium (Se) and copper (Cu) ions have glutathione peroxidase (GPx)-like catalytic activity that can decompose RSNOs into NO *in vivo*, so a series of strategies for catalytic NO generation were developed.[57] For example, our team incorporated selenocystamine into DA by co-immobilization, controlled the NO rate by regulating the amount of Se, and could release NO continuously for more than 60 days.[58] To further improve NO production, we replaced Se with Cu for its higher catalytic activity, and showed that the NO flux rate reached the natural release rate in ECs.[59]

1.3.3 Combination of NO release and generation strategy

In biomedical applications, maintaining NO release in the upper end of the physiological region (~ 4×10^{-10} mol/cm^2/min) can enhance the therapeutic effects of NO, while a short-term high NO throughput benefits anti-bacteria. However, traditional NO donors cannot maintain a continuous NO flux, while the GPx-like catalytic moieties lack the ability for burst NO release. Therefore, researchers have combined NO release and generation strategies to complement NO supply. In a study, Handa et al. incorporated SNAP into Cu nanoparticles to ensure NO supply from both exogenous donor SNAP decomposition and endogenous RSNOs catalyzed by Cu; the NO flux could reach 4.48 ~ 4.84 $\times 10^{-10}$ mol/cm^2/min.[60] In another research, Brisbois et al. designed a multilayer polymer blending Se and SNAP, where SNAP provided a high initial NO supply to inhibit bacterial growth, while Se maintained continuous NO generation to prevent thrombus.[61]

Additionally, Chandrawati et al. found that zinc oxide (ZnO) possesses natural GPx and Gal activities to break down RSNO and β-Gal-NONOate into NO. ZnO could maintain the catalytic performance for 6 months, and by changing the amount ZnO and NO prodrug, the group achieved on-demand NO supplement.[62]

Overall, these combination strategies are very encouraging in terms of NO production, and ongoing efforts include improved manufacturing processes and relevant medical materials for future clinical applications.

1.4 Current NO production platforms

The NO production strategies described above can control NO release/generation but suffer from disadvantages such as limited loading and lack of targeting. To circumvent such shortcomings, researchers have sought to combine NO production strategies with biomedical materials, based on the needs of different diseases (Fig. 1-3).

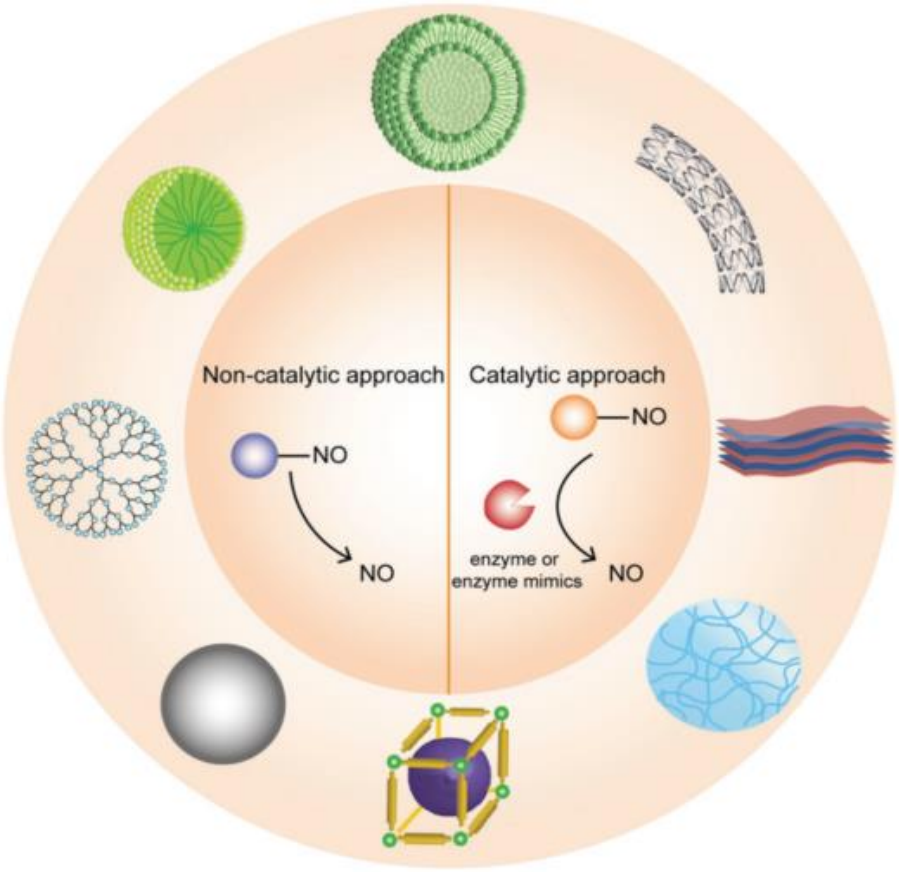

Fig. 1-3. An overview of different NO platforms that contain NO donors and catalytic conversion. Figures are reproduced from Ref. [45] with permission. Copyright 2018, Wiley.

1.4.1 NO production cardiovascular stent

Millions of people with cardiovascular disease have been spared thanks to stenting by

unclogging the blocked blood vessels and restoring blood flow. However, the therapeutic effect of stents is severely limited due to stent intimal hyperplasia or stent thrombosis as the implantation can cause endothelial damage. Motivated by the multiple biological activities of NO, many NO production stents have been proposed.

For instance, Elnaggar et al. proposed a liposome-based layer-by-layer deposition to achieve controlled release of NO donors on cardiovascular stent. The NO donor NONOate was first encapsuled in liposomes, and then the NO-liposomes were sandwiched between a polylysine layer and a hyaluronic acid-dopamine conjugate layer. Such layer-by-layer deposition improved the loading of NO donors (Fig. 1-4Ai). The coating showed smooth surface (Fig. 1-4Aii) and the stent could release NO continuously for 5 days with a good antithrombotic effect.[63]

In one study of Chen et al., a hydrogel-coated stent that eluted NO was developed (Fig. 1-4Bi). The hydrogel coating mainly consisted of alginate and gelatin, which could mimic extracellular matrix (ECM) to allow ECM remodeling on the stent surface. In addition, alginate was coupled with Se to continuously catalyze the generation of NO for at least 1 month (Fig. 1-4Bii). Meanwhile, this combination of hydrogel and NO could promoted EC adhesion and growth, prevented thrombus formation, inhibited smooth muscle overgrowth, and facilitated rapid endothelial recovery (Fig. 1-4Biii).[64]

In a study, Zhang et al. fabricated a vascular double-layer stent based on NO-releasing peptides. This design consisted of two types of peptide nanofibers, which could be deposited in layers on the stent surface (Fig. 1-4Ci). The first peptide contained laminin to allow cell attachment, while the second peptide contained a polylysine sequence to generate NO. The nanomatrix coating improved reendothelialization, modulated SMC phenotype, suppressed inflammation, and inhibited restenosis (Fig. 1-4Cii and iii).[65]

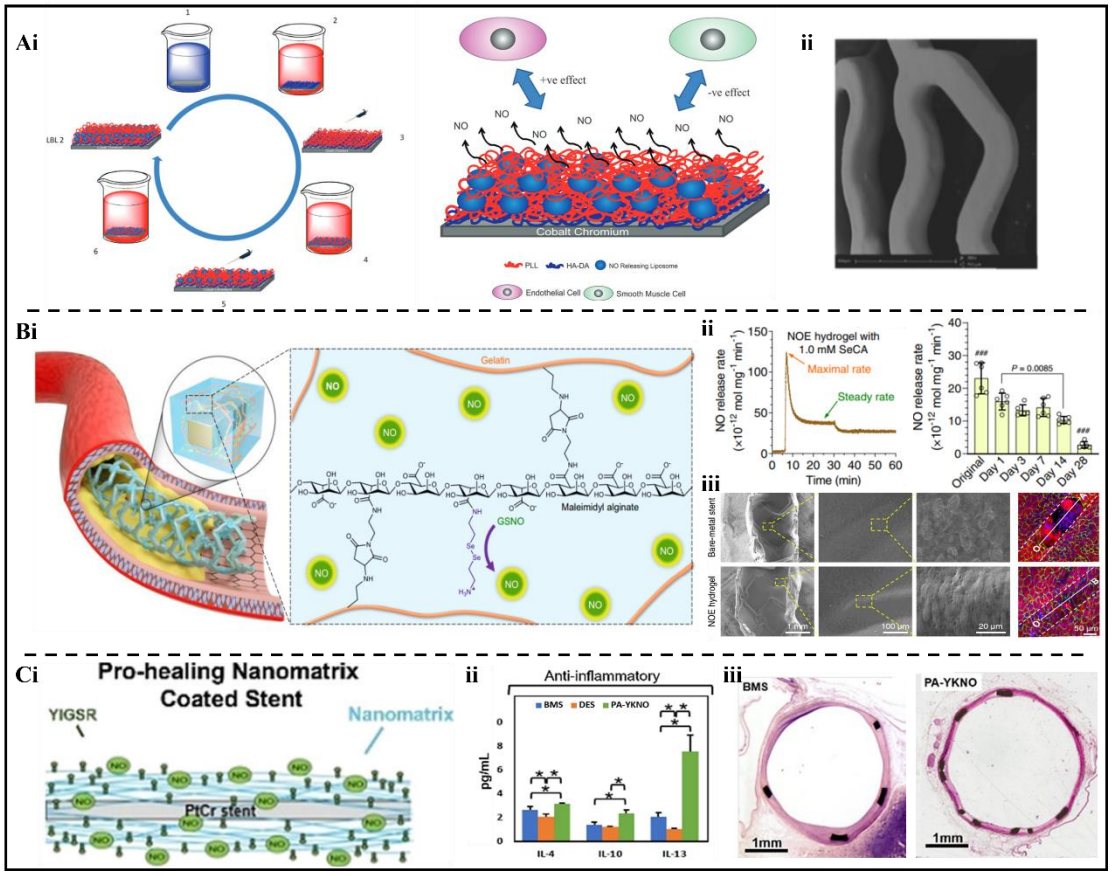

Fig. 1-4. NO production cardiovascular stents. (A) Layer-by-layer NO-liposome coating by Elnaggar et al.: (i) Preparation of NO-liposome coating and the multilayer structure. (ii) Scanning electron microscopy (SEM) observation of NO-liposome coated stent. Figures are reproduced from Ref. [63] with permission. Copyright 2016, John Wiley and Sons. (B) NO-eluting hydrogel-coated stent by Chen et al.: (i) Schematic for the coating design. (ii) Real-time (left) and long-term (right) NO release profiles. (iii) SEM (left) and cluster of differentiation 31 (CD31) immunofluorescent (right) images of stent surface after 3 months *in vivo* implantation. Figures are reproduced from Ref. [64] with permission. Copyright 2021, Springer Nature. (C) NO-releasing PA stent by Zhang et al.: (i) Structure of NO-releasing PA stent. (ii) Anti-inflammatory observation by enzyme-linked immunosorbent assay (ELISA) and (iii) anti-restenosis evaluation by van Gieson staining. Figures are reproduced from Ref. [65] with permission. Copyright 2022, American Chemical Society.

1.4.2 NO production bone scaffolds

Treating bone diseases – such as bone defects, fractures and osteoma resection – often relies on existing autogenous or allogenic tissue grafts, but the drawbacks include limited sources, poor bone repair and neovascularization. Based on the dual role of NO in osteogenesis and angiogenesis, scientists have developed a series of synthetic bone scaffolds for targeted and local delivery of therapeutic NO for better bone regeneration, blood vessel formation, wound healing and antimicrobial effects.

For example, our group designed an osteogenic and angiogenic platform to mimic periosteum, which is a physical barrier that stably connects bone tissues and mediates bone homeostasis. The system involved gelatin methacrylate (GelMA), hydroxyapatite methacrylate nanoparticles, and NO precursor Arginine, prepared by electrostatic spinning (Fig. 1-5Ai). GelMA and nanoparticles provided biocompatibility, mechanical properties, and calcium ion (Ca^{2+}) storage, while Arginine enabled long-term NO release (Fig. 1-5Aii). After implantation, the scaffold released Ca^{2+} and Arginine, activated the NO-cGMP pathway, and mimicked the functions of natural periosteum to promote bone healing (Fig. 1-5Aiii).[66]

In another study, Lee et al. proposed a bioactive scaffold to account for the complex interactions (like inflammation, infection, bone fracture) during osteoporotic bone regeneration. They used polylactic-glycolic acid scaffolds with incorporated nanoparticles containing the NO catalyst ZnO, the osteoporosis drug alendronate, and the bioactive agent bone morphogenetic protein-2 (BMP-2). The NO produced by ZnO stimulated the activities of cGMP and protein kinase G to promote angiogenesis; alendronate inhibited osteoporosis while BMP-2 promoted bone repairing (Fig. 1-5Bi). This scaffold combined NO with drugs and active factors to regulate bone homeostasis, exhibiting anti-inflammatory, angiogenic, anti-osteoclastogenic, and bone regenerative effects (Fig. 1-5Bii and iii).[67]

Separately, Yang et al. designed a 3D-printed scaffold that integrated near infrared (NIR)-induced photothermal therapy and gas therapy to suppress tumor growth and promote bone repair. Specifically, the bioactive glass scaffold contained a photothermal material MXene grafted with NO donor SNO-loaded mesoporous silica. MXene had a

good photothermal conversion efficiency, and the generated heat could promote NO release in a controlled manner (Fig. 1-5Ci). The high heat along with high concentration of NO in the early stage endowed anti-tumor properties, while the small amount release of NO in the late stage could promote bone regeneration (Fig. 1-5Cii). Meanwhile, the enhanced blood supply by NO enhanced the transport of phosphorus and Ca, which was beneficial to bone regeneration. This tunable NO production scaffold could orderly assist tumor inhibition, and then couple angiogenesis with bone regeneration (Fig. 1-5Ciii and iv).[68]

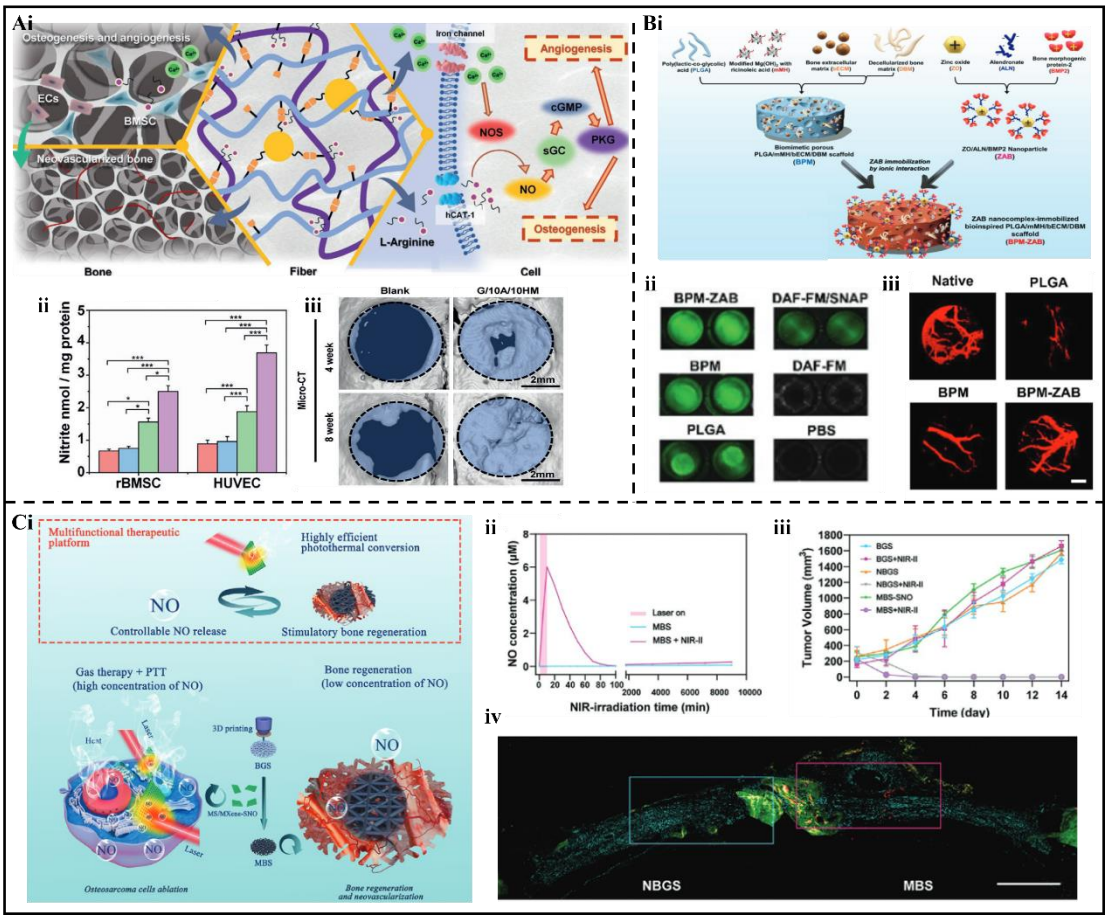

Fig. 1-5. NO production bone scaffold. (A) NO production periosteum by Yang et al.: (i) Osteogenic-angiogenic coupling effect by NO periosteum. (ii) Quantification of NO production in cellular level. (iii) 3D reconstruction of defect areas by micro-computed tomography (micro-CT). Figures are reproduced from Ref. [66] with permission. Copyright 2021, John Wiley and Sons. (B) NO catalyst ZnO loaded biomimetic scaffold by Lee et al.: (i) Schematic for the scaffold design. (ii) Fluorescent signal for cellular NO tracing. (iii) 3D reconstruction images of new formed blood vessels after

implantation. Figures are reproduced from Ref. [67] with permission. Copyright 2022, John Wiley and Sons. (C) Photothermal NO production scaffold by Yang et al.: (i) Illustration of controllable NO release and corresponding therapeutic effects. (ii) NO release under NIR irradiation. (iii) Tumor inhibition effect. (iv) CD31 immunofluorescent images after *in vivo* implantation. Figures are reproduced from Ref. [68] with permission. Copyright 2020, John Wiley and Sons.

1.4.3 NO production nano/micro-carriers

Nano/micro-carriers are an important medium for transporting NO. Because of their small size, they can reach various organs or tissues either sparsely or densely. By using different materials or surface modifications, these carriers can accurately transport NO to the lesion.

Due to its fast onset and limited therapeutic window, acute ischemic stroke presents a significant obstacle for early identification and treatment. Inspired by the role of natural platelets in actively targeting and adhering to injured vessels during blood clot formation, Li et al. designed a biomimetic carrier, which used platelet membrane to encapsule Arginine and magnetic nanoparticles for targeted delivery (Fig. 1-6Ai). After *in vivo* administration, a magnetic field was applied at lesion site which could lead magnetic nanoparticles rapid move to the lesion site, and then combined with the natural targeted adhesion of platelets, this bionic carrier would accurately locate the thrombus and deliver Arginine in a dual-targeted manner (Fig. 1-5Aii). After aggregation and release of Arginine at lesion (Fig. 1-5Aiii), ECs internalized Arginine to produce NO, which promoted vasodilation, disrupted local blood clots, and repaired the microvascular network around the lesion (Fig. 1-5Aiv). Thus, this carrier was a promising diagnostic and therapeutic candidate for stroke.[69]

Additionally, motivated by the function of NOS, Li et al. proposed a nano-carrier made of catalytic noble metal core and mesoporous silica shell. Similar to NOS, noble metal (e.g., gold) has oxidizing property and can react with glucose, NADH and catalase, etc. When contacted with oxygen molecules, noble metal is activated to

oxidize reduced substrates like oxidized Arginine to generate NO (Fig. 1-5Bi). Meanwhile, the mesoporous silica shell could protect the gold nanorods from protein adsorption while allowing smaller molecules such as NADPH and oxygen to enter the core for reaction. These nanoparticles could be taken up by ECs and sustain intracellular NO production (Fig. 1-5Bii and iii). Such nanoparticles that mimic natural NOS had a wide range of applications.[70]

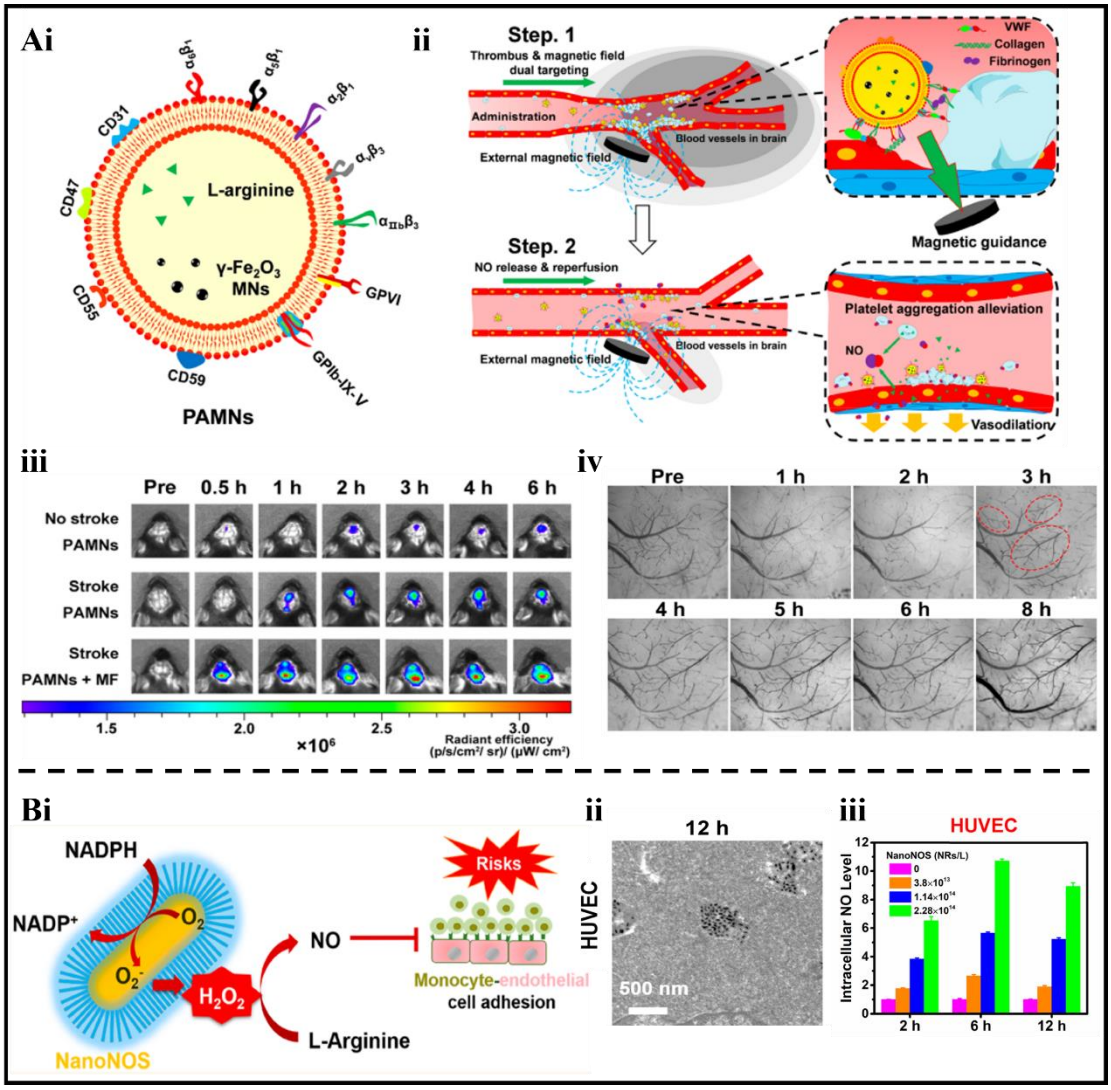

Fig. 1-6. NO production nano/micro-carriers. (A) Platelet-mimicking NO carrier by Li et al.: (i) Structure of NO carrier. (ii) Illustration of targeting mechanism. (iii) *In vivo* NO carrier targeting effect evaluation. (iv) Vascular network rebuilt by NO around the lesion. Figures are reproduced from Ref. [69] with permission. Copyright 2020, American Chemical Society. (B) NOS-mimicking noble metal nanoparticles by Li et al.: (i) Schematic of nanoparticles to oxidize Arginine to generate NO. (ii) Cell uptake

of metal nanoparticles by transmission electron microscope. (iii) NO production in cells. Figures are reproduced from Ref. [70] with permission. Copyright 2020, American Chemical Society.

1.5 Motivation and objective

This dissertation delves into the multifaceted physiological roles of NO in cardiovascular homeostasis and bone repair by recreating relevant microenvironment that supports NO production.

Firstly, considering the suboptimal endogenous NO donor supply in cardiovascular disease, we proposed a stent coating that could produce NO under any conditions (with or without NO donors).

Subsequently, based on the chronological responses following vascular damage and the spontaneous cellular production of NO after EC aggregation, we designed a cell-recruiting and NO-producing stent coating to promote reendothelialization, anti-thrombosis and anti-restenosis.

Lastly, we constructed a NO donor-free bone scaffold that recruited BMSCs and vascular cells, which contributed to the spontaneous, natural NO production from cells and remodeled bone microenvironment.

Specific objectives of project 1:

(1). To develop a NO-fueled stent coating that can produce NO regardless of NO donor presence.

(2). To investigate the effects of the coating on cell behaviors.

(3). To study the inhibitory effect of NO fuel coating on thrombosis and restenosis *in vivo*.

Specific objectives of project 2:

(1). To fabricate a cell-adherent coating where NO is produced by adherent cells and NO generation elements.

(2). To prove the temporal therapeutic effects in terms of cell behaviors.

(3). To validate the reendothelialization, anti-thrombosis and anti-restenosis of the coating *in vivo*.

Specific objectives of project 3:

(1). To prepare a bone scaffold that can capture osteogenic and angiogenic cells to produce NO spontaneously without external NO addition.

(2). To study the *in vitro* osteogenesis and angiogenesis of the scaffold.

(3). To investigate *in vivo* bone regeneration effect of the scaffold.

Chapter 2 Development of self-sustainable NO fuel coating for anti-thrombosis and anti-restenosis

2.1 Introduction

Cardiovascular disease (CVD) is a significant contributor to disability and mortality worldwide.[71, 72] The main etiology of CVD is the buildup of fat molecules and cell debris at the lesion site (i.e., plaque deposition), where the plaque growth and calcification narrow the vessel, and vasoconstriction reduce blood flow.[73] To address CVD cases involving arterial blockages, surgical intervention using cardiovascular stents (CVSs) is commonly employed.[74] However, the implantation of stents inherently damages the endothelial structure, reducing the activity of eNOS, which impairs subsequent NO production and disrupts the vascular homeostasis, eventually causing thrombus to block blood vessels.[75, 76] Under normal physiological conditions, endothelial glycocalyx (like heparin) and NO maintain an anticoagulant environment, where heparin prevents platelet adhesion and increases eNOS activity,[77-80] while NO allows EC migration & proliferation and activates NO-cGMP, inhibiting the migration of SMC and the adhesion of platelet (Fig. 2-1).[81, 82] In light of these insights, a biomimetic endothelial vascular stent with NO-producing properties is crucial to prevent thrombosis and restenosis after stent placement.

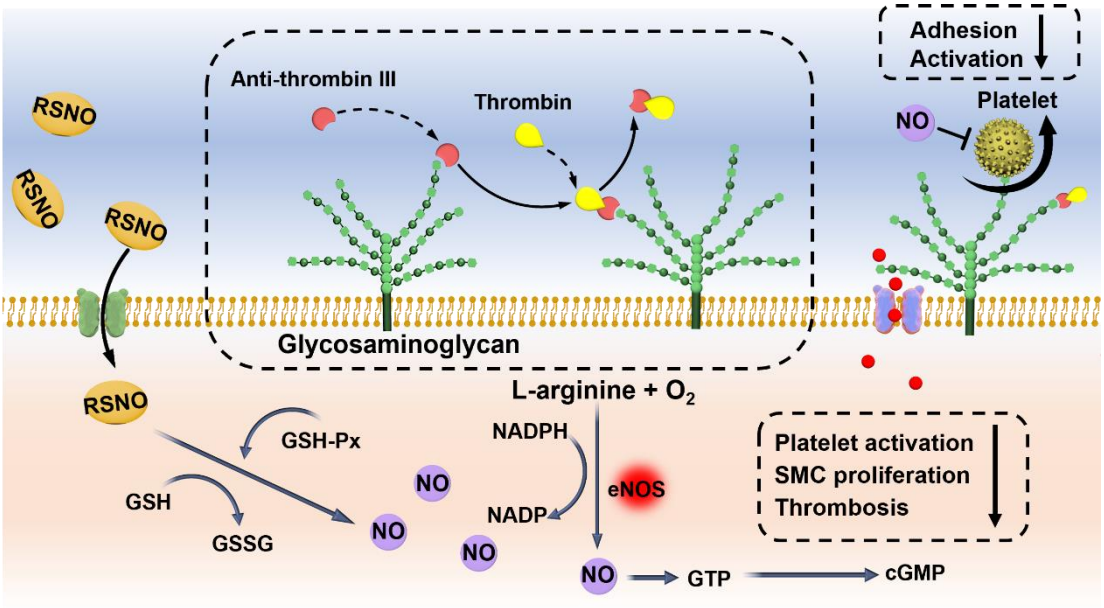

Fig. 2-1. Natural endothelium is rich in glycocalyx heparin and arginine transporter,

where heparin has anticoagulant properties and can increase the eNOS activity to generate NO from its principal precursor (arginine). The essential event of thrombosis, platelet adhesion, and SMC migration can both be inhibited by the generated NO (a major factor contributing to restenosis).

Recently, many NO-production CVS coatings were created.[62, 83] For example, a coating consisted with dopamine (DA) and copper (Cu) exhibited strong NO generating ability.[58, 59] Due to the catechol structure of DA and NO catalytic effect of Cu, DC can tightly adhere to the surface of the stents and sustainably catalyze endogenous RSNO conversion into NO.[59, 84] Nevertheless, in the real pathophysiological microenvironment, this coating design overestimates the local concentration of endogenous NO donors. Specifically, oxidative stress in CVD increases the secretion of thioredoxin and accelerates RSNO's denitrosation. As a result, insufficient NO production *in vivo* compromises the therapeutic efficacy of the stent coating.[85, 86]

To compensate for the decreased RSNO levels in the real physiological milieu, NO precursors can be added to the CVS coating. One strategy inspired by healthy endothelium is to incorporate arginine (converted into NO via eNOS even when no RSNOs presence) and heparin (increases eNOS activity). Such design prevents systemic administration of RSNOs after stent implantation and reduces the risks of hypotension and vasodilation.[66, 87]

Here, we designed a self-sustainable NO-fueled stent coating, which consisted of DC networks with grafted arginine and heparin, namely DCHA coating. Due to the reduction of Cu(II) to Cu(I), our coating could convert RSNOs to NO by GSH while forming byproduct glutathione disulfide (GSSG) (Fig. 2-2A and B).[58] Then, with oxygen and NADPH, arginine were converted to citrulline and NO by eNOS (could be increase by heparin). The increased NO facilitated EC growth even without NO donors, and its byproducts (citrulline) underwent recycling into arginine (Fig. 2-2A and C). [88, 89] Moreover, the soluble guanylyl cyclase (sGC) and cGMP can be stimulated by the

generated NO,[90] thereby suppressing SMC and platelet and promoting vasodilation.[91] It is expected that the self-sustainable NO stent will decrease restenosis and blood clot formation (Fig. 2-3). This design allowed the components in the DCHA coating to act synergistically in endothelial remodeling while compensating for any potential decrease in RSNOs in the physiological milieu. In addition, we anticipate that the DCHA coating would inhibit platelet adhesion, prevent SMC growth, and overcome stent thrombosis and restenosis.

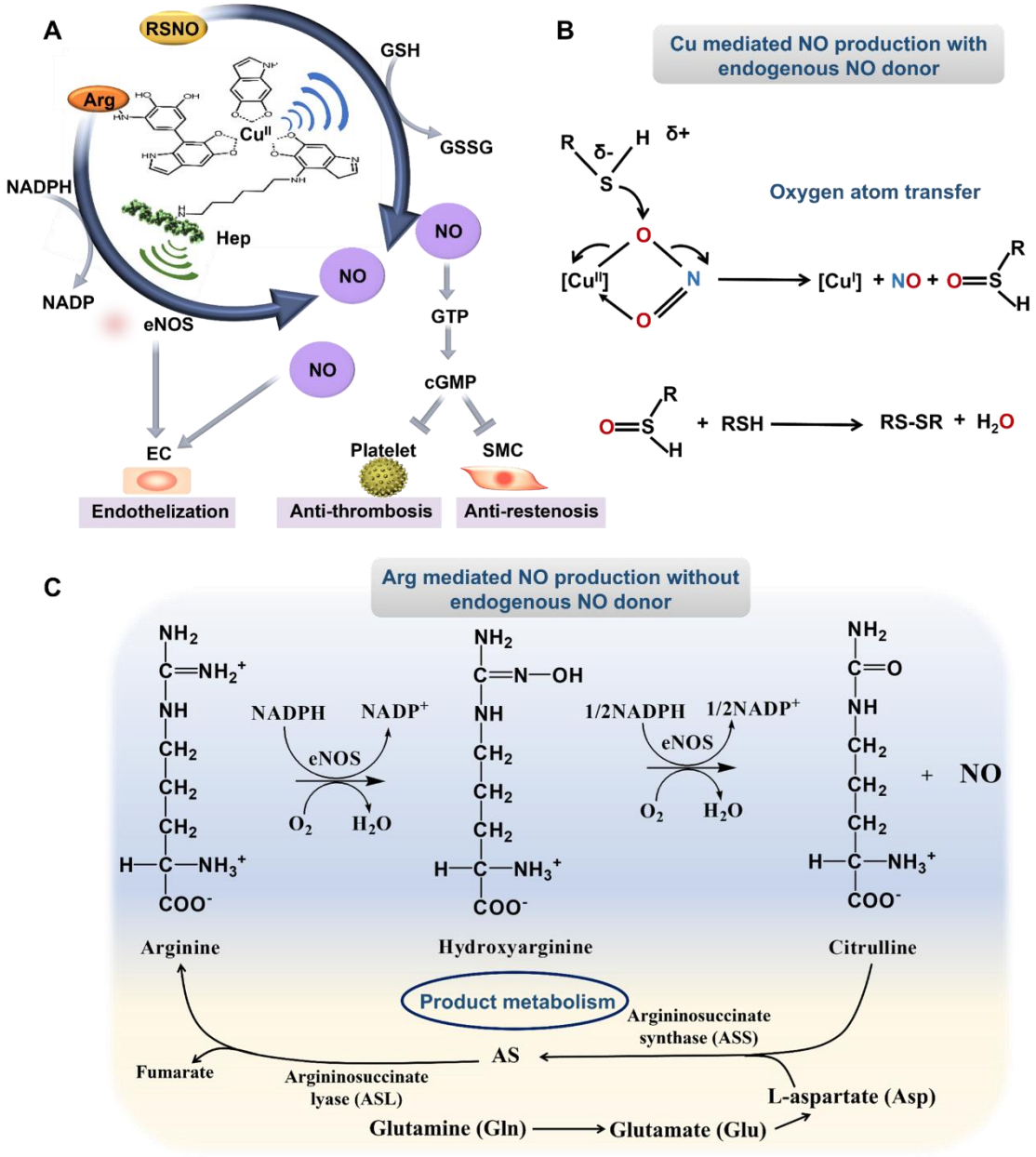

Fig. 2-2. (A) Illustration of DCHA producing NO and its effect on the modulation of cell behaviors. (B) Cu mediated NO production from NO donor. (C) Arginine mediated NO production and arginine-citrulline metabolism cycle.

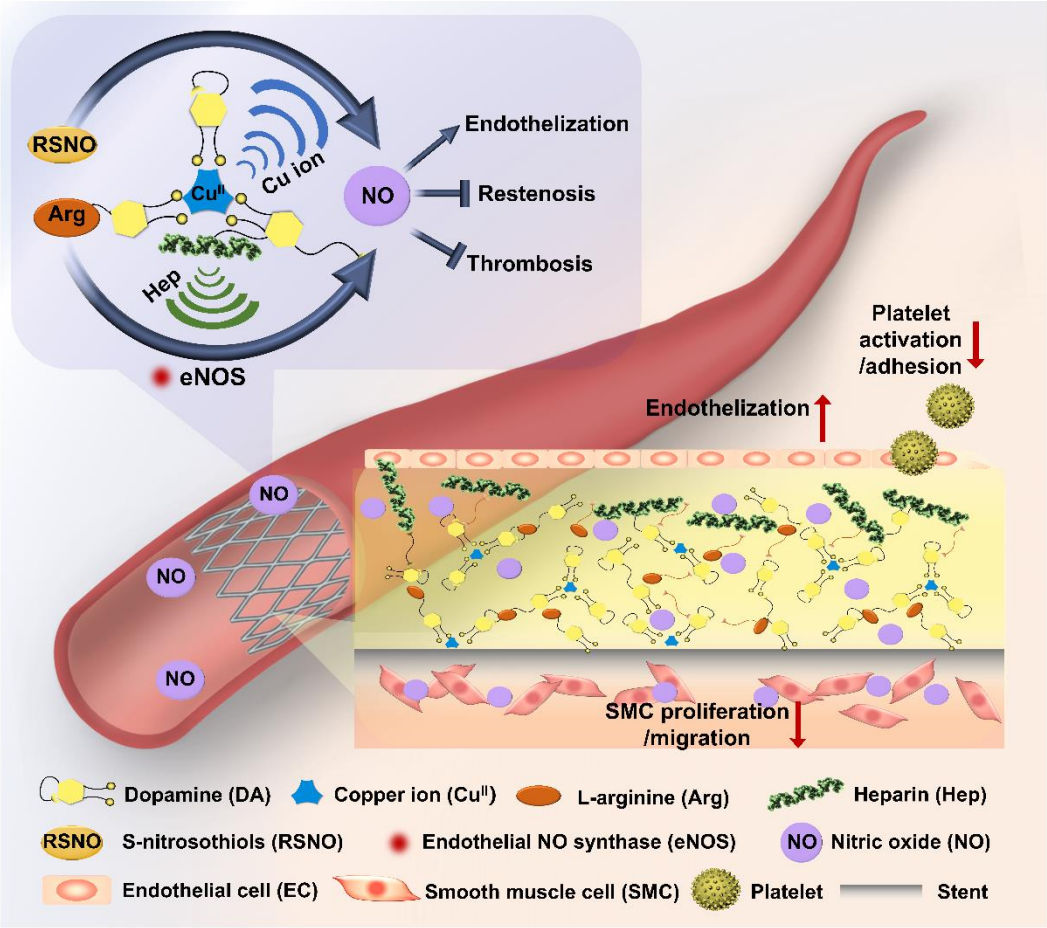

Fig. 2-3. Schematic structure and function of a DCAH coating capable of self-sustaining NO production. This coating has an endothelium-like structure. The DA base allows arginine and heparin grafting, and continuously catabolizes RSNOs conversion into NO; while eNOS, whose activity may be increased by heparin, converts arginine to NO even without RSNO's presence, thus compensating for the reduction of donor levels in the actual physiological environment. This coating has a continuous and self-sustaining NO supply to promote EC growth, suppress platelet adhesion, prevent SMC growth, and ultimately address stent thrombosis and restenosis.

2.2 Materials and Methods

2.2.1 Fabrication and characterization of DCAH coating

2.2.1.1 Fabrication of DCAH coatings

Dopamine (1 mg) and $CuCl_2$ (5 μg) were dissolved in 1 mL tris-(hydroxymethyl)-aminomethane hydrochloride (Tris-HCl; pH 8.5) to prepare a DC solution.[59] 316L stainless steel (316L SS, one of the most common materials used for CVS) bases were

dipped in DC solution for 24 h at room temperature to prepare DC coatings. Then, the DC samples were dipped in 1 mL arginine (1 mg) solution for 24 h to prepare the DCA coatings.[83] Subsequently, 1 mg heparin was pre-activated by N-hydroxysuccinimide (NHS) andN-(3-dimethylaminopropyl)-N-ethylcarbodiimide (EDC) in a 2-(N-morpholino) ethanesulfonic acid hydrate (MES, 1 mL, pH 5.5) solution, and then placed the DCA samples into the above solution to obtain DCAH coatings (Fig. 2-4).[62]

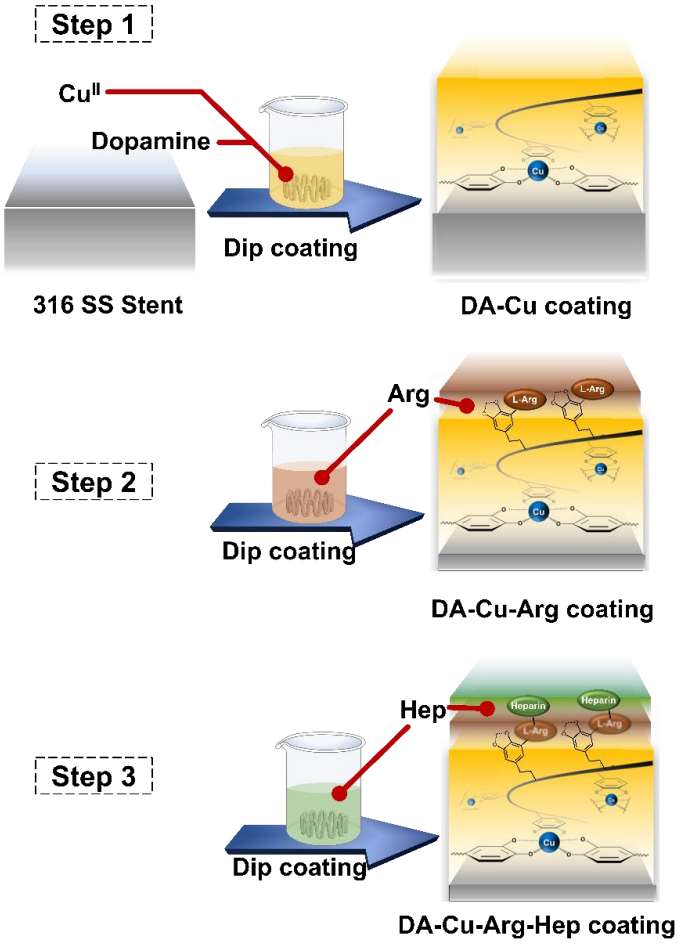

Fig. 2-4. Fabrication of DCAH coating by three-dipping method. The first step was to immerse the 316L SS substrates into DC solution, followed by dipping into arginine solution. After placing it in heparin solution, the DCAH coating was prepared.

2.2.1.2 Characterization of DCAH coatings

Matrix-assisted laser desorption/ionization-time of flight mass spectroscopy (MALDI-TOF-MS), with high sensitivity measuring m/z < 1000, was used to examine the chemical structure of the DC complex. X-ray photoelectron spectroscopy (XPS) was used to determine the elemental distribution. Fourier transform infrared spectroscopy

with attenuated total reflection (ATR-FTIR) allowed for the detection of the chemical structure of DCAH coating. Using a SEM, the surface morphology was investigated. Using a quartz crystal microbalance equipped with dissipation (QCM-D) equipment, the mass of arginine and heparin immobilized onto the DC was ascertained. Briefly, the coated samples were placed inside the testing chamber, and the QCM-D system was then injected with arginine solution. After arginine grafting was saturated, phosphate-buffered saline (PBS) was administered to remove poorly bound arginine. The grafting amount was represented by the residual arginine amount, which was determined by using the Sauerbrey equation to the adsorbed mass. In a similar manner, the QCM-D system was filled with the heparin solution until it was saturate, then washed with PBS, and the final adsorption mass was recorded. A contact angle meter was used to measure the water contact angle (WCA) and surface hydrophilicity. Through balloon dilation testing, the coatings' mechanical stability was examined. the DCAH-coated CVS was linked to the angioplasty balloon, and its surface shape was observed using SEM.[58] Lastly, dilated DCAH stents were placed inside a tube and flushed with a 200 mL/min PBS. After 1 month, the surface morphology was examined using a SEM to determine the stability of the DCAH coating under PBS flow.

2.2.2 Assessment of sustained NO generation

An eNOS inhibition test was performed to confirm the effects of arginine on NO production and heparin on eNOS increase. Briefly, at 5×10^4 cells/cm^2 human umbilical vein endothelial cells (HUVECs) were seeded on each sample in a medium containing or lacking the eNOS inhibitor NG-Monomethyl-L-arginine (L-NMMA, 0.5 mM). Following 3 days of co-cultivation, the NO was teat using a total NO kit, the eNOS expression was determined by ELISA, and the NO signal was detected using a DAF-FM DA probe. To investigate long-term NO production, bare, DC, and DCAH-coated foils were immersed in of PBS with NO donors (10 μM GSH and SNAP, replaced every 6 h), and at day 1, day 5, day 10, day 15 and day 30, NO production was quantified.[92-94] To investigate the cellular NO production by arginine, samples that immersed in PBS were taken out at day 0, 7, 14 and 28. Then, 5×10^4 cells of HUVECs were seeded on each sample without NO donors. The cellular production of NO was observed using the DAF-FM DA probe, and a fluorescence microscope was used to view the NO fluorescent signal.

2.2.3 *In vitro* biological properties of DCAH coating

2.2.3.1 Evaluation of the growth of HUVECs and HUASMCs on the developed coatings

HUVECs or HUASMCs were cultivated in the media with or without NO donors provided every 6 h) and 5×10^4 cells were seeded onto each surface (bare, D, DC, DDCA, DCH, and DCAH). The cytotoxicity of the coatings was investigated using live/dead staining. After co-culturing with NO donors for 3 days, cells were observed by calcein acetoxymethyl ester (AM) and pyridine iodide (PI) staining. For the visualization cell proliferation, cell-seeded samples were stained by fluorescein isothiocyanate (FITC)-phalloidin to visualize the proliferation of the cells. Cell growth on different coatings was assessed using the Cell Counting Kit-8 (CCK-8).

The foils were folded in half, with one side remaining uncoated and the other half had coating to observe cell migration. Cells were seeded on the uncoated side and incubated for 4 hours before to migration assays. After that, the side that without cells was flipped and added medium containing NO donor (refreshed every 6 h). After 1 day, the samples were stained with phalloidin.[83]

2.2.3.2 Investigation of the HUVECs and HUASMCs' competitive adherence to the proposed coatings

The cells were pre-stained with green (EC) and red (SMC) fluorescence to investigate the competitive adhesion. Pre-labeled cell suspensions in equal volumes were mixed and subsequently seeded at 5×10^4 cells on each surface. Following 24 and 72 h (with NO donors), the count the adherent cells were examined by Image J software.[95]

2.2.3.3 Platelet adhesion assay

Following protocols authorized by the Ethics Committee of the Hong Kong Polytechnic University, fresh blood was collected from rats. The platelet related experiments received helps from Miss Yongyi MO. In accordance with the manufacturer's instructions, an anti-Factor Xa (FXa) test was conducted to confirm the bioactivity of heparin. Centrifugation was used to extract platelet-poor plasma (PPP) from whole blood (3000 rpm, 15 min). At 37°C, each sample were treated with PPP for 30 min. Following that, test solutions were introduced to each sample, and 405 nm was used to

measure the absorbance. The levels of fibrinogen and fibrinogen gamma chain (FN and Fg-γ) were measured to assess FN adsorption and activation, respectively. Briefly, each sample were treated with PPP for 2 h. For FN and Fg-γ test, test kits were used following manufacturer's instructions. Whole blood was centrifuged at 1500 rpm for 15 min to extract platelet-rich plasma (PRP), and the PRP were then diluted and seeded at a density of 3×10^4 cells/well onto each sample, then incubated them at 37°C for 2 h. Calcein-AM staining and SEM were used to observe platelets. Additionally, PRP was incubated for 2 h and then Triton-X was added, and a cGMP ELISA kit was utilized to examine the supernatant.[62, 96]

2.2.4 Assessment of the stent coatings' *ex vivo* anti-thrombogenic activity

Following protocols authorized by the Southern Medical University Ethics Committee. The animal experiments were assisted by Mr. Xiaohui MOU from Prof. Zhilu YANG's research group. Briefly, the proposed coatings' anti-thrombogenicity was evaluated using an arteriovenous (AV) shunt model in rabbits (3.5-4.0 kg) (Fig. 2-5). The bare, D, DC, DCA, DCH, and DCAH foils were fixed inside PVC tubes prior to the animal trials. Following anesthesia, the rabbits' arteries and veins were connected to the PVC blood transfusion apparatus. The circuits were turned off after 2 h, and the sample were collected for SEM examination. The occlusion rate was calculated using images of cross-sections of tubes. In addition, blood clots were gathered, recorded, and weighed.[88, 97]

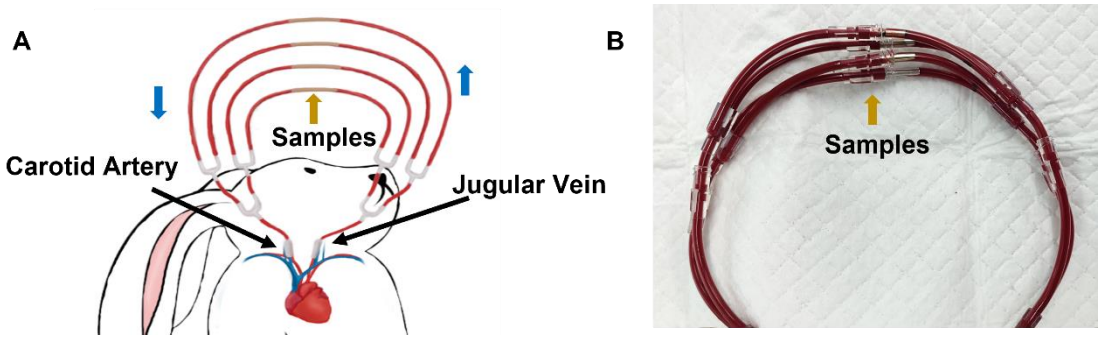

Fig. 2-5. (A) The illustration of the *ex vivo* AV-shunt circulation model. (B) Sample installed PVC tubes of the *ex vivo* circulation.

2.2.5 Assessment of *in vivo* efficacy of DCAH coatings

For the *in vivo* investigations, the rabbits' arteries were exposed after anesthesia, and the iliofemoral arteries were implanted with commercial PrimtechTM (bare 316L SS)

and DCAH coated stents at opposing locations. At 1 week, the arteries were collected to observe the adherent platelets by SEM. At 1 and 3 months, Van Gieson's staining was applied to each implanted sample to assess the structure of the stented artery.[98, 99]

2.2.6 Statistical analysis

Every experiment, unless specified differently, was carried out in triplicate. The data was shown as mean ± standard deviation. GraphPad Prism was utilized to perform statistical analysis using the T-test and one-way ANOVA. The statistically significant values, indicated by the symbols *, **, and ***, respectively, referring as $p < 0.05$, 0.01, and 0.001.

2.3 Results and discussions

2.3.1 Fabrication and Characterization of DCAH coating

2.3.1.1 Fabrication and optimization of DCAH coating

By using a dipping method, the DCAH coating was fabricated without the use of any organic reagents.[59, 62] The grafting amount of arginine and heparin was measured using QCM-D. As shown in Fig. 2-6, approximately 513 and 430 ng/cm^2 of arginine and heparin immobilized.

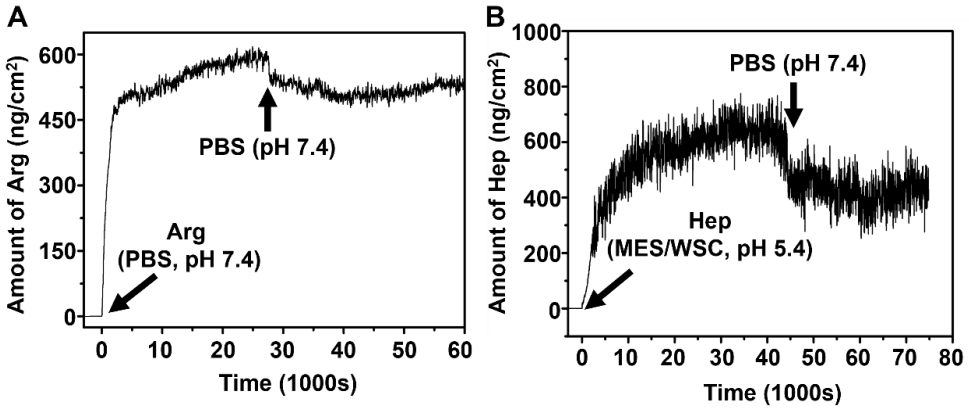

Fig. 2-6. Immobilization amount of arginine (A) and heparin (B) using QCM-D. The stabilized curves represented the grafting amount.

The zeta potential of each stent coating was measured to ascertain the grafting sequence of arginine and heparin. Fig. 2-7 showed arginine's cationic property could raise the potential, and the addition of heparin concealed the positive charge due to its

anionic property, suggesting that the DCAH had the potential to increase endothelial homeostasis.

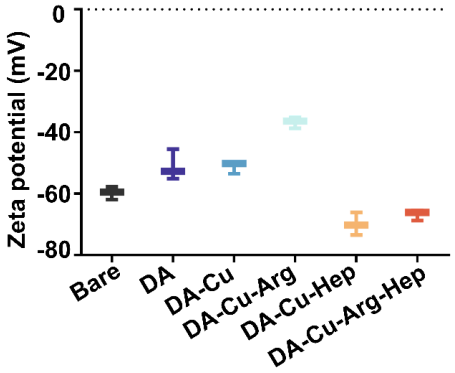

Fig. 2-7. Zeta potential of each sample. The introduction of arginine increased zeta potential, while the heparin could shield the positive charge.

2.3.1.2 Characterization of DCAH coating

We carried out a series of studies to describe the chemical characteristics of the stent covering. First, MALDI-TOF-MS was performed to study the possibility of Cu and DA polymerizing (Fig. 2-8A). The peaks at m/z 212, 335, and 610 proved the immobilization of DC. After that, the elementary composition was analyzed using XPS. DC and DCAH showed Cu peaks, indicating the coordination of Cu (Fig. 2-8B). DCAH coating also showed a clear S peak (belonging to Heparin). As shown in GATR-FTIR result (Fig. 2-8C), the DC and DCAH coatings had peaks belonging to dopamine, while the DCAH coating featured with the -C=N and -S=O peaks belonging to arginine and heparin, respectively. According to these findings, the DCAH complexes were successfully incorporated into 316L SS substrate.

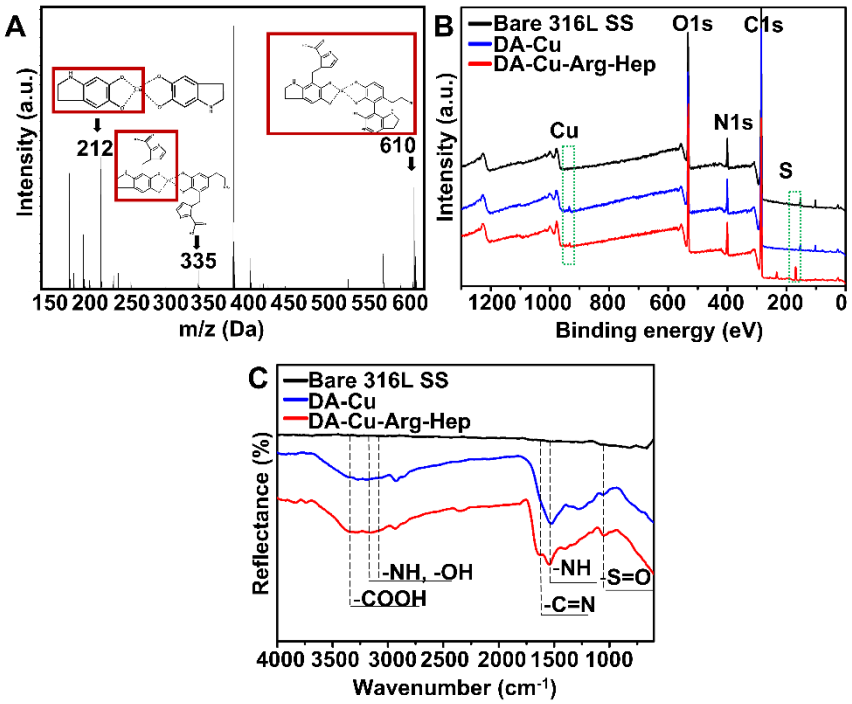

Fig. 2-8. (A) MS spectra of polymerization between dopamine and copper. (B) XPS result, where Cu and S (belonged to heparin) could be found in DCAH group. (C) FTIR spectra of bare, DC, and DCAH coatings. Characteristic peaks of arginine (-C=N) and heparin (-S=O) could be found in DCAH coating.

Next, the DCAH coating's physical characteristics were examined. The SEM examination showed that the coating distribution was homogeneous across each coated sample (Fig. 2-9A). The energy-dispersed X-ray (EDX) results showed that the DCAH coating had N, O, C, Cu, S peaks. In the protuberant area, the elemental signals were more concentrated and less dispersed than in the flat area. (Fig. 2-9B).

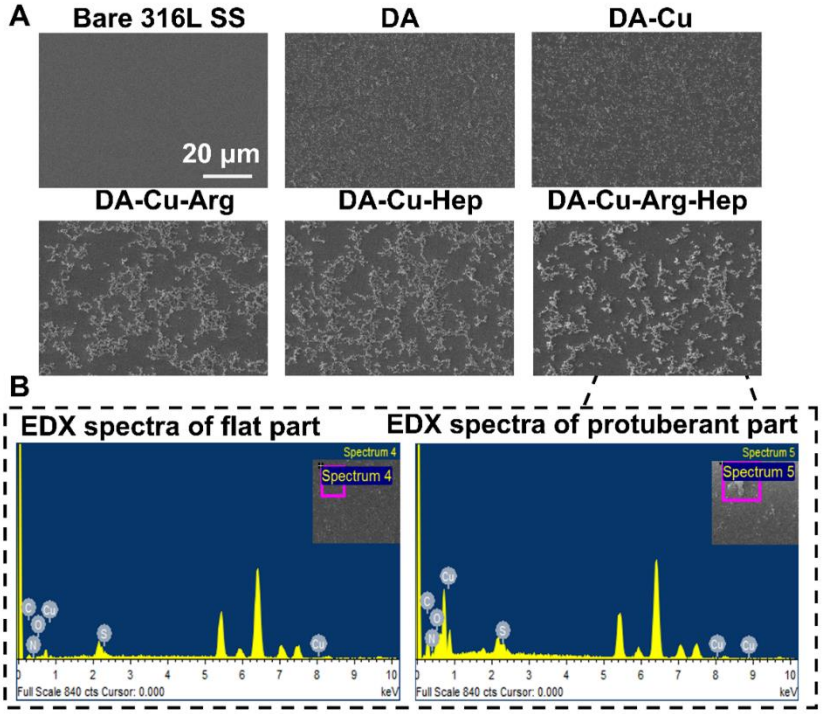

Fig. 2-9. (A) Representative SEM micrographs of each coating demonstrated uniform coating distribution. (B) EDX spectra of the DCAH coating.

The thickness data (Fig. 2-10A) showed the coating thickness was nanometer-thin. Such thinness had little effect on the stent surface structure and was more stable than micrometer thickness.[83] Next, the WCA was calculated. Fig. 2-10B showed that the bare surface had a very high WCA (~85.8°), which was decreased in all coated samples (< 60°), showing that hydrophilicity was enhanced by the immobilization of DA, Cu and arginine. The remarkable hydrophilic characteristics of heparin contributed to the significant decrease in WCA, which dropped to ~29°in heparin coated samples. The enhanced hydrophilicity promotes cell proliferation and adhesion.

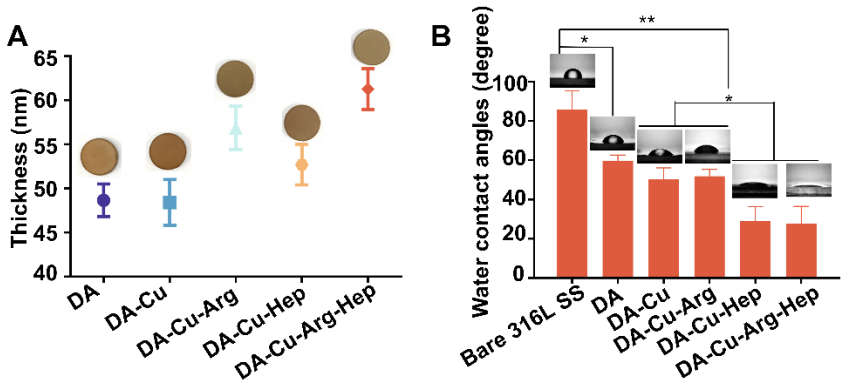

Fig. 2-10. (A) Coating thickness. (B) WCA of each surface. The nano-thin coating

modification improve the surface hydrophilicity.

Next, an angioplasty balloon was used to enlarge the coated stents to test the mechanical durability of the DCAH coating (Fig. 2-11). SEM was used to observe for any fracture formation on each sample.[58] The DCAH coating was compact and homogenous both prior to and after balloon dilatation. The coating showed no apparent breaks after balloon inflation and diameter growth, suggesting sufficient flexibility to tolerate deformation. Subsequently, 30 days fluid flush was used to evaluate the DCAH coating's long-term stability under fluid flow. In Fig. 2-12A, the coating remained uniform and continuous. And EDX (Fig. 2-12B) showed the coating had remarkable long-term durability was further supported by the clear distribution of chemical elements. All of these findings show that the DCAH coating was successfully prepared and that it could resist to long-term fluid flow.

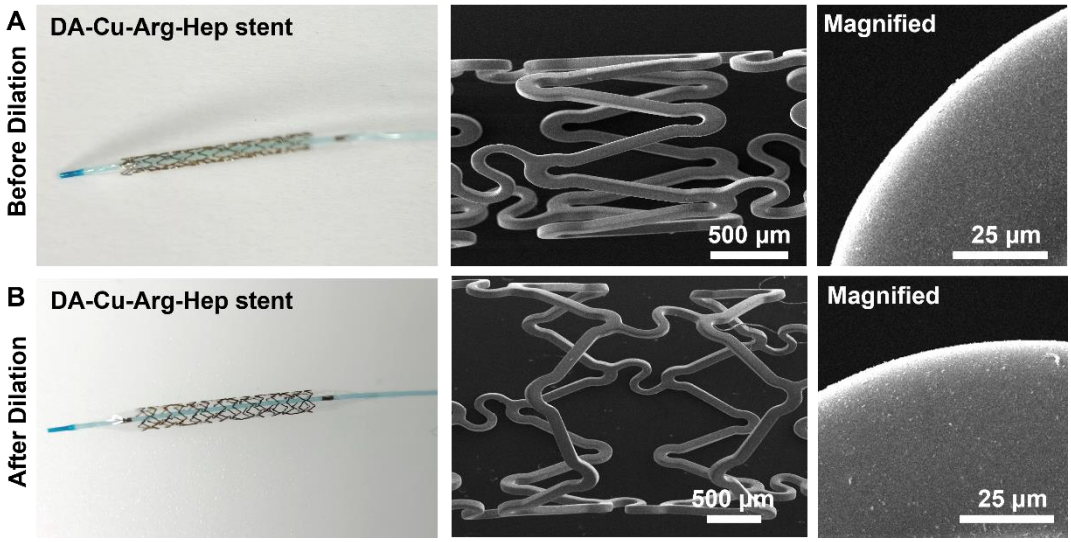

Fig. 2-11. Representative images and SEM micrographs of a DCAH coated stent (A) before and (B) after dilation. The coating showed no cracks after dilation.

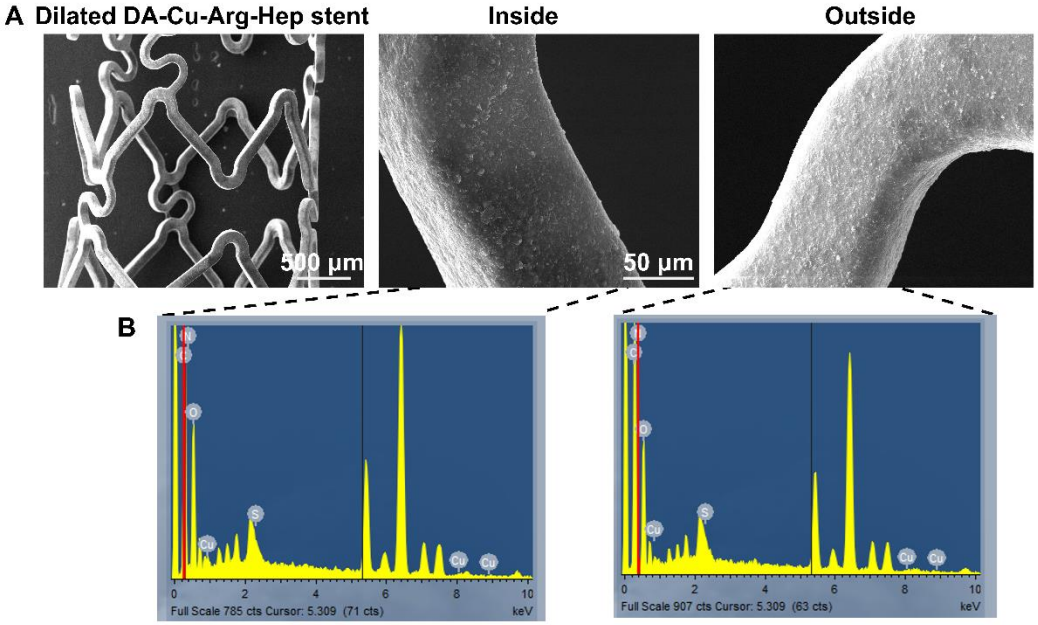

Fig. 2-12. (A) SEM micrographs of a dilated DCAH-coated stent after PBS flow for 30 days. (B) EDX spectra of the DCAH coating. The coating possessed good stability after long-term flush.

2.3.2 Evaluation of NO production from the DCAH coating

To confirm the effects of heparin, eNOS block tests were conducted by using the NOS inhibitor L-NMMA.[100] Fig. 2-13A illustrated the addition of L-NMMA suppressed eNOS (black column), whereas the DCH and DCAH groups showed a considerable increase of eNOS in the absence of L-NMMA (orange column). Following eNOS suppression, NO generation was reduced as shown in Fig. 2-13B and C, where it was represented by low quantitative data (black column) and no NO fluorescence signal. Only the DCA and DCAH groups displayed substantial NO levels when eNOS inhibition was removed. DCAG had the largest NO quantity (~ 28 µM) and the most visible fluorescent signal because of heparin's enhanced eNOS activity. These studies confirmed the effect of heparin on eNOS increase and the generation of NO by arginine.

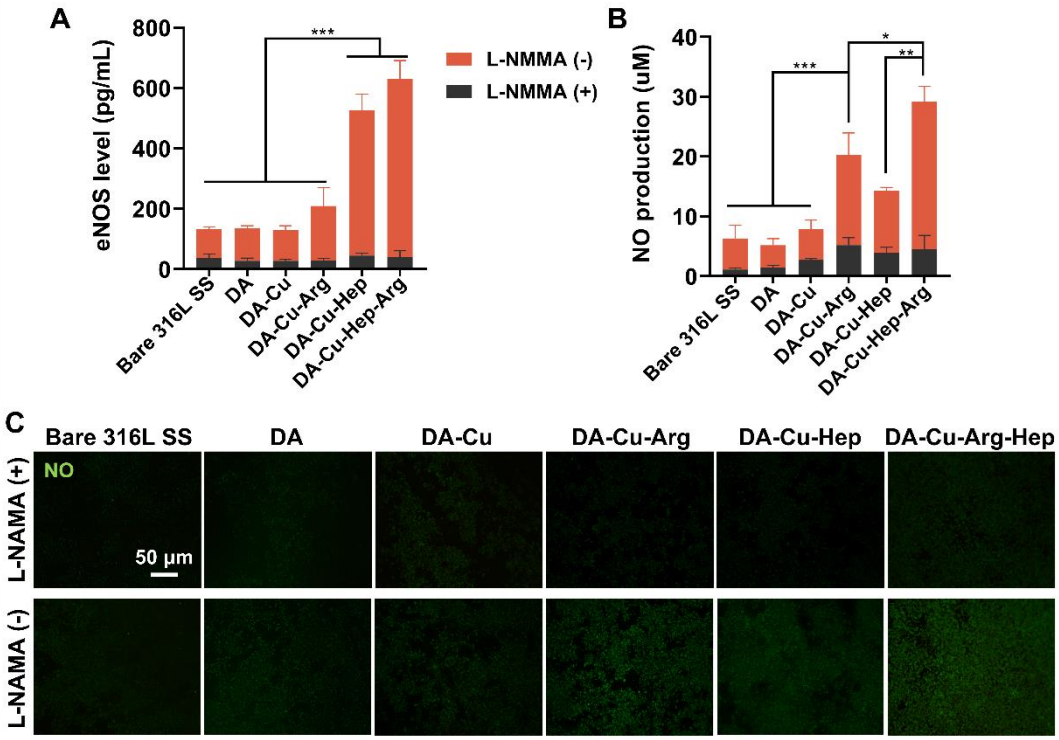

Fig. 2-13. (A) eNOS level of HUVECs on each sample containing or lacking the NOS inhibitor L-NMMA to evaluate eNOS-enhancing ability of heparin. (B) NO production from each sample with or without L-NMMA to evaluate eNOS-mediating NO production form arginine. (C) NO production in HUVECs (green signal) measured by the NO tracing probe.

When immersed in PBS (contained NO donors), significant NO production could be observed in DCAH during a 30-day period (Fig. 2-14A), while there was no NO production in the bare samples. Arginine and heparin grafting had no influences on the catalytic NO generation by Cu catalytic effect, as demonstrated by the similar amounts of NO generated by both the DC and DCAH coatings.

Subsequently, NO production in HUVEC was assessed with NO donors (Fig. 2-14B). The bare and DC samples were unable to produce NO without NO donors, while the DCAH coating continually produced NO due to the synergistic interaction of arginine and heparin, which had a significant fluorescence signal (Fig. 2-15).

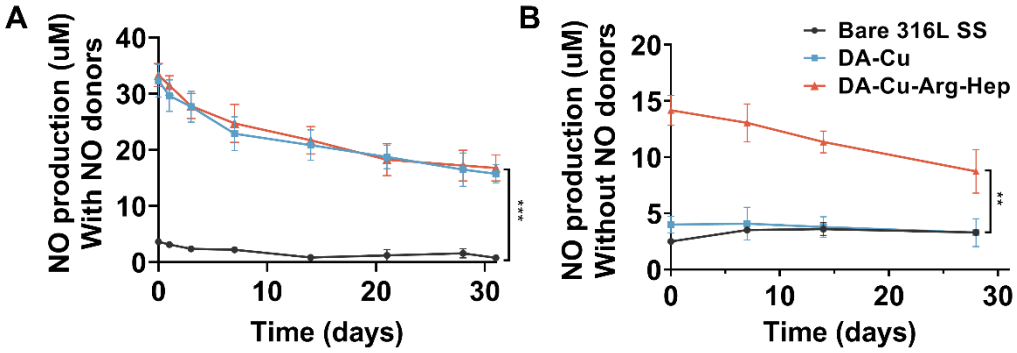

Fig. 2-14. (A) 30 days' NO production by bare, DC and DCAH with NO donors. (B) NO production without NO donors. The proposed coating had long-term NO production.

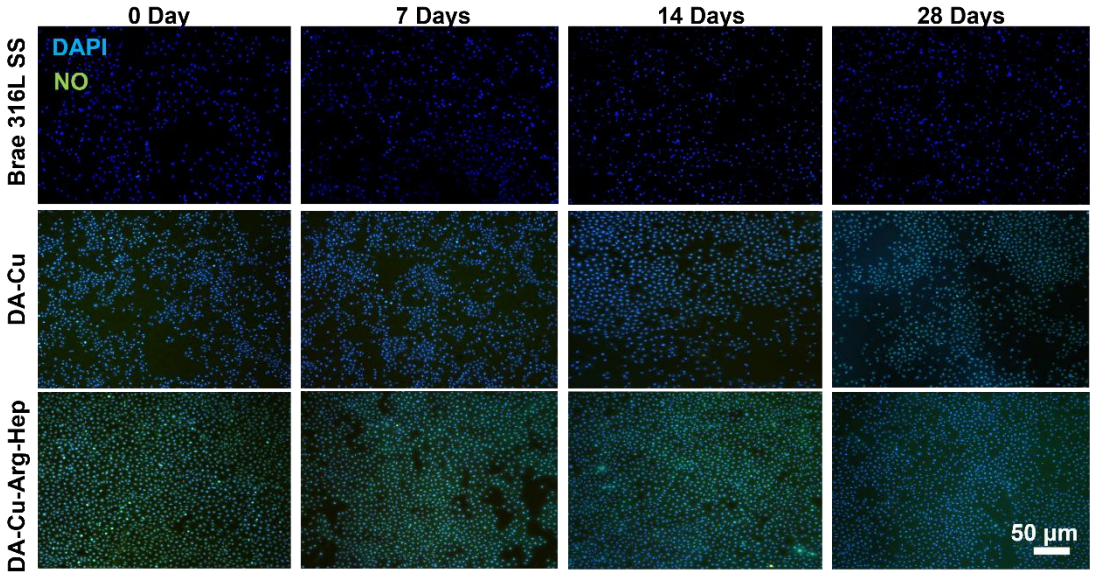

Fig. 2-15. NO (green fluorescence) in HUVECs induced by DC and DCAH with NO donors, as traced by the NO fluorescence probe.

2.3.3 Evaluation of the growth of ECs and SMCs

For implanted stents, the relationship between ECs and SMCs with their milieu is essential.[101] The endothelium can rebuild itself more easily with ECs proliferation.[102] On the other hand, excessive SMC growth causes extracellular matrix deposition, which leads to neointimal hyperplasia.[103] eNOS and NO promote EC growth and restrict SMC proliferation, offering a special benefit for endothelium regeneration and restenosis prevention.[104, 105]

2.3.3.1 Evaluation of HUVEC proliferation

Without NO donors, HUVEC growth was inhibited on bare, D, and DC-coated groups (Fig. 2-16), whereas DCA and DCH groups showed increased proliferation. Because arginine and heparin generate an EC-friendly environment, the DCAH coating exhibited the strongest effect.

With NO donors, due to catalytic NO synthesis by Cu, the EC growth on the NO-generating coating was boosted (Fig. 2-17A). The DCAH group had the strongest effect on HUVEC growth. When ECs were cultured on DCAH for 72 h, all of its surface was covered in cells. Quantitative results (Fig. 2-17B) showed that DCAH enhanced HUVEC proliferation by 3.12 times when compared to the bare samples.

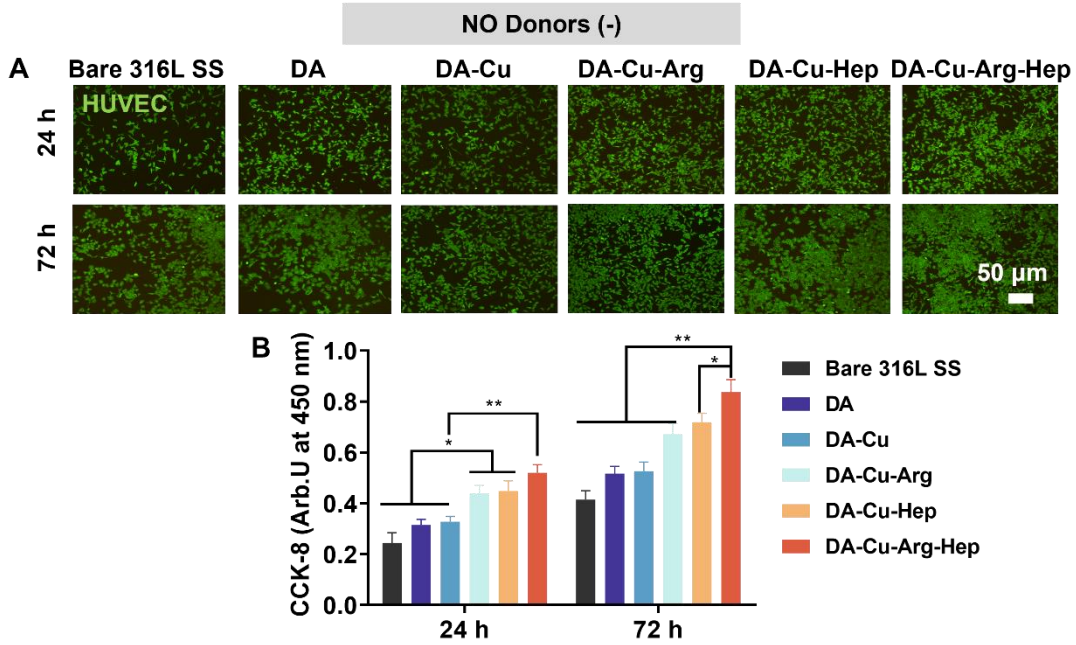

Fig 2-16. (A) Fluorescence images of HUVECs without NO donors. (B) CCK-8 assay results for the proliferation of HUVECs without NO donors. DCAH support EC growth without NO donors.

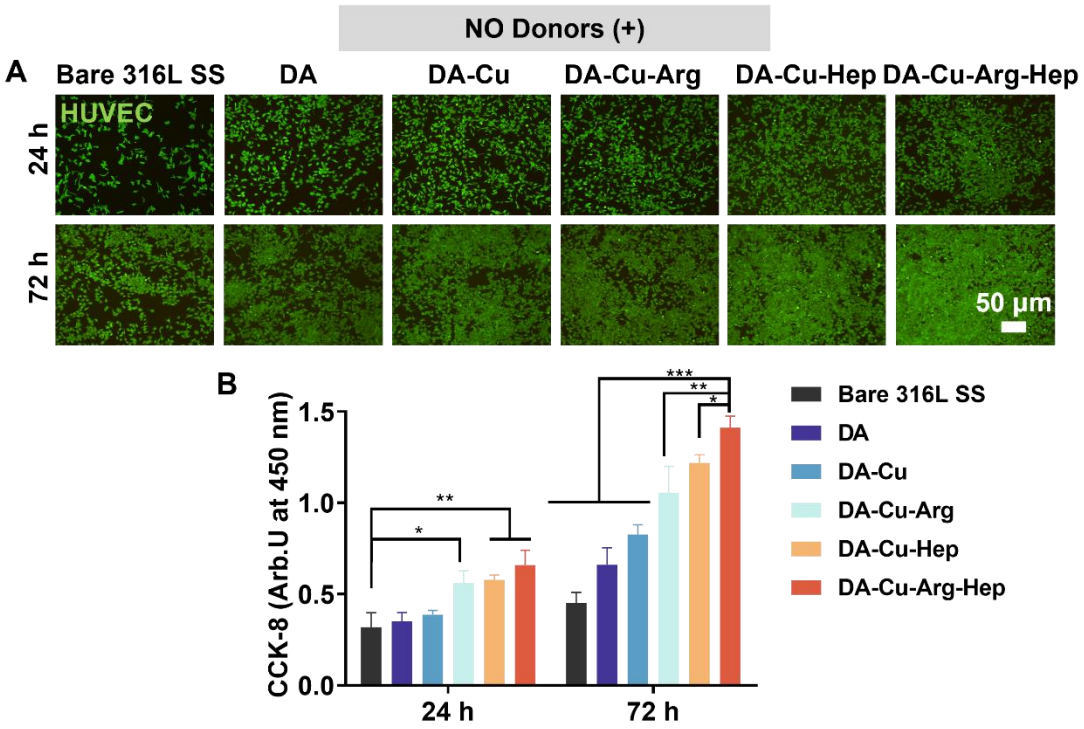

Fig. 2-17. (A) Images of HUVECs with NO donors. (B) CCK-8 assay results for the proliferation of HUVECs with NO donors. DCAH had the strongest effect on EC growth with NO donors.

The eNOS level and NO generation were then assessed to confirm the EC growth mechanism, because eNOS is a crucial protein of ECs that can encourage EC proliferation and convert arginine into NO.[66, 88] In Fig. 2-18A, the eNOS level was increased by DCAH group. Without NO donor, the level of eNOS increased from 0.16 0.27 U/mL (in bare and DCAH); while with NO donor, 0.18 U/mL and 0.32 U/mL NOS could be found in bare and DCAH respectively.

Further analysis was performed on the cellular generation of NO. As shown by Fig. 2-18B, without NO donors, the DCAH coating was able to generate a significant amount of NO at 0.24 ± 0.01 nM, which also showed a strong green fluorescence signal (Fig. 2-18C). When NO donors were present, all Cu-containing coatings showed a significant increase in NO content, and DCAH had the highest NO concentration (0.31 ± 0.02 nM), which was 2.05 times greater than the bare group with the maximum fluorescence intensity. In conclusion, the DCAH coating ensured an EC-friendly milieu by contributing to the elevated eNOS level and the synergistic NO generation of Cu and arginine.

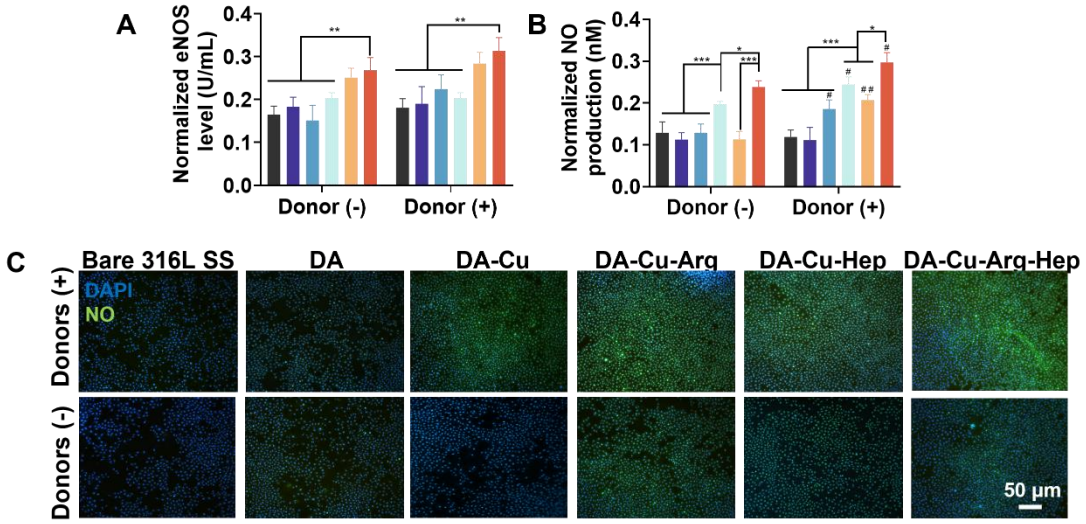

Fig. 2-18. (A) eNOS concentration in HUVECs. (B) NO production in HUVECs. (C) Fluorescence images demonstrating NO production in HUVECs. The increased eNOS expression and NO production illustrated the mechanism of enhanced EC growth.

2.3.3.2 Evaluation of HUASMC proliferation

Then, we investigated the SMC inhibitory effects of coatings by examining the adherence and growth of HUASMC. In the absence of NO donors, HUASMCs had good growth (Fig. 2-19). Because heparin has SMC-suppressive qualities, the development of HUASMCs was decreased in the DCH and DCAH groups.[88] In the presence of NO donors, the NO generating groups showed a considerable inhibition of HUASMC growth, and the strongest inhibitory impact was shown by DCAH, which was 2.27-fold greater than the bare surface.

Heparin and NO-induced elevation of cGMP serves as an illustration of the SMC inhibitory mechanism.[106-108] In Fig. 2-20C, the cGMP amount was significantly reduced in the bare, D, DC, and DCA groups when NO donors were not present, but it increased in the DCH and DCHA groups. When NO donors were present, Cu-containing coatings displayed elevated cGMP levels that were closely correlated with the NO flow. The DCAH group had the highest level of cGMP expression, suggesting a significant inhibitory action on SMCs. These results suggested that the DCAH effectively inhibited the growth of HUASMC and prevent the formation of intimal hyperplasia.

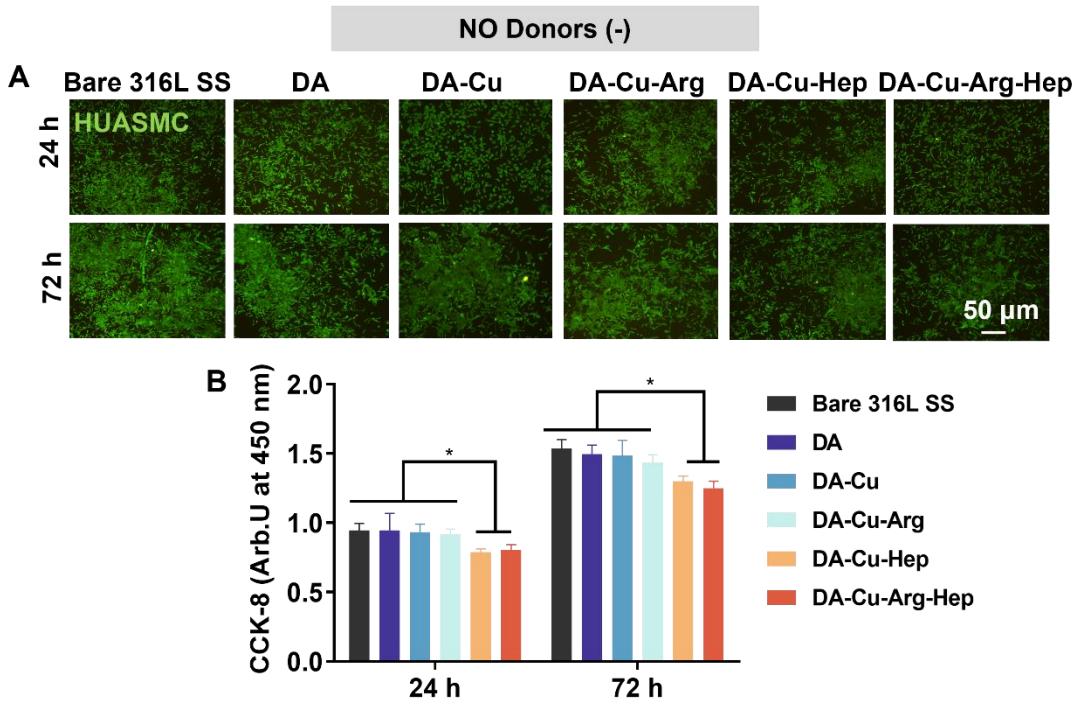

Fig 2-19. (A) Fluorescence images of HUASMCs without NO donors. (B) CCK-8 assay results for the proliferation of HUASMCs without NO donors. DCAH showed slightly SMC inhibition without NO donors.

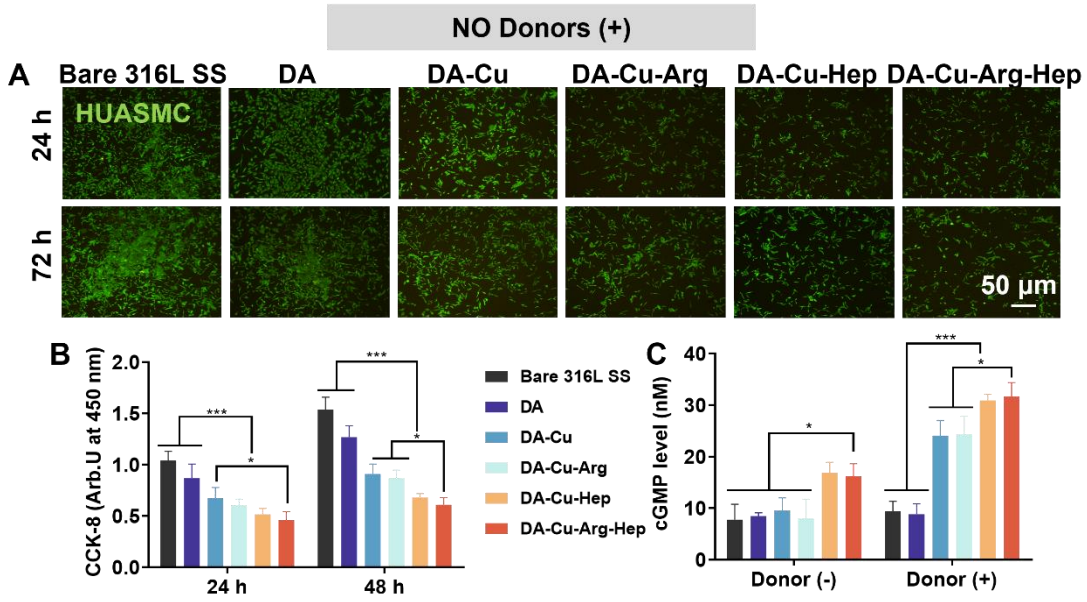

Fig. 2-20. (A) Images of HUASMCs with NO donors. (B) CCK-8 assay results for the proliferation of HUASMCs with NO donors. DCAH suppressed SMC growth with NO donors.

2.3.3.3 Cytotoxicity of DCAH coating

The cytotoxicity of the proposed coatings was examined using a live/dead staining technique, in which red signal indicated dead cells and green signal indicated living cells. In Fig. 2-21, the lack of apparent dead cell appearance on the stent coatings' surface indicated that the coatings did not exhibit any overt cytotoxicity, and the pattern of cell growth agreed with the CCK-8 data.

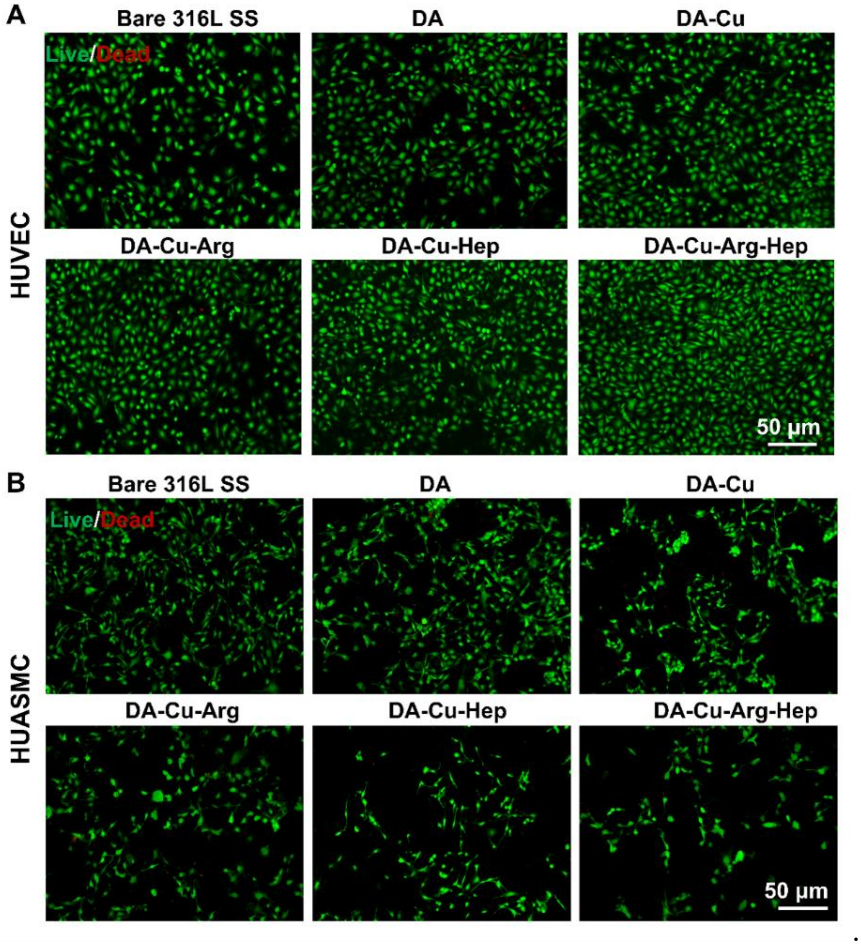

Fig. 2-21. Live/dead staining of (A) HUVECs and (B) HUASMCs with NO donors. Live cells: green; dead cells: red. Almost no dead cells could be found in our proposed coatings.

2.3.3.4 Evaluation of the migration of HUVEC and HUASMC

After stenting, EC migration from nearby endothelial tissue is necessary for endothelial repair.[89] Conversely, SMC over-migration can be detrimental and often leads to in-stent restenosis and hyperplasia.[109] As shown in Fig. 2-22A and B, limited cell

movement was observed on bare and D (26.60 and 41.25 μm) surfaces. On the other hand, HUVEC motility was considerably enhanced (109.01 μm) by the DCAH coating when NO donor supplements were added. The bare and D surfaces only slightly inhibited the migration of HUASMCs (Fig. 2-22C and D). In contrast, the migration of HUASMCs was suppressed by all NO-generating groups. In DCAH group, the migration (20.45 μm) was lower than that in the bare sample. According to these findings, DCAH would offer a friendly surface to encourage EC migration while preventing SMC movement to ensure a healthy reendothelialization after stent implantation.

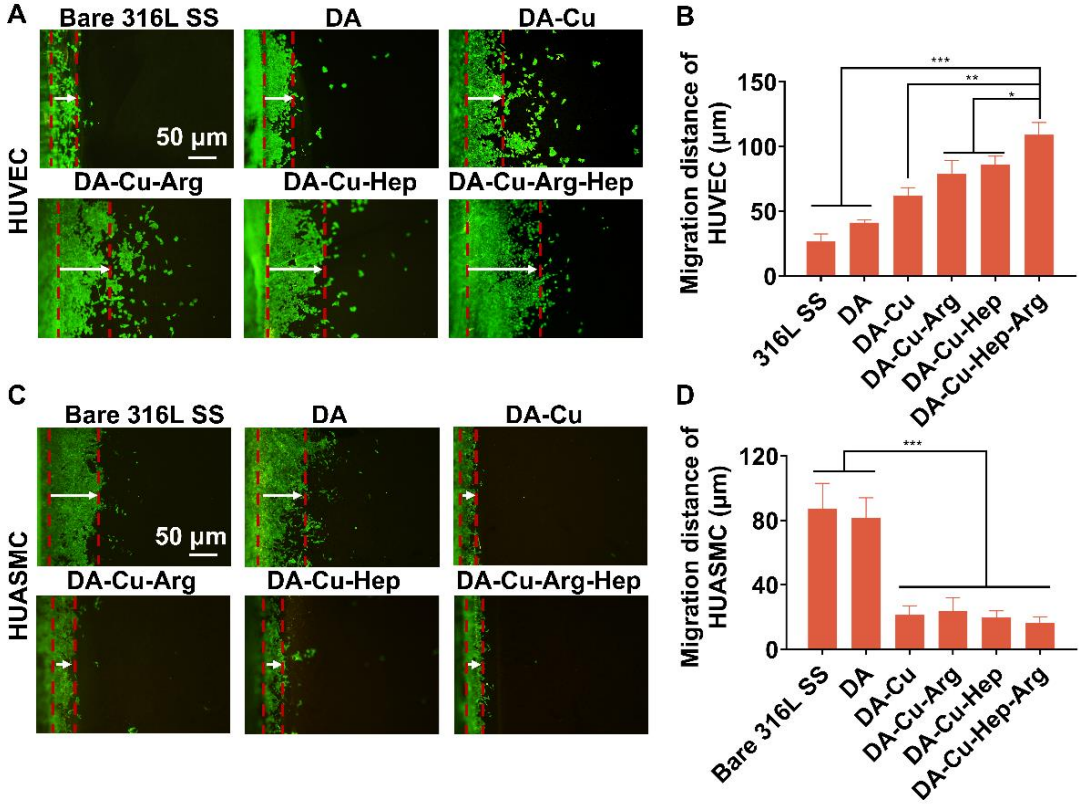

Fig. 2-22. (A) Actin fluorescence staining and (B) migration distance of HUVECs. (C) Actin fluorescence staining and (D) migration distance of HUASMCs.

2.3.3.5 Evaluation of the competitive growth of ECs over SMCs

Since the formation of new endothelium and the inhibition of restenosis depend on the competitive growth of EC over SMC, we co-seeded these two cells on each sample and observed their fluorescence (green: EC, red: SMC).[110] As seen in Fig. 2-23A and B,

the bare samples had few HUVECs (green) and were primarily covered in HUASMCs (red). The DCAH coating, on the other hand, showed a higher green fluorescence with a reduced red signal. The EC/SMC ratio raised from 0.504 to 1.814 (bare to DCAH), with 1.81-times higher HUVEC growth compared to the bare samples at 72 hours, indicating excellent selectivity for HUVEC growth (Fig. 2-23C and D). To sum up, these findings confirmed the effectiveness of the DCAH coating in promoting the growth of endothelial layer and preventing SMC related restenosis.

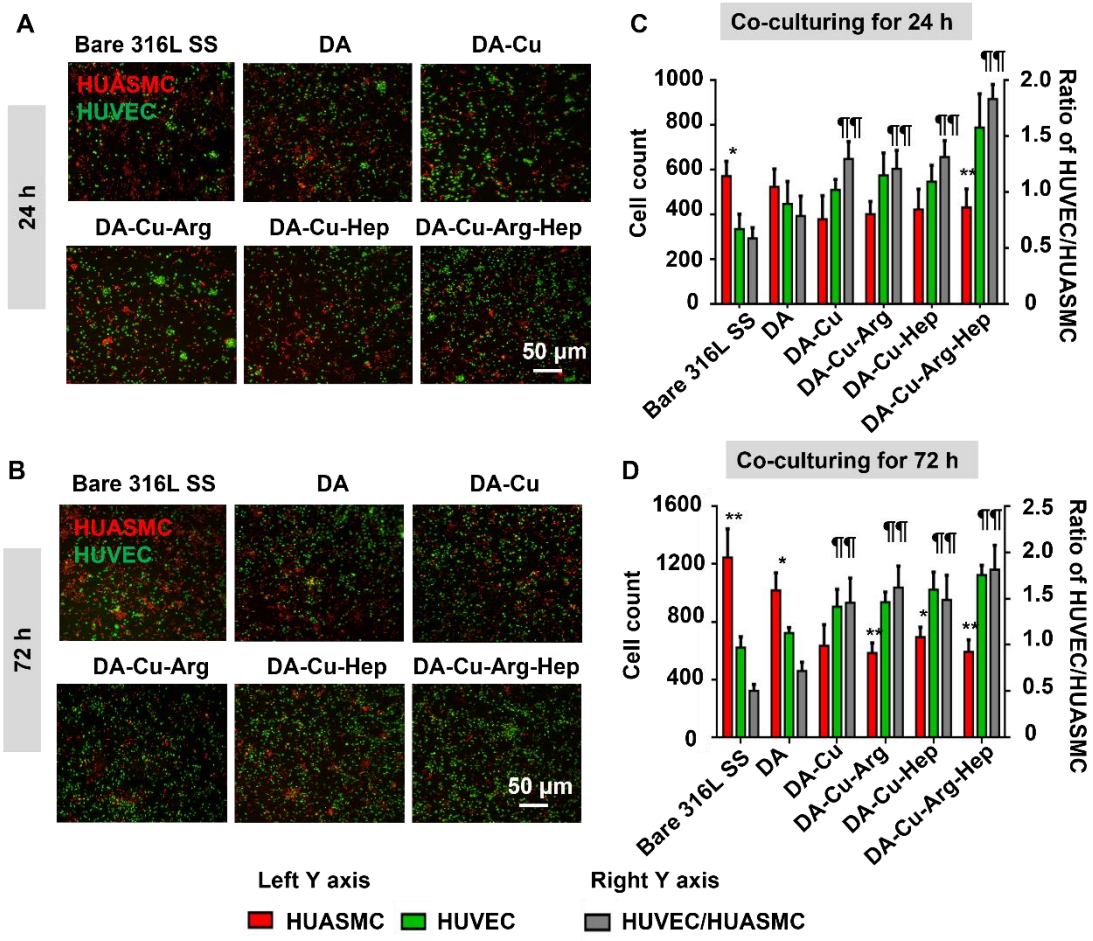

Fig. 2-23. Fluorescent images of HUVECs and HUASMCs after (A) 24 and (B) 72 h of co-culturing. The ratio of EC to SMC cultivated on various coatings after (C) 24 and (D) 72 h of co-culture. *, **, ***(HUVEC vs. HUASMC) and ¶, ¶¶, ¶¶¶ (vs. 316L SS) represent $p < 0.05$, 0.01 and 0.001.

2.3.4 Evaluation of platelet behaviors on DCAH coating

2.3.4.1 Evaluation of heparin bioactivity and fibrinogen adhesion

Generally, FXa is bound by active heparin, which lowers the amount of leftover FXa in platelets. As a result, the presence of FXa can indicate heparin activity.[111-114] The absorbance dropped from 1.028 (bare) to 0.489 (DCH) and 0.412 (DCAH) (Fig. 2-24), indicating the anti-FXa effect was increased by heparin grafting. DCH and DCAH both retained good bioactivity with a decreased amount of FXa.

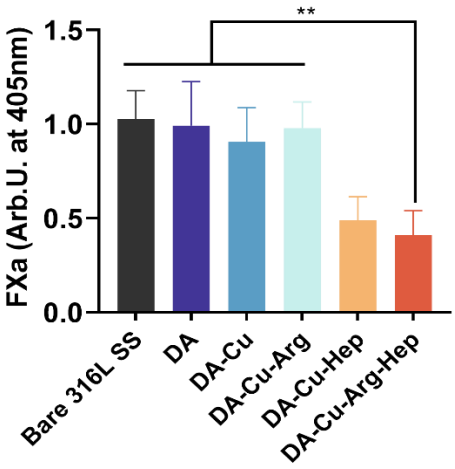

Fig. 2-24. Anti-FXa activity of each coating after incubated with PPP for 2 h.

The fibrinogen adsorption experiments were used to examine the coating's antithrombotic properties.[115, 116] All samples exhibited fibrinogen adsorption. The D, DC, and DCA groups displayed larger adsorption amounts than the bare surface, which may have been brought on by the amino groups and enhanced surface roughness. On the other hand, because of the anticoagulant effect of heparin and the decreased amine groups caused by heparin, fibrinogen adsorption was reduced in the DCH and DCAH groups.

We then carried out the fibrinogen activation assay. The bare and D groups both exhibited strong fibrinogen activation, while the groups that could produce NO showed decreased activation potential. We hypothesized that NO may affect the structure of the protein and obstruct the activation mechanism. With the greatest potential to prevent thrombosis, the DCH and DCAH groups demonstrated the largest inhibitory effect on fibrinogen activation among all the other groups.

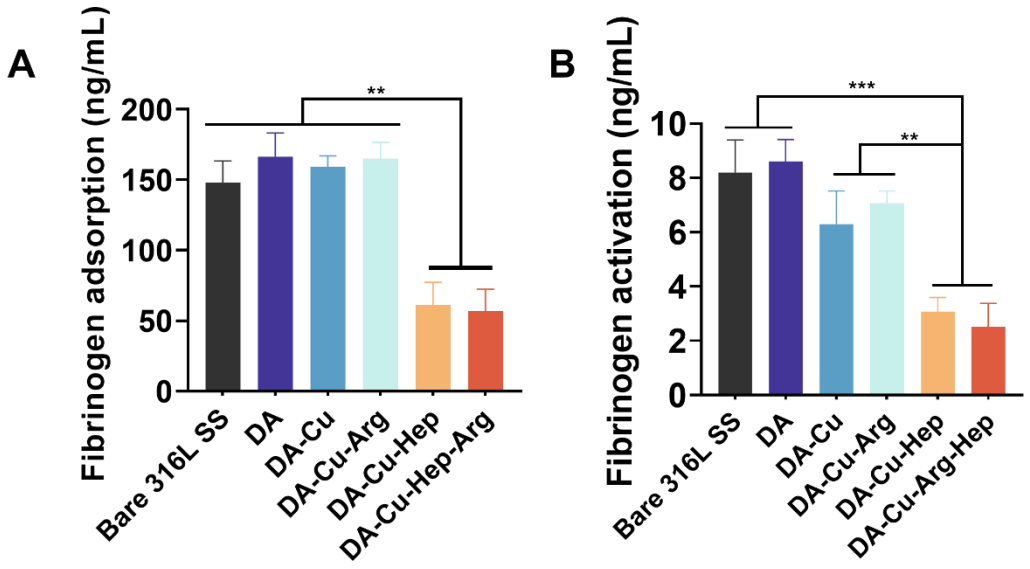

Fig. 2-25. Relative quantification of fibrinogen adsorption (A) and activation (B) exposure on each sample.

2.3.4.2 Evaluation of platelets adhesion

Following implantation, thrombosis results from activated platelets adhering and aggregating quickly at the site of implantation.[88, 117, 118] In Fig. 2-26, neither the bare nor the D samples prevented platelets from adhering. The DCAH coating, on the other hand, dramatically reduced platelet adherence with NO donors.

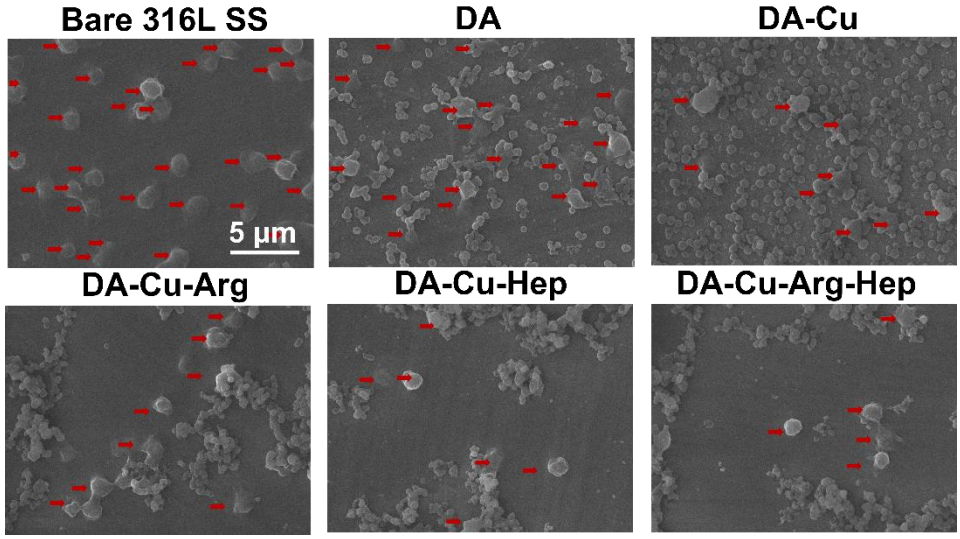

Fig. 2-26. SEM images depict platelets' adhesion on uncoated and coated surfaces. The red arrow pointed to platelets.

Adherent platelets were further seen using a fluorescent dye. The least amount of platelet adherence was observed in the DCAH coating (Fig. 2-27), suggesting that it has significant anti-thrombotic potential. The levels of cGMP in platelets were evaluated to investigate the mechanism of platelet inhibition (Fig. 2-28). There are fewer platelets on the surface of DCAH because of a considerable increase in cGMP production caused by the coating.

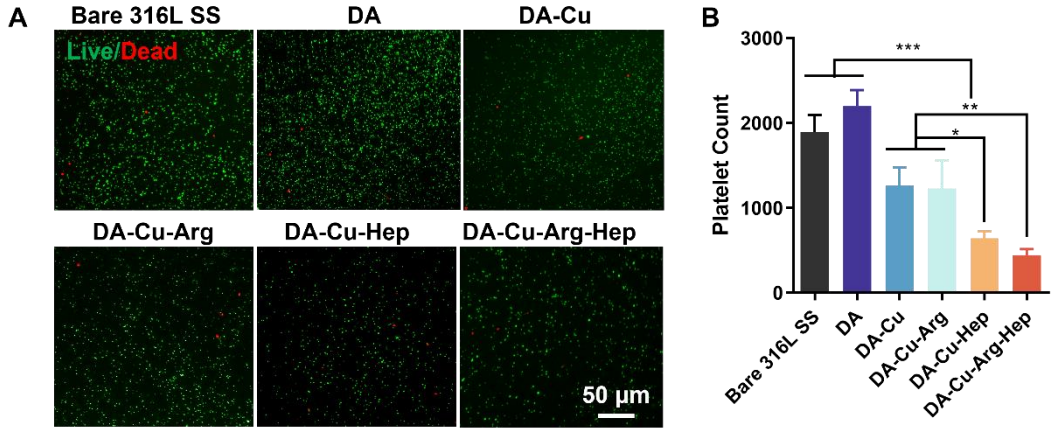

Fig. 2-27. (A) Fluorescent staining of platelets on different surfaces. (B) The quantity of adherent platelets presented in every sample.

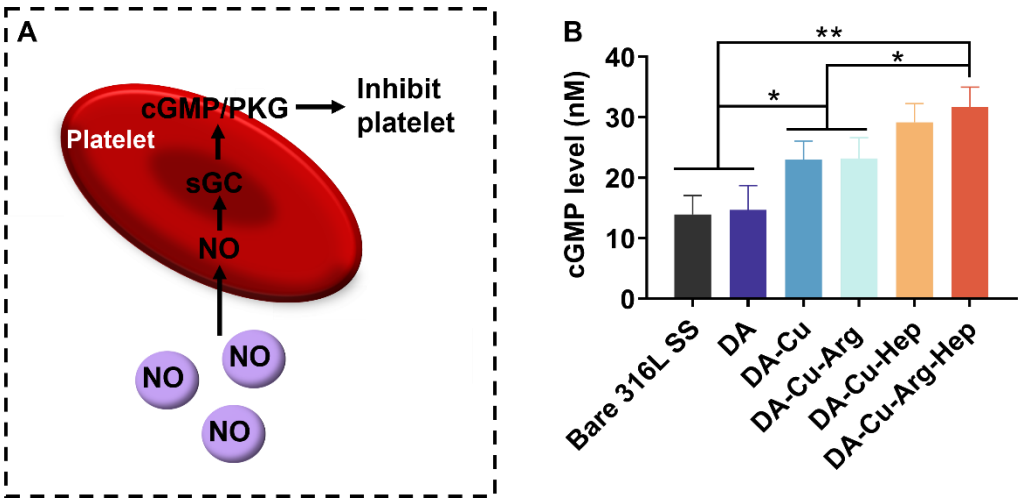

Fig. 2-28. (A) The mechanism of platelet inhibition is that NO can activate cGMP pathway. (B) cGMP concentration in platelets.

2.3.5 Anti-thrombogenic efficacy of DCAH coatings

An investigation into each sample's anti-thrombotic properties under blood flow was conducted using a rabbit model.[64, 104] As seen in Fig. 2-30A, each group's blood

flow, occlusion, and thrombosis development rates were assessed. Blood clots were completely obscured bare and D samples. In contrast, the DCAH group had less thrombus on the wall, while other coated foils had obvious wall clots. Additionally, the group treated with DCAH had a lower thrombus weight (10.46 mg) than the bare group (58.32 mg) (Fig. 2-30B). SEM (Fig. 2-31) showed that the coated surfaces had fewer platelets than the untreated ones, although the bare surface had many attached platelets. The most notable platelet reduction was shown by the DCAH coating, which also showed a decrease in blood clot formation.

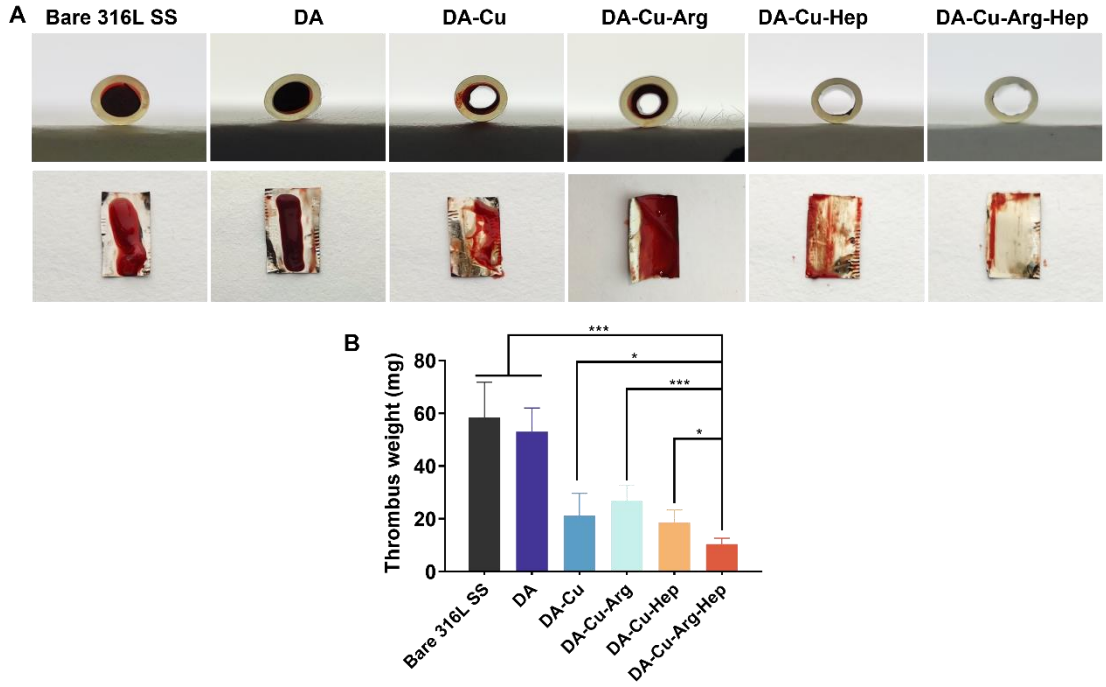

Fig. 2-30. (A) Images of sample installed PVC tubes, where the DCAH sample had very few blood clots onto its surface. (B) Thrombus weight of each group.

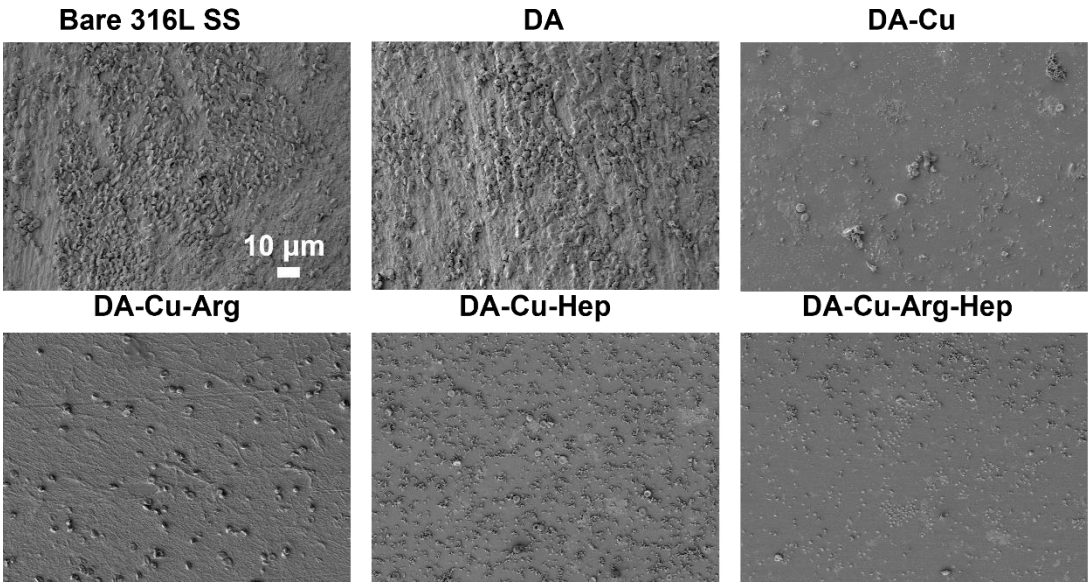

Fig. 2-31. SEM observation of thrombus of each group. DCAH had the least platelet adhesion.

The occlusion rates (Fig. 2-32A) of the bare and D samples were remarkably high at 94.5 ± 2.5% and 93.7 ± 2.2%, respectively. In contrast, there was almost no occlusion in the DCAH samples (7.4 ± 4.5%). Blood flow can be restored more easily because of the reduced thrombus and occlusion. The blood flow rate in the DCAH was higher (85.6 ± 6.3%) than in the bare foil (10.1 ± 7.6%) and D (11.5 ± 3.1%). The blood flow in the DCAH foils was 1.48, 1.60, and 1.35 times higher than in DC, DCA and DCH, respectively (Fig. 2-32-B).

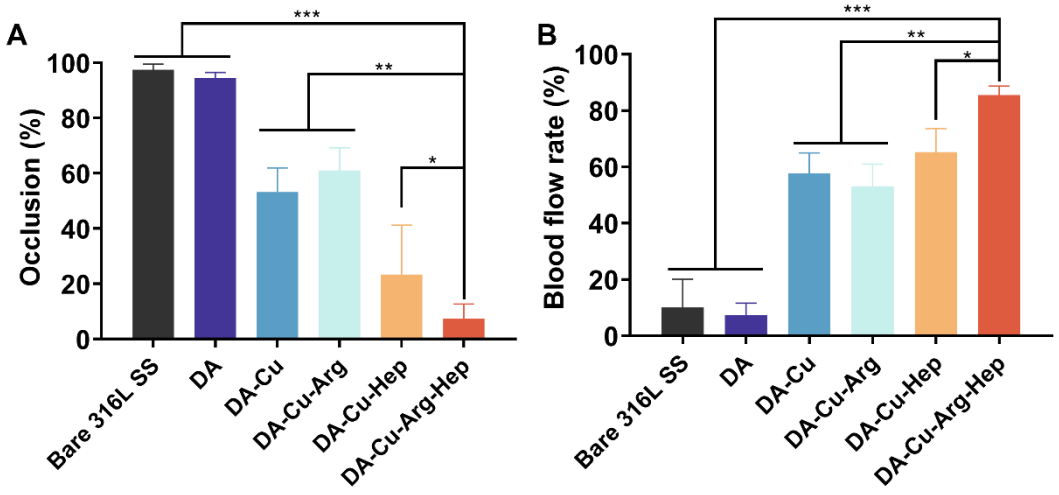

Fig. 2-32. (A) Percentage of circuit occlusion. (B) Blood flow rate through different samples.

Because the arginine's cations were exposed to the surface, the DCA group exhibited a higher occlusion rate and blood clot weight than the DC and DCH groups. Heparin could augment the antithrombotic effects by shielding the positive charge of arginine and raising the eNOS level to enable the synthesis of NO from arginine. In comparison to the other groups, the DCAH coating showed the best antithrombotic effects.

2.3.6 Effectiveness of DCAH coatings *in vivo*

Coated stents with DCAH coating were used to treat anti-restenosis in rabbit iliofemoral arteries. [119, 120] The endothelialization of the DCAH stents, which were covered in a thin endothelium, was verified by the SEM data at one week (Fig. 2-33). On the other hand, there was obvious platelet adherence on the surface of the control stent with limited endothelium covering.

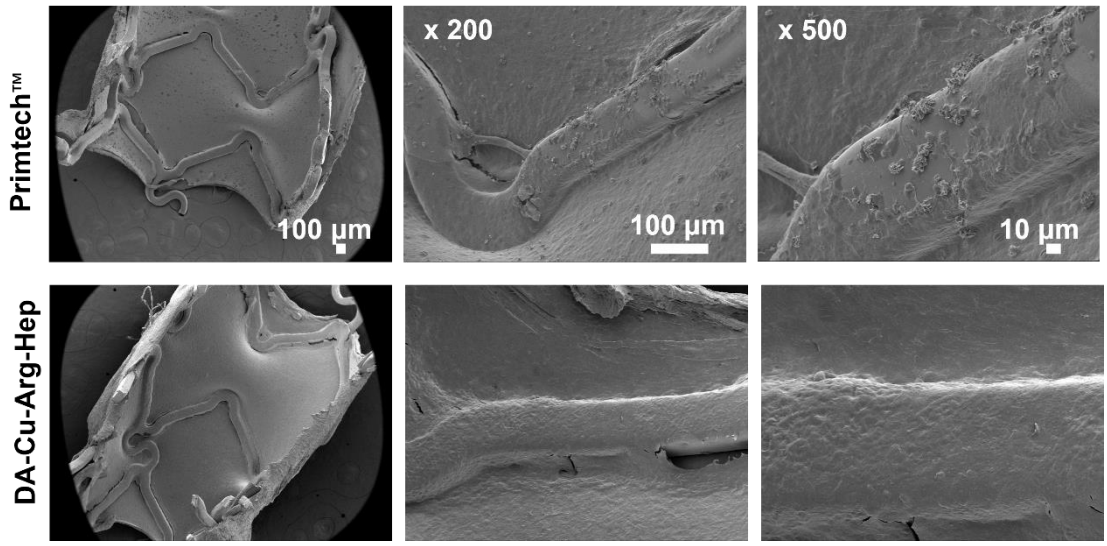

Fig. 2-33. SEM pictures of stents one week after insertion. Significant platelet adhesion could be found in the control group.

To assess the anti-restenosis of the DCAH coating in more detail, histomorphometric analysis was carried out (Fig. 2-34). Following 1 month of implantation, the control stent's lumen did noticeably thicken, while the DCAH coated stents continued to have a clear outline. The DCAH coated stents showed much less restenosis at three months, while the control stents showed severe neointimal hyperplasia. The DCAH coated stents showed a considerable reduction in neointimal

area and stenosis percentage (Fig. 2-35).

The control stents showed a significant increase in restenosis (3.09 ± 0.56 mm^2) indices at 3 months, reaching to 47.37 ± 5.23%. On the other hand, the mean neointimal area and neointimal stenosis percentage of the DCAH coated stents were 1.21 mm^2 and 23.69%, respectively. Taken together, these findings showed that the DCAH stents endowed a friendly environment that lowers restenosis and maintains the long-term CVS viability.

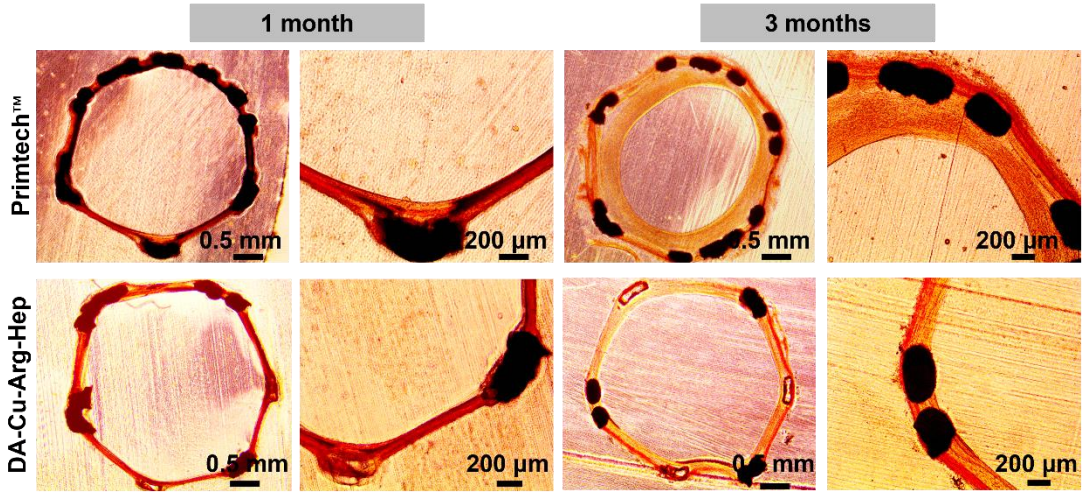

Fig. 2-34. Observation of restenosis.

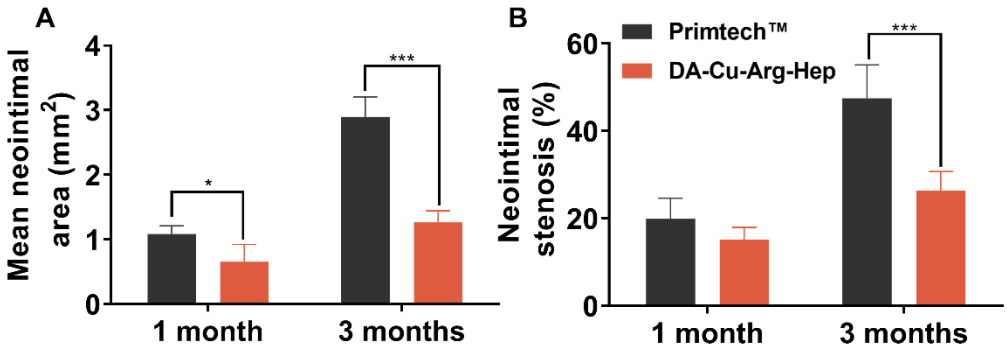

Fig. 2-35. Analysis of stenosis and the neointimal region of stents implanted

2.4 Summary

Using a dipping method, we created a DCAH coating for CVS, enabling mass manufacture and broad application in many contexts, including public hospitals. Cu, arginine, and heparin were coupled in this stent coating to create NO synergistically under all circumstances. Specifically, when endogenous RSNOs were present, Cu

stimulated the formation of NO. In the absence of RSNOs, heparin increased the activity of eNOS, then it broke down arginine into NO. As a result, this coating enhanced endothelial functions by producing NO regardless NO donors' presence (Fig. 2-36), possibly reducing the requirement for systemic RSNO administration following stenting. Moreover, the DCAH coating inhibited platelet adhesion and SMC proliferation while promoting EC growth. Animal studies showed that the DCAH coating greatly increased blood and tissue compatibility, serving a useful treatment for thrombosis and restenosis. Drawing from this, we envision the application of our DCAH coating in CVS, which will yield incalculable benefits for CVD patients, such as reduced postoperative complications and lower expenses for prescription drugs such as arginine administration and extra NO donor supplementation.

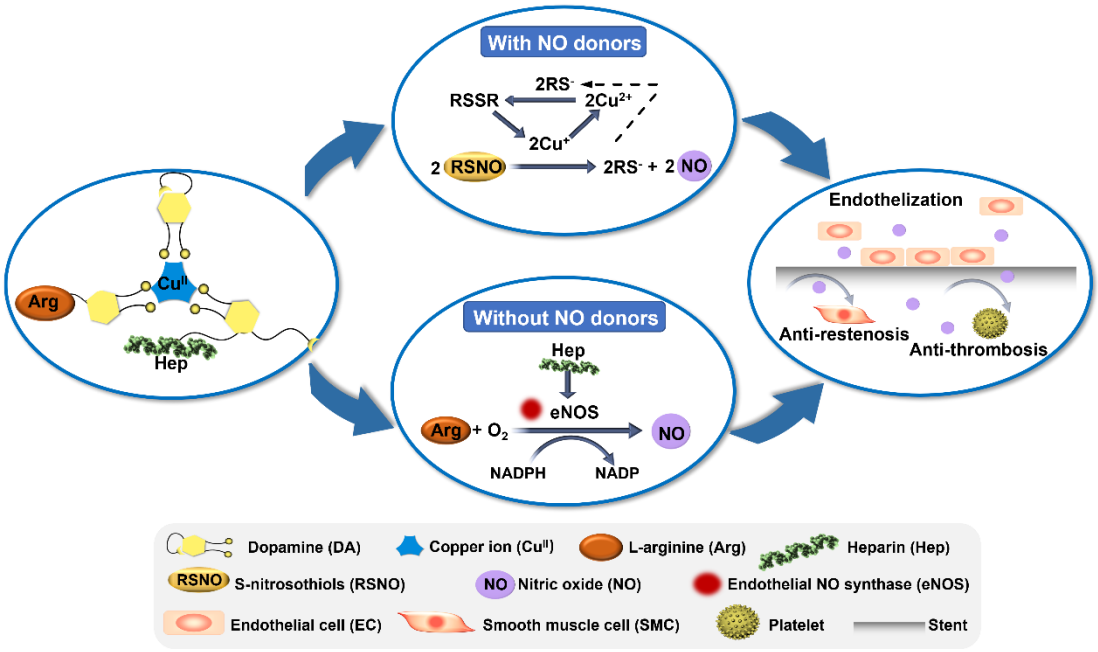

Fig. 2-36. Illustration of the synergistic effect of NO production by DCAH coating. Adequate Cu, arginine and heparin grafting was modified to the dopamine network. Cu sustained the conversion of endogenous RSNOs into NO. eNOS, whose activity was elevated by heparin, could convert arginine to NO in the absence of RSNOs. Following stent implantation, the adequate, continuous, and self-sustaining supply of NO was ensured by the combination of Cu, arginine, and heparin, which rebuilt the endothelium.

Chapter 3 Development of an EC-capturing and NO-producing stent coating for rapid reendothelialization

3.1 Introduction

As a natural barrier, endothelium can impede unfavorable cellular behaviors, such as activated platelet adherence and excessive SMC over-proliferation from the defect site and migration into the vascular lumen. When the endothelium loses its integrity, the above-mentioned behaviors occur, ultimately leading to thrombosis and restenosis.[62] Therefore, to restore vascular homeostasis effectively, an ideal CVS should address every cellular event following stent implantation while promoting endothelial repair.

In the natural vascular endothelium, the presence of glycosaminoglycan and EC-synthesized NO maintains an anticoagulant environment. The glycocalyx, specifically heparin, promotes NO production from arginine by elevating the expression of eNOS.[62, 121] The produced NO activates the cGMP pathway to further suppress platelet adhesion/activation and SMC migration/proliferation.[99] However, NO alone may not rapidly facilitate early-stage reendothelialization, as this process requires the rapid recruitment of ECs.[122-124] VEGF has been recognized as a key mediator in cell-matrix interactions. Numerous studies have demonstrated that ECs can directly adhere to and spread thanks to VEGF during angiogenesis.[125-127] Additionally, the binding of VEGF to EC receptors (including α3β1 and αvβ3 integrins) activates a number of important intracellular signaling molecules, including matrix metalloproteinases (MMPs) and focal adhesion kinase (FAK). Subsequently, the activated molecules mediate EC migration, proliferation, and tubule formation.[128-130] VEGF binding also leads to the activation of some signal pathways to promote angiogenesis (Fig. 3-1).[131, 132] Hence, the incorporation of VEGF into the stent coating holds great potential for promoting EC adherence and facilitating reendothelialization.

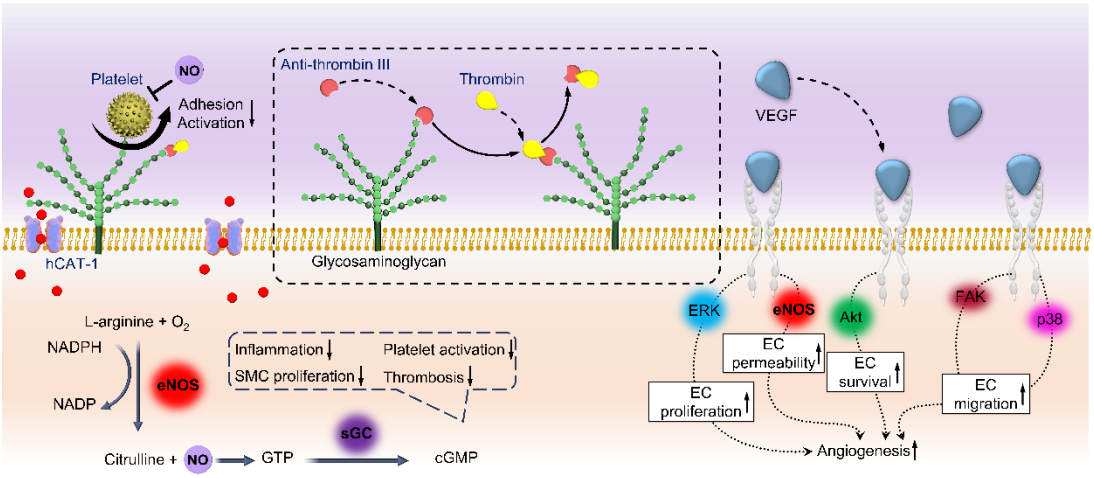

Fig. 3-1. Natural endothelium has a glycocalyx surface and contains arginine transporter, where heparin has anticoagulant properties and can increase the eNOS activity to decompose arginine into NO. The produced NO can stimulate NO-cGMP pathway to inhibit thrombosis and restenosis. Meanwhile, the presence of VEGF promotes EC adhesion and the recognition between VEGF and EC receptor will stimulate various pathways to promote EC growth as well as angiogenesis.

In our last project, we designed a NO-producing stent coating, which consisted of antithrombotic glycosaminoglycan surface with NO-synthesizing ability via Cu catalysis and arginine decomposition. Interestingly, when a substantial number of ECs adhered to the coating surface, they spontaneously produced NO, closely resembling the behavior of a healthy endothelium. Building upon these findings, in this chapter, we incorporated VEGF into the coating to facilitate rapid adhesion of ECs.

Here, we reconstructed the endothelial structure on CVS stents by fabricating a coating consisting of a dopamine (DA)/hexamethylene diamine (HD)-Cu network and NO precursor arginine, endothelial glycocalyx heparin as well as VEGF. The DA/HD-Cu network, resembling the adhesive properties of a mussel foot cuticle, securely attached to the stent surface through catechol binding, and HD provided ample amino groups for functional biomolecular grafting. The complexed Cu had GPx-like catalytic activity that converted the endogenous RSNOs into NO. Arginine served as an NO precursor, releasing NO in the presence of eNOS, whose activity was enhanced by

heparin. Finally, covalent immobilization of VEGF facilitated rapid EC adhesion, accelerating reendothelialization. Moreover, the aggregation of ECs on the stent surface spontaneously produced NO, forming a barrier that prevented platelet adhesion and inhibited SMC growth, thereby mimicking the protective functions of a healthy endothelium (Fig. 3-2).

The DA/HD-Cu-arginine-heparin-VEGF (AHV) coating replicated the essential features of the endothelial structure. It promoted EC adhesion and provided a sustained release of NO, thereby addressing the temporal cellular responses associated with stent implantation (i.e., rapid reendothelialization, platelet inhibition, and long-term suppression of SMC proliferation and migration). Our AHV coating has the potential to overcome clinical challenges related to uncontrolled thrombus formation and restenosis. Importantly, it eliminates the need for additional growth factors or NO precursors, thereby enhancing the long-term effectiveness and safety of CVS.

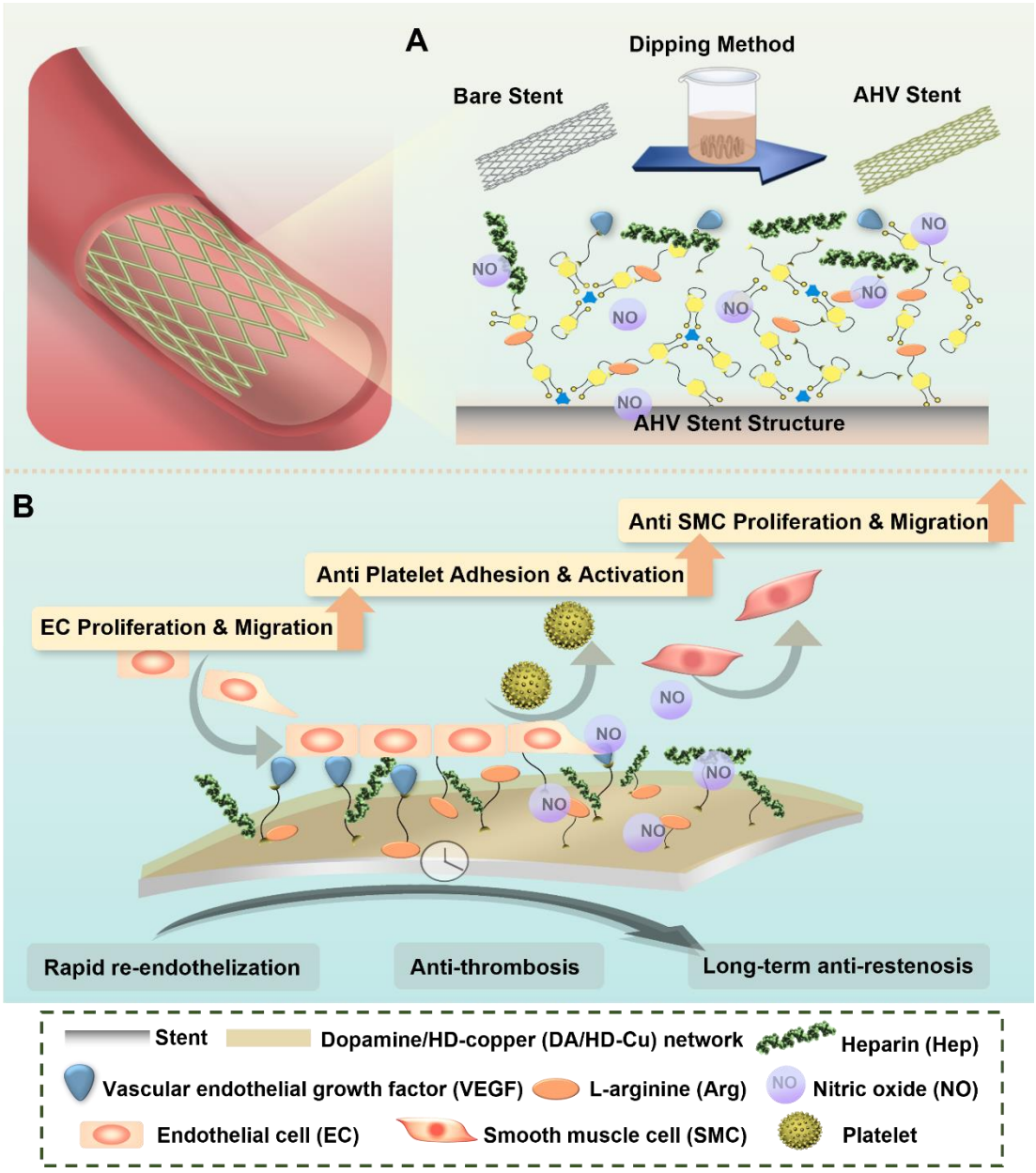

Fig. 3-2. (A) The process of dipping was used to create the AHV coating. The DA/HD-Cu base could adhere onto the stent surface, where HD provided abundant grafting sites and Cu worked as NO catalyst. The grafted Arginine and Heparin guaranteed the production of NO when endogenous NO donor was insufficient, while the immobilized VEGF would adhere EC rapidly. (B) After *in vivo* implantation of AHV stent, the grafted VEGF could promote fast EC adhesion and facilitate EC migration and proliferation, which contributed to rapid re-endothelization at the early stage to establish a barrier to defend against platelet adhesion. The Cu catalyzed endogenous RSNOs into NO. With the elevated eNOS activity by heparin, NO precursor arginine

can be converted into NO, which guaranteed sufficient NO production under any physiological conditions (with or without NO donors in blood). The sustained NO production inhibited SMC migration/proliferation at the later stages of stent implantation for a long time, reducing the risk of restenosis.

3.2 Materials and Methods

3.2.1 Fabrication and characterization of AHV coating

3.2.1.1 Fabrication of AHV coatings

We prepared the AHV coatings on 316L SS substrates by an organic-free dipping method. First, the bare substrates were placed into a 1 mg/mL DA solution with 5 μg/mL $CuCl_2$ and 2.44 mg/mL HD to form the DC network.[59] Afterward, we immersed the DA-Cu-coated sample into 1 mg/mL arginine solution for 24 h to form the DCA surface. Heparin was pre-activated, and the DCA samples were dipped into the activated heparin solution for another 24 h to form the DCAH coating.[62] Lastly, the coated samples were dipped in 0.5 μg/mL VEGF solution for 12 h to fabricate the AHV samples.

3.2.1.2 Characterization of the AHV coatings

The possible anti-ferromagnetic coupling of Cu ions in AHV coating was analyzed using electron paramagnetic resonance (EPR, Bruker, Germany). The possible reaction mechanism between the DA and Cu molecules was investigated using MALDI-TOF-MS. The elemental composition was analyzed with XPS. Chemical structures were determined using ATR-FTIR. The masses of covalently immobilized arginine, heparin, and VEGF were quantified using QCM-D equipment. The hydrophilicity of each surface was examined by measuring WCA. The mechanical stability of the AHV coating was assessed using a balloon dilation test. SEM images of the AHV stents before and after expansion were taken to analyze the surface morphology change. The long-term stability of AHV coating under fluid flow for 30 days was carried out. The surface morphology change was observed by SEM.[58]

3.2.2 *In vitro* long-term NO production

The AHV-coated samples were immersed in PBS with NO donors at 37˚C.A total NO assay kit was used to measure the amount of NO produced. To evaluate the NO production from arginine, the samples immersed in PBS were taken out, and the5×10^4 cells EC were seeded on each surface without NO donors. The NO amount was determined and traced by NO kit and fluorescence probe.

3.2.3 *In vitro* biological properties of AHV coating

3.2.3.1 Assessment of the growth of EC and SMC onto the developed coatings

The *in vitro* experiments received helps from Miss Di SUO. Cells at 5×10^4 cells/cm^2 were seeded onto B, V, AV, HV, AH, and AHV samples. After 24 h and 72 h, samples were stained using FITC-phalloidin for fluorescence observation. Cell proliferation on different coatings was assessed *via* CCK-8 assay. For HUVECs, the adherent cells were counted by ImageJ 1.8.0 software after 2 h. To investigate the mechanism of increased growth of HUVECs, after incubation for 72 h, NO production was measured, and an ELISA kit was used to measure the eNOS. To investigate the mechanism of inhibition of HUASMCs, the cGMP level was measured by ELISA kit.[84]

3.2.3.2 Competitive growth of EC over SMC

Before being seeded onto the B, V, AV, HV, AH, and AHV coatings, HUASMCs and HUVECs were sained by different dyes. The EC (green) and SMC (red) mixtures (5×10^4 cells/cm^2) were mixed in equal volume and seeded onto each sample. After 24 h and 72 h, the cells were observed, and the cell number was calculated.[95]

3.2.3.3 Investigation of EC and SMC migration

The foils were folded symmetrically. The V, AV, HV, AH, and AHV coatings were deposited onto one side while the other remained naked. Then, cells (5×10^4 cells) were seeded on the naked half side for 4 h to form a confluent cell layer. Then, the foils were flipped and incubated for another 24 h with NO donors. The cells were stained by FITC-phalloidin, and the cell migration from the naked side to the coated side was observed

by a fluorescence microscope.

3.2.3.4 Assessment of platelet adhesion

The blood from Sprague Dawley rats was collected by following procedures approved by the Ethics Committee of PolyU. After obtained PRP, and the B, V, AV, HV, AH, and AHV samples were incubated with PRP for 2 h. Afterwards, all samples were fixed and followed by gradient dehydration. The adherence of platelets on each sample was observed by SEM. Triton-X was added for cGMP expressions after a 2-hour incubation period, and the supernatant was then collected and examined using a cGMP ELISA kit.[62, 96]

3.2.3.5 Competitive adhesion of ECs and platelets

Before being seeded onto the B, V, AV, HV, AH, and AHV coatings, HUVECs and platelets were traced by fluorescence dyes. The HUVEC (green) and platelet (red) mixtures were mixed in equal volume (5×10^4 cells) and seeded onto different surfaces. After 2 h, the number of adhered cells was calculated.

3.2.4 Assessment of the AHV coatings' anti-thrombogenic effectiveness

All the animal experiments were approved by the Ethics Committee of Southern Medical University. The animal experiments were assisted by Mr. Qing MA from Prof. Zhilu YANG's research group. We established an AV-shunt model in rabbit. Before the animal experiments, the B, V, AV, HV, AH, and AHV foils were curled and fixed into a PVC tube. The left arteries and right veins of rabbits were exposed after general anesthesia and barbering. Their vessels were connected to the prepared PVC blood transfusion system for 2 h, and then the samples were harvested and fixed for SEM examination. Cross-sections of each circuit were photographed, and the occlusion rate was calculated. Moreover, the thrombus was collected for photographing and weighing.[88, 97]

3.2.5 Evaluation of *in vivo* therapeutic efficacy of the AHV coatings

New Zealand white rabbits were anesthetized in this experiment, and the iliofemoral arteries were exposed. Commercially used Primtech™ (bare) stents and the AHV- stents were separately inserted onto the left and right iliofemoral arteries. For 1 week, CD31 fluorescence staining, and SEM were used to observe the reendothelialization of each sample. For 1 and 3 months, one part of the samples was fixed for SEM detection, and the other was stained.[98, 99]

3.2.6 Statistical Analysis

T-test with GraphPad Prism 8.0 software was used for statistical analysis, *, **, *** represented a statistically significant difference ($p < 0.05$, 0.01, and 0.001, respectively).

3.3 Results and discussions

3.3.1 Fabrication and Characterization of AHV coating

Bare 316L SS (B), DA-Cu-VEGF (V), DA-Cu-arginine-VEGF (AV), DA-Cu-heparin-VEGF (HV), and DA-Cu-arginine-heparin (AH) served as control groups. We first characterized the chemical properties of the resultant AHV coatings. First, EPR spectrum was used to investigate the coordination reaction between DA and Cu (Fig. 3-3A). DA had little signal, while a strong signal at 3440 mT was found in DA-Cu, indicating successful coordination. Then, MS analysis was carried out (Fig. 3-3B). The peaks at 402 m/z indicated the possible structures of dopamine and copper, which further confirmed the chelation of Cu and DA derivatives. XPS was further used to analyze the chemical element distribution (Fig. 3-3C). All groups showed a strong Cu signal, and the AHV group possessed additional S signal (belonging to heparin), confirming the alteration of chemical composition in the AHV-coated samples. To investigate the chemical structure of AHV coating, ATR-FTIR was also used. In Fig. 3-3D, the fundamental structure of each coating was identical (with same -COOH, -NH, -OH and -C=C peaks), which demonstrated the formation of DA network. In AHV samples, -C=N and -S=O bonds were detected by the peaks around 1600 and 1000 cm^{-1}, which belonged to arginine and Heparin, respectively, indicating the successful

modification with arginine and Heparin. Subsequently, the grafting amount of arginine, heparin and VEGF onto the DA-Cu network were measured. Fig. 3-4 showed around 346 ± 11 ng/cm^2 Arginine, 609 ± 7 ng/cm^2 Heparin and 232 ± 4 ng/cm^2 VEGF had been conjugated onto the sample surface, confirming the successful fabrication of the AHV coating.

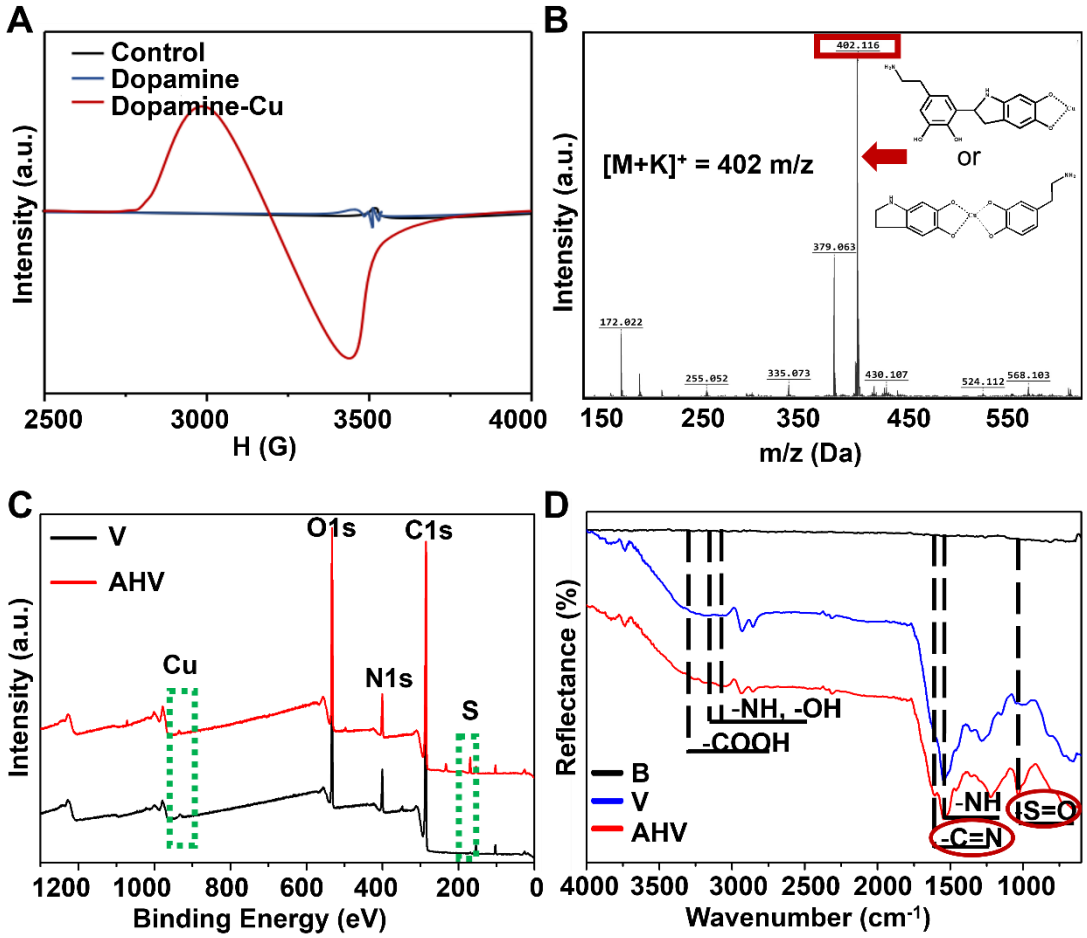

Fig. 3-3. (A) EPR and (B) MS spectra. (C) XPS spectra of V and AHV. (D) GATR-FTIR spectra of B, V and AHV.

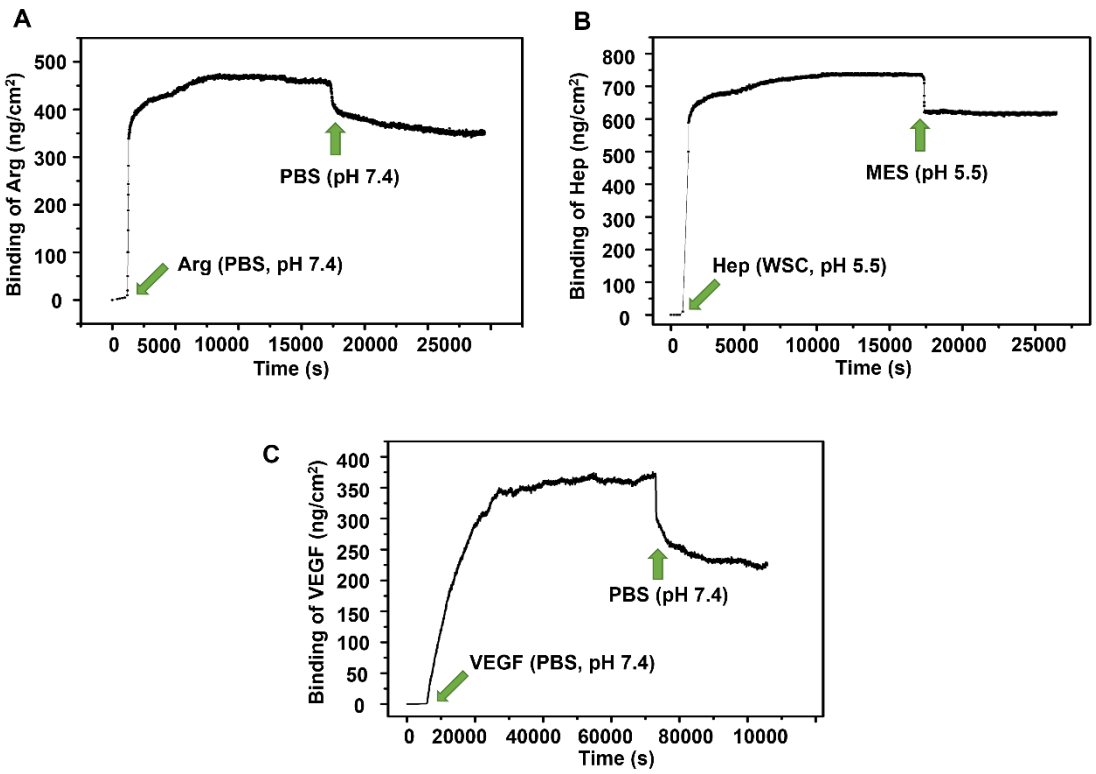

Fig. 3-4. Immobilization of arginine, heparin and VEGF onto DA-Cu measured by QCM-D. The stabilized curve represented the amount of grafting.

Afterward, the physical properties of the AHV coating were studied. The WCA of the bare sample was around 85°, suggesting its surface was hydrophobic (Fig. 3-5A and B).[89] The introduction of arginine, heparin and VEGF led to a significant WCA decrease (around 23°) in AHV samples, indicating improved hydrophilicity, which was conducive to cell adhesion. Furthermore, the AHV coating had a thickness in the nanometer range, at about 53 nm (Fig. 3-5C).[133]

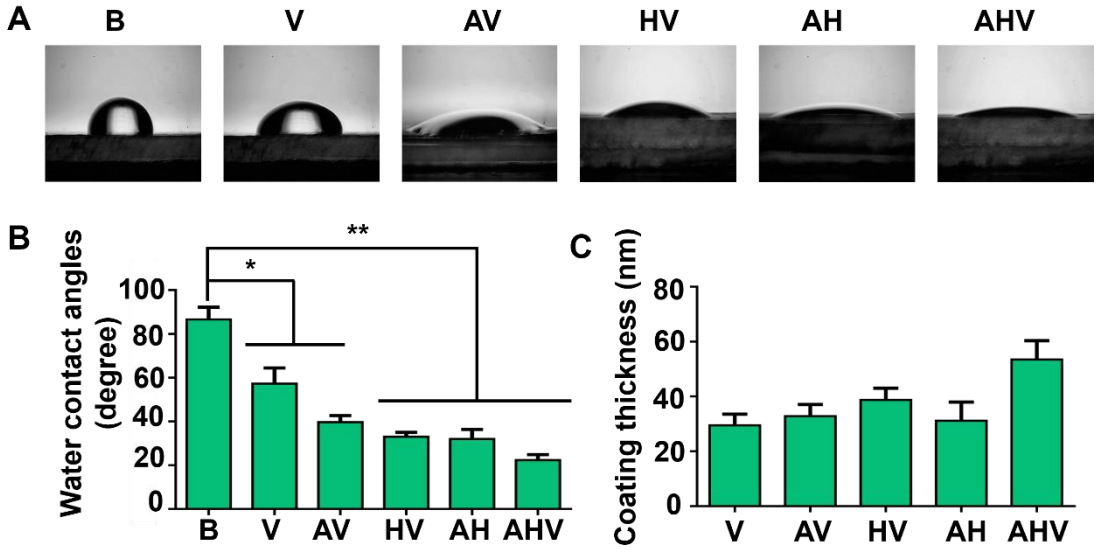

Fig. 3-5. (A) WCA images and (B) quantitative data of bare and coated samples. (C) Thickness of each coating.

A dilated balloon angioplasty was used to study the mechanical stability of AHV coating.[58] SEM showed the AHV coating had no delamination or cracks after dilation, (Fig. 3-6). Moreover, to evaluate the AHV coating's durability over time under fluid flow, SEM observation of dilated AHV stents under 30 days of flush was carried out (Fig. 3-7A). In Fig. 3-7B, the AHV coating was continuous and homogeneous. As shown by EDX spectroscopy (Fig. 3-7C), the AHV coating still showed obvious chemical element distribution (including C, N, O, Cu and S) after PBS flush, suggesting the AHV coating was mechanically strong, chemically stable, and did not peel off.

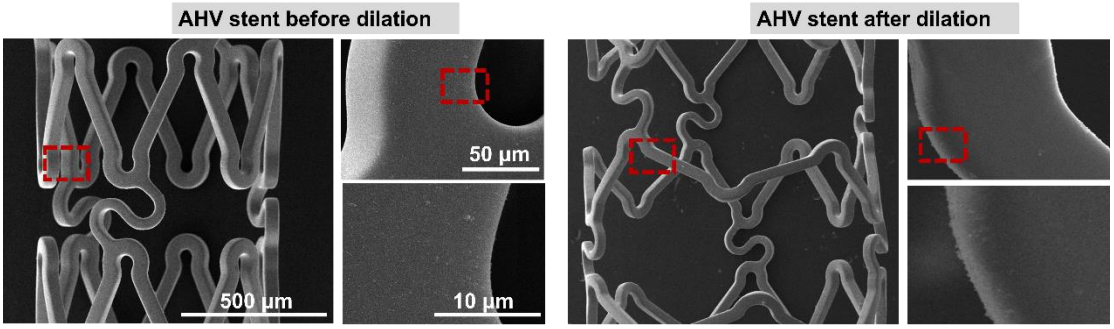

Fig. 3-6. Representative SEM micrographs showing the morphology of AHV-coating. The coating had no cracks after diliation.

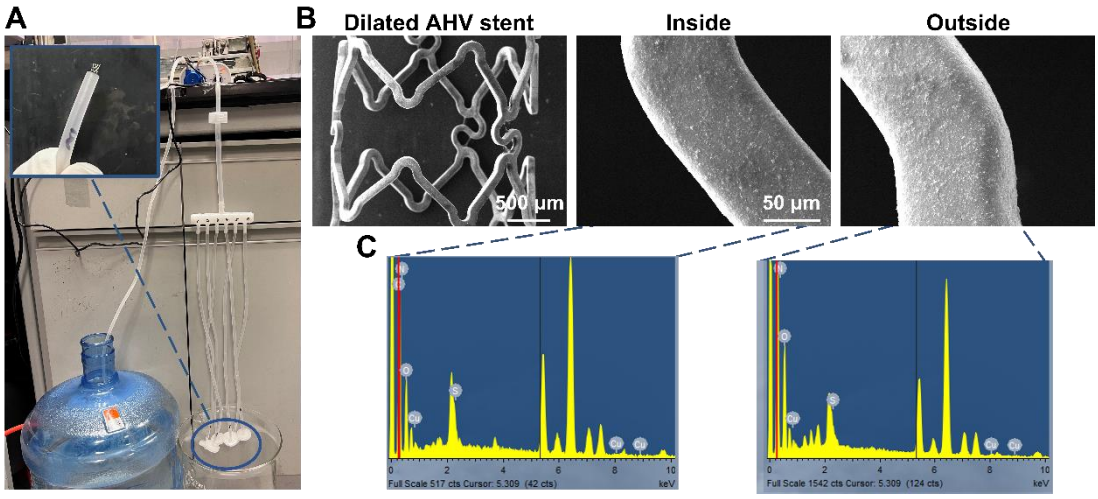

Fig. 3-7. (A) Photograph of PBS flush device. (B) Representative SEM micrographs of dilated AHV-coated stents after 30-day of PBS flush. Note that the coating remained homogeneous after 30-day of flush. (C) EDX spectra of AHV coating.

3.3.2 *In vitro* long-term NO production

Under the chemical reduction effect of GSH, the transition from Cu^{II} to Cu^{I} could catalyze NO production from NO donors such as SNAP. Meanwhile, NO precursors like arginine could release NO under the effect of eNOS in ECs, whose level would be elevated by heparin. These synergistic elements could maintain long-term NO production at any physiological condition (with or without sufficient endogenous NO donors). To investigate NO production from AHV coating by Cu, the dopamine-copper and AHV were placed in NO donors containing PBS solution. According to Fig. 3-8, both DA-Cu and AHV coatings showed more NO production with NO donors, confirming that the modification of arginine, heparin and VEGF did not affect NO production. After immersion in PBS for 30 days, the coated samples could maintain NO production, and the release of NO was about 50.15% of their initial amount.

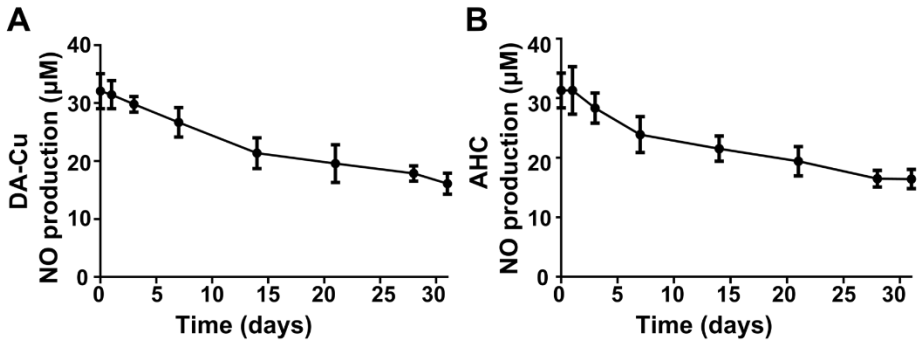

Fig. 3-8. 30 days' NO generation of the (A) dopamine-copper (B) and AHV with NO donors.

Additionally, to investigate NO production from AHV coating by NO precursor Arginine, HUVECs were seeded onto its surfaces without NO donors. The quantitation data (Fig. 3-9A) showed the AHV coating could sustainably support NO generation at the cellular level. The fluorescence images (Fig. 3-9B) exhibited no fluorescence signal in bare samples, while the AHV samples exhibited strong green fluorescence for 28 days, confirming the continuous NO production from the coated samples. Overall, these results verified the AHV coating had long-lasting NO generation independent of NO donors, which suggested potential therapeutic efficacy for long-term inhibition of stent restenosis and thrombosis.

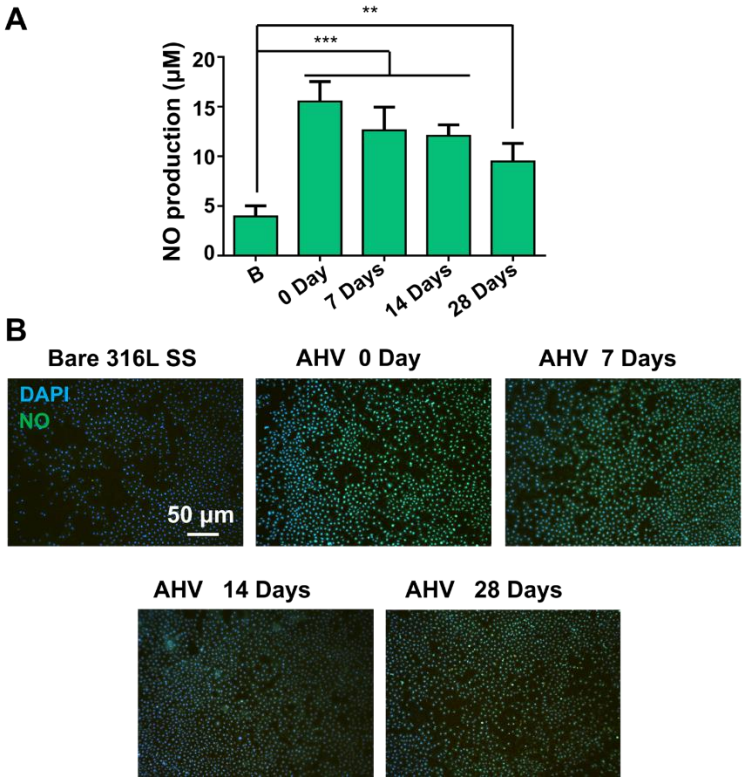

Fig. 3-9. (A) Quantification of NO production by arginine (without NO donors) in HUVECs. (B) Fluorescent NO production by arginine (without NO donors) in HUVECs. The data show that the AHV coating can long term generate NO.

3.3.3 *In vitro* biological properties of AHV coatings

3.3.3.1 Evaluation of HUVEC adhesion

Rapid adhesion of ECs provides necessary conditions for their proliferation and migration to achieve early-stage reendothelialization.[134] To investigate the effect of AHV coating on rapid EC adhesion, HUVECs were seeded on the developed coatings for 2 h. VEGF grafting facilitated EC adhesion for its strong EC-capturing ability.[135, 136] AH and HV showed similar EC adhesion, which may be contributed by the positive charge of arginine. Among all groups, AHV showed the highest cell number (280 ± 21 cells) (Fig. S3A-B), which was 2.02 and 1.62 times higher than B and AH group, respectively, indicating AHV had the potential to promote early-stage reendothelialization.

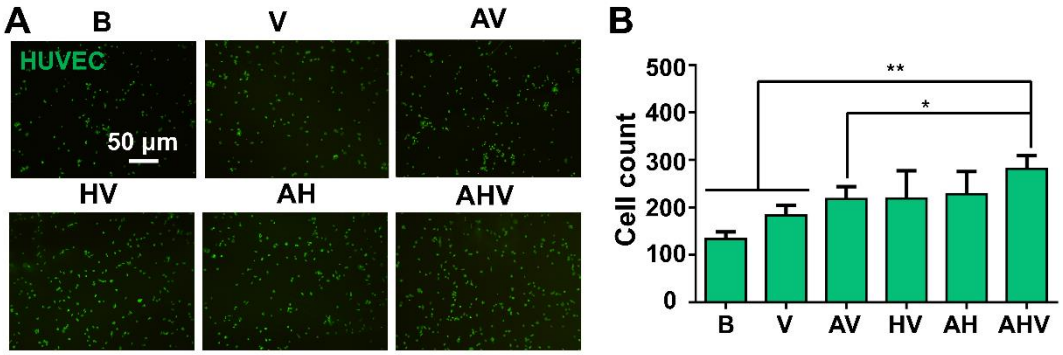

Fig. 3-10. Fluorescence images (A) and cells count (B) of HUVECs after 2 h of culture to evaluate the rapid EC adhesion ability of each sample.

3.3.3.2 Promotion of HUVEC growth

Without NO donors, the HUVEC growth on AHV was enhanced after 72 h, as indicated by the coverage of green fluorescence signal indicating HUVECs (Fig. 3-11A). The CCK-8 results (Fig. 3-11B) also verified the AHV coating had the strongest ability to support HUVEC growth, which was 1.61 times higher than bare samples at 72 h.

In the presence of NO donors, after seeding HUVECs onto each sample for 24 h, the fluorescence images (Fig. 3-12A) exhibited that AHV coating significantly increased the growth of HUVECs and was fully covered by HUVECs at 72 h (Fig. 3-12B). These results proved that the synergic effect of the AHV coating could enhance EC growth. Additionally, with the introduction of arginine, the influence of the NO donors was weakened with the decreased differences between each group, which indicated the reduced dependence of stent coating on NO donors.

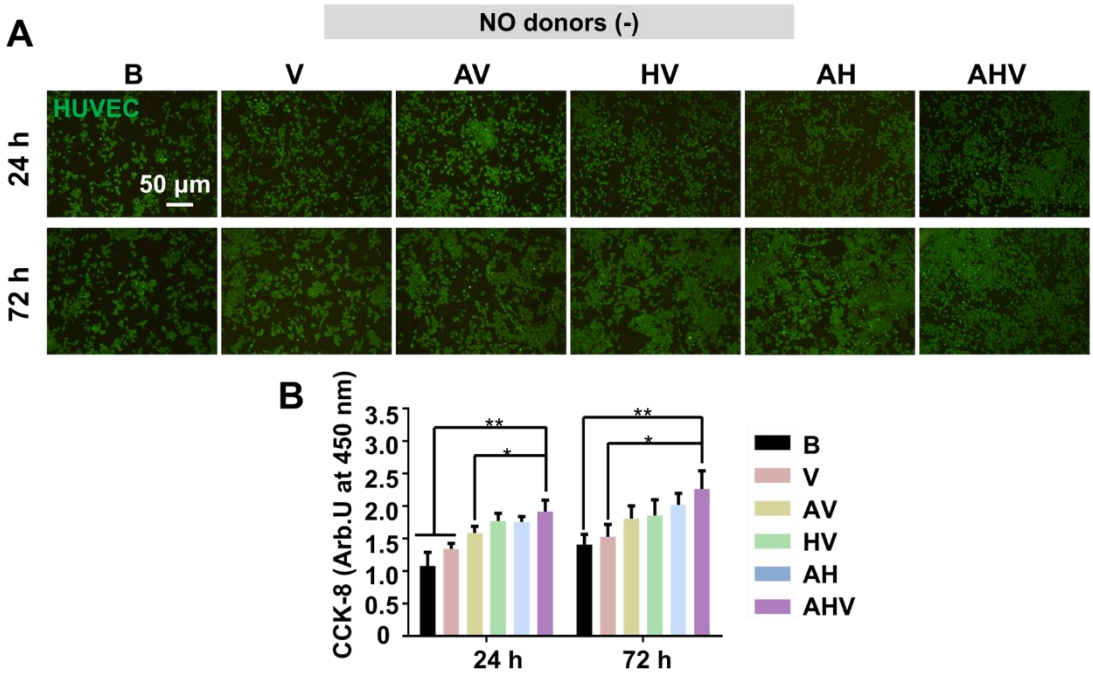

Fig. 3-11. (A) Fluorescence images of HUVECs without NO donor. (B) Proliferation of HUVECs without NO donors determined using CCK-8 assay.

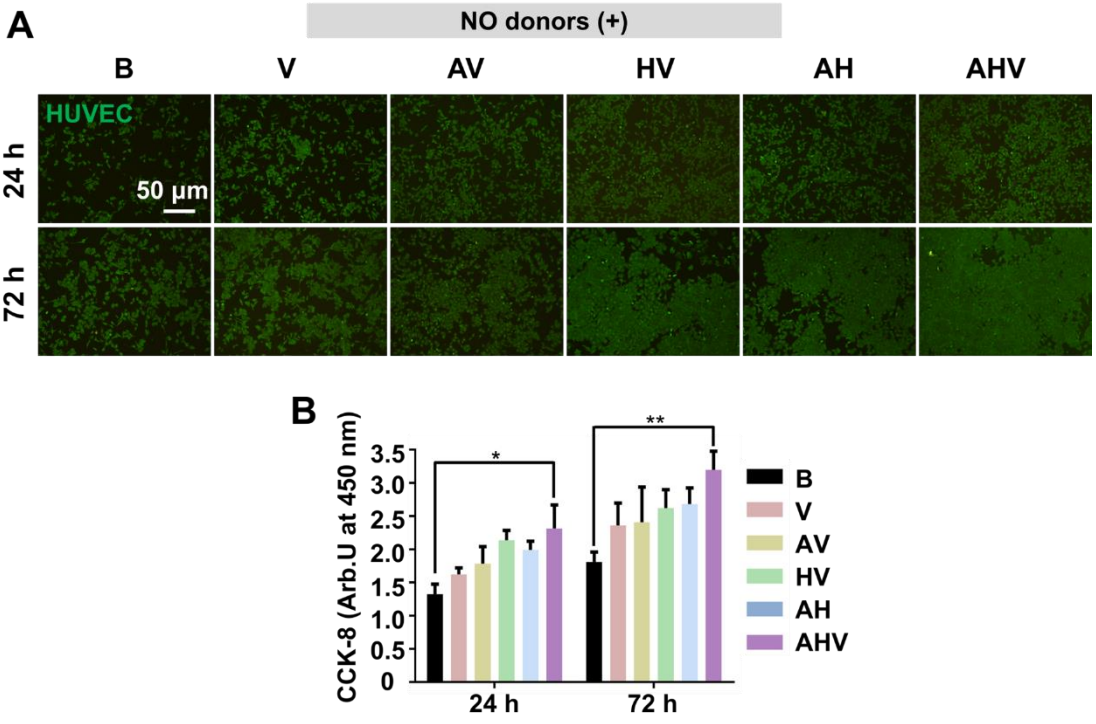

Fig. 3-12. (A) Fluorescence images of HUVECs with NO donor. (B) Proliferation of HUVECs with NO donors determined using CCK-8 assay.

As an important protein that enhances EC proliferation and decomposes arginine into NO, eNOS level was evaluated.[66, 88] In Fig. 3-13A, without NO donors, the increased eNOS expression could be found in the heparin-containing groups (9.20 ± 0.43 U/L in HV, 8.94 ± 0.81 U/L in AH and 11.57 ± 1.56 U/L in AHV), while the eNOS expression in bare, V and AV surface were only 3.87 ± 0.35 U/L, 4.51 ± 0.75 U/L and 6.60 ± 0.69 U/L, respectively. After adding NO donors, all the coated groups showed an escalated trend in eNOS levels; AHV had the highest eNOS amount (18.71 ± 1.10 U/L), while AV only showed 10.96 ± 1.55 U/L eNOS. These results proved that heparin had excellent ability to upregulate eNOS, which would facilitate arginine decomposition into NO. AV had a higher eNOS level than V regardless the presence of NO donors, possibly because arginine could enhance eNOS expression.[137, 138]

We then investigated NO production from each sample. As shown in Fig. 3-13B, only the groups with arginine had NO generation in the absence of NO donors, and the amount of NO generated was boosted after adding NO donors, especially in the AHV group, which was 8.06 and 1.25-fold higher than the bare and other coated groups. Consequently, owing to the increased EC adhesion, enhanced eNOS level and NO production, AHV showed the optimal effect on HUVEC growth, which was beneficial for reendothelialization.

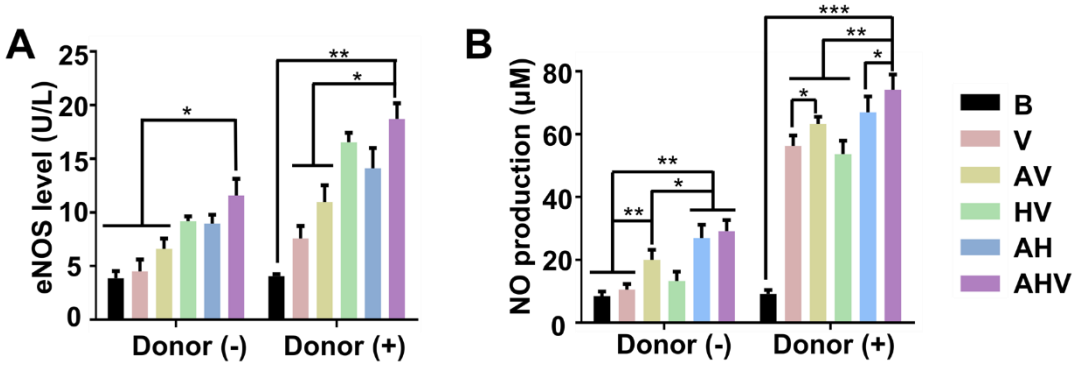

Fig. 3-13. (A) eNOS level in HUVECs after 72 h of culture. (B) NO production in HUVECs after incubated for 72 h.

3.3.3.3 Inhibition of platelet adhesion

After stent implantation, a significant risk of thrombotic occlusion arises from the

activated platelets' quick adherence and aggregation at the insertion site, so the inhibition of platelets is a basic requirement for CVSs.[88] In Fig. 3-14A, the bare sample showed no inhibition of adherent platelets. In contrast, the coated group showed significant suppression of platelet adhesion, where the AHV coating only had few platelets. The significant platelet-inhibiting effect was attributed to the long-term NO production and anticoagulant heparin. To investigate the related mechanism, the cGMP level in platelets was tested, which is associated with antiplatelet activity (Fig. 3-14B). The bare surface only possessed limited cGMP level (8.15 ± 1.48nM), while the AHV coating elevated cGMP synthesis (27.53 ± 3.07nM), which corresponded to the reduced platelets on its surface. These results implicated the superior endothelium-like anti-thrombogenic effect of the AHV coating.

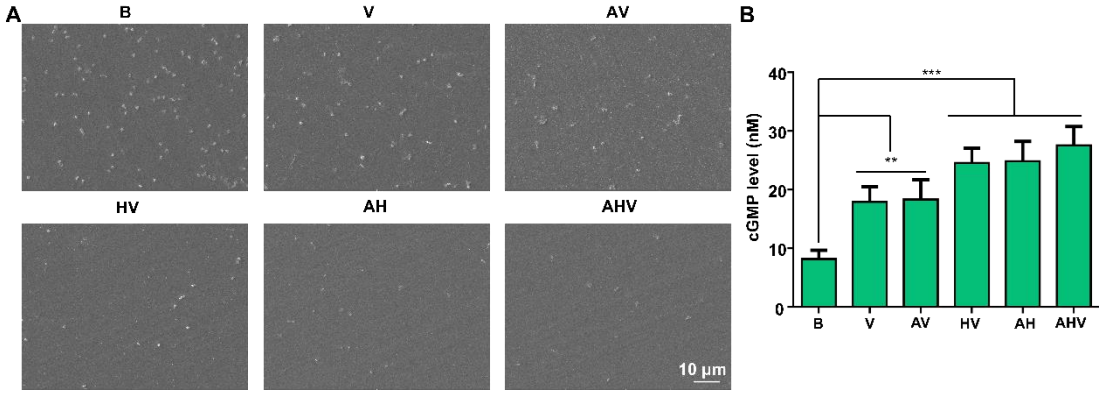

Fig. 3-14. (A) SEM images of platelet adhesion. AHV surface had no platelet adhesion. (B) Concentration of cGMP.

3.3.3.4 Co-adhesion of HUVEC and platelet

The addition of VEGF into stent surface improved the adhesion of ECs, although the difference between the coated groups was not obvious, which could be attributed to the positive effects of both arginine and heparin on EC adhesion. However, in the context of vascular injury, platelet adsorption and aggregation are common occurrences. It is crucial to achieve preferential adhesion of ECs while inhibiting platelets as the rapid formation of an endothelial layer prevents thrombus. Therefore, we examined the co-adhesion between ECs and platelets on each coating sample.

The HUVECs and platelets were pre-labeled by green and red fluorescence, respectively. In Fig. 3-15A, significant platelet and limited EC adhesion were found in

bare group. After surface modification, the EC amount had a rising trend, yet the anti-platelet effect varied among groups. Specifically, although V and AV group increased EC adhesion, they still exhibited obvious platelet adhesion, which could be attributed to the cationic nature of coated surfaces. The heparin-containing groups (HV and AH) demonstrated lower platelet adhesion due to the strong anticoagulant effect of heparin. Among all groups, AHV had the highest EC attachment with the lowest platelet adhesion, suggesting that the AHV coating had the potential to quickly form an endothelium on the stent and effectively suppress thrombosis.

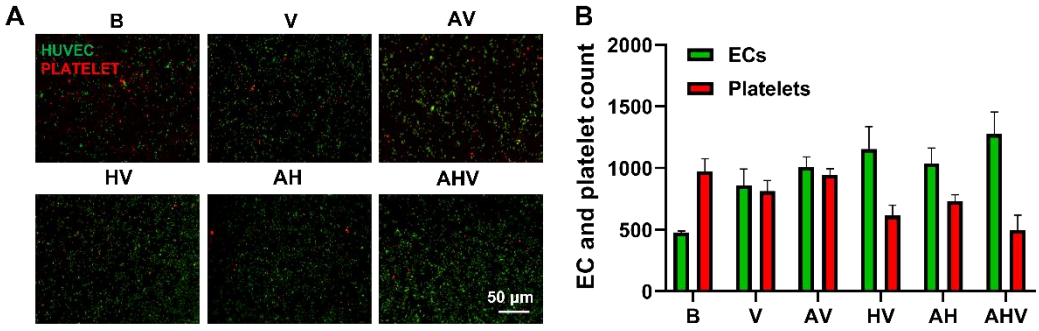

Fig. 3-15. (A) Images of competitive adhesion between HUVECs (green) and platelets (red) for 2 h. (B) EC and platelet count. Selective EC adhesion could be found in AHV coating.

3.3.3.5 Inhibition of HUASMC growth

As the over-growth of SMCs induces neointimal hyperplasia, we further investigated the SMC inhibitory effect of AHV coating. In Fig. 3-16, in the presence of NO donors, all the coated samples showed a huge suppression of HUASMC attachment compared to bare surface. The mechanism of SMC inhibition is attributed to the increased expression of cGMP by NO and heparin.[106-108] In Fig. 3-17, AHV coating significantly promoted the level of cGMP, which was 26.21 ± 2.14nM, increasing 3.9-fold compared with bare sample (6.67 ± 1.51nM). Overall, the AHV coating showed the strongest inhibitory effect on SMCs and was expected to have great potential to suppress restenosis.

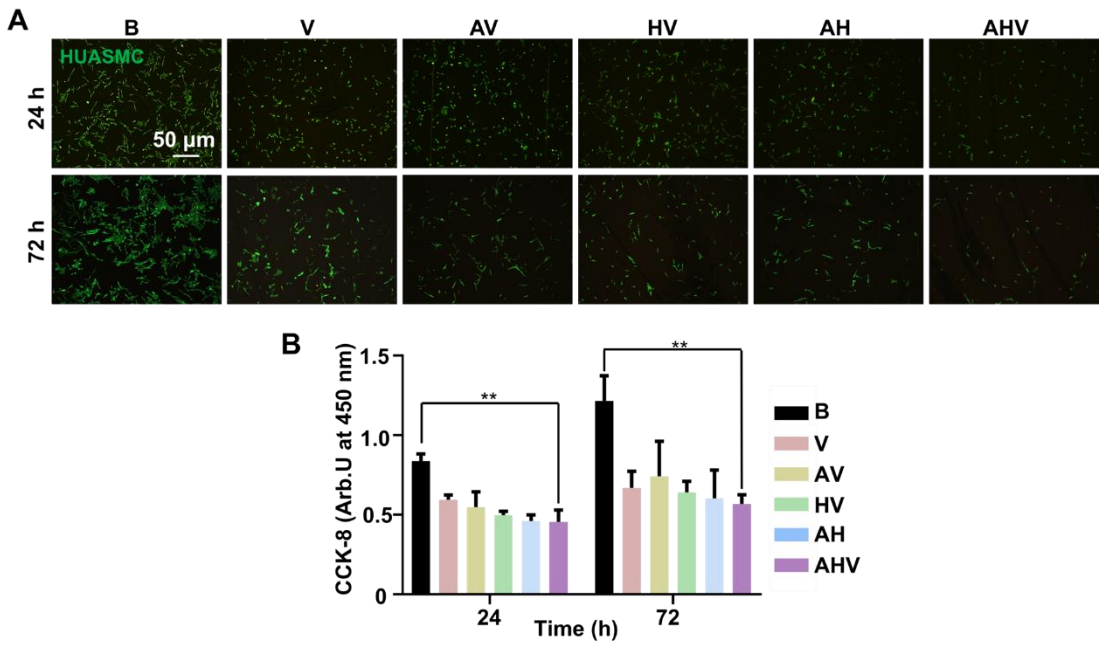

Fig. 3-16. (A) Fluorescence images of HUASMCs without NO donor. (B) Proliferation of HUASMCs without NO donors determined using CCK-8 assay.

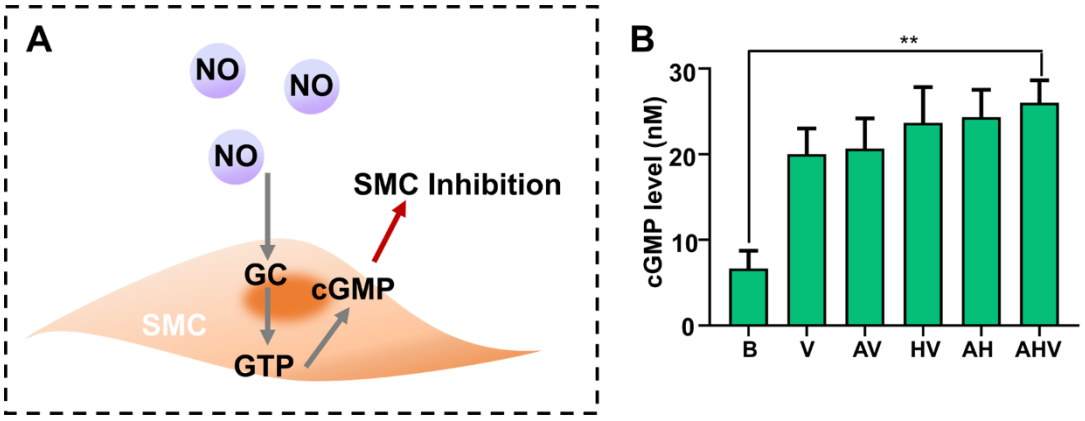

Fig. 3-17. (A) Illustration of SMC inhibition by NO (B) Concentration of cGMP in HUASMC after 72 h of culture.

3.3.3.6 Support of HUVEC migration while inhibiting HUASMC migration

Promoting EC migration is crucial for *in situ* reendothelialization after stenting. However, SMC over migration is detrimental, often leading to post-implantation hyperplasia and in-stent restenosis.[89, 109] Here, the cell migration on different coatings with NO donors was evaluated. As shown in Fig. 3-18, the bare group had limited migration of ECs (~26.7 μm). In contrast, the AHV group showed observably

enhanced cell migration at 116.4 μm, which was approximately 22 μm more than the HV and AH groups, and almost 5 times higher than that of the bare samples.

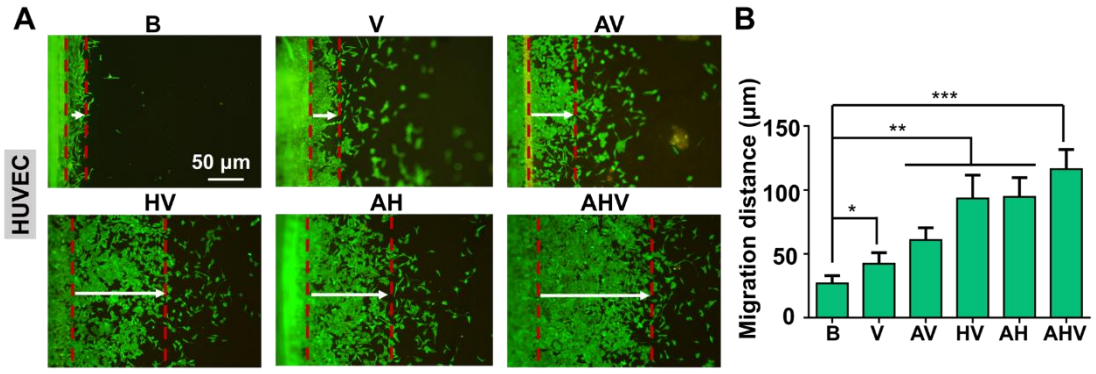

Fig. 3-18. (A) Actin fluorescence staining of HUVECs. (B) Migration distance of HUVECs.

In Fig. 3-19, the bare surface displayed little inhibitory effect on HUASMC migration (75.5 μm), while all the coated groups demonstrated enhanced suppression of HUASMC migration. Notably, the AHV group displayed the most significant reduction in migration distance (12.8 μm). These results suggested that our proposed AHV coating could promote EC migration while inhibiting SMC migration, which had great potential to facilitate endothelialization and suppress hyperplasia.

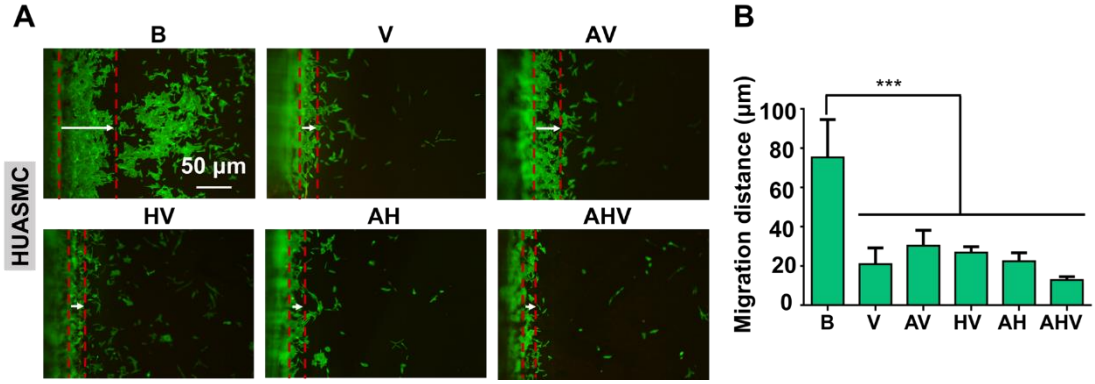

Fig. 3-19. (A) Actin fluorescence staining of HUASMCs. (B) Migration distance of HUASMCs.

3.3.3.7 Enhanced growth of EC over SMC

In Fig. 3-20, the HUVECs/HUASMCs ratio on AHV coating was 2.51 (24 h) and 2.94 (72 h), while the ratio on bare surface was 0.68 (24 h) and 0.43 (72 h), indicating a

higher number of HUVECs grown on the AHV coating while bare surface had more HUASMCs. Meanwhile, compared with bare surface which possessed more red fluorescence (HUASMCs), the AHV coated surface was fully covered by ECs, suggesting the superiority of the AHV for new endothelium formation and anti-intimal hyperplasia. According to the results, we could conclude that the biomimetic AHV coating boasts properties that favor ECs.

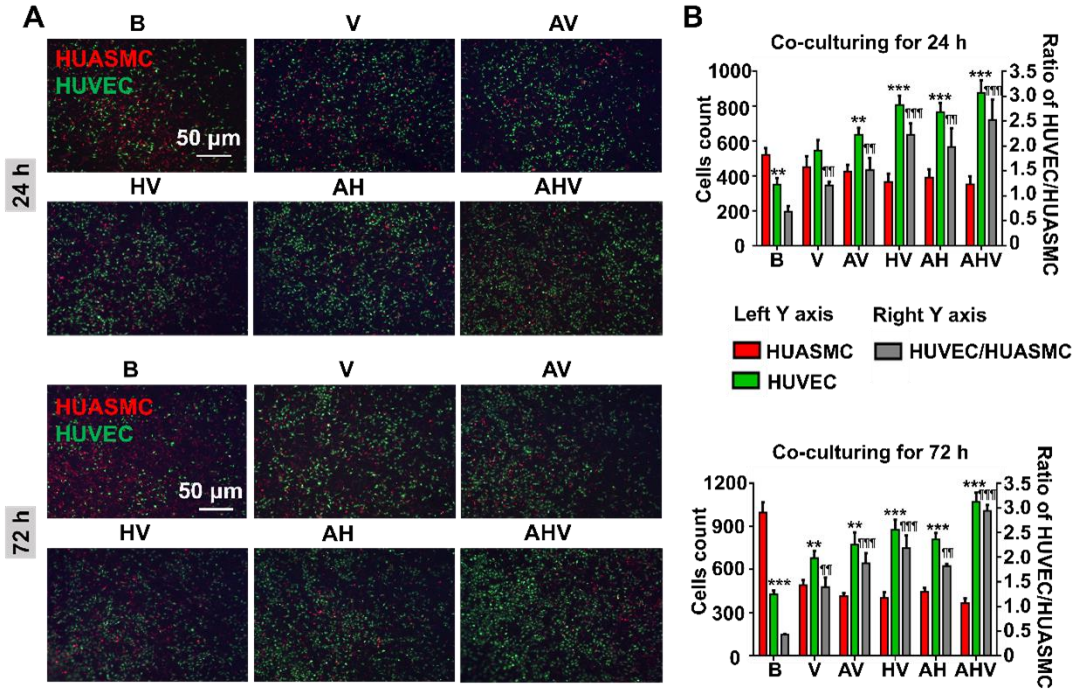

Fig. 3-20. (A) Images of competitive adhesion of EC (green) over SMC (red). (B) The ratio of EC/SMC on the different coatings. *, **, ***(EC vs SMC) and ¶, ¶¶, ¶¶¶ (vs 316 L SS) remarked $p < 0.05$, 0.01 and 0.001.

3.3.4 The AHV coating's anti-thrombogenic properties

To further demonstrate the antithrombotic and antiplatelet functions of the AHV coating, an AV-shunt experiment was performed, where each sample were installed into the PCV tubes withstanding blood circulation (Fig. 3-22). After 2 h, the photographs of stented lumen showed that the cross-section of a bare sample was completely blocked by blood clots (Fig. 3-23). On the contrary, the coated samples showed reduced blood clots, where the AHV group had almost no thrombosis on its wall. After observation by SEM, significant platelets were found on the bare sample, while the AHV coating possessed minimal platelet adhesion (Fig. 3-24).

Fig. 3-22. Image showing the *ex vivo* circulation setup, where sample-loaded PVC tubes were connected to the left and right vessel of the rabbits and kept blood circling for 2 h.

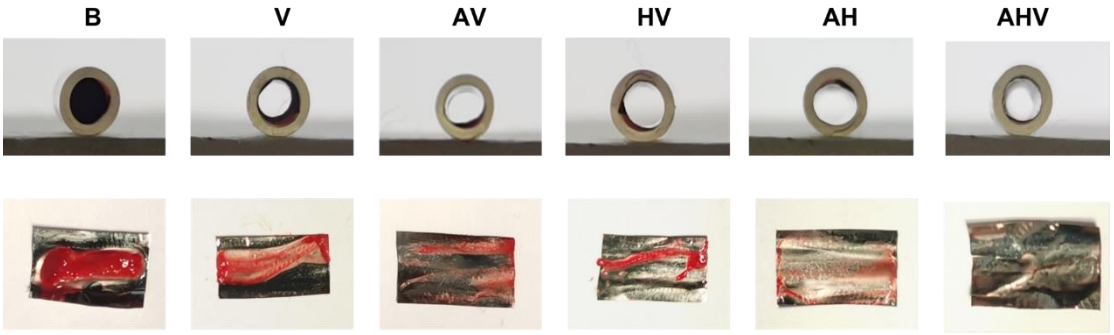

Fig. 3-23. Representative photographs of cross-sections of foil tubes coated with different coatings showing the thrombus. The AHV group had almost no blood clots onto its wall.

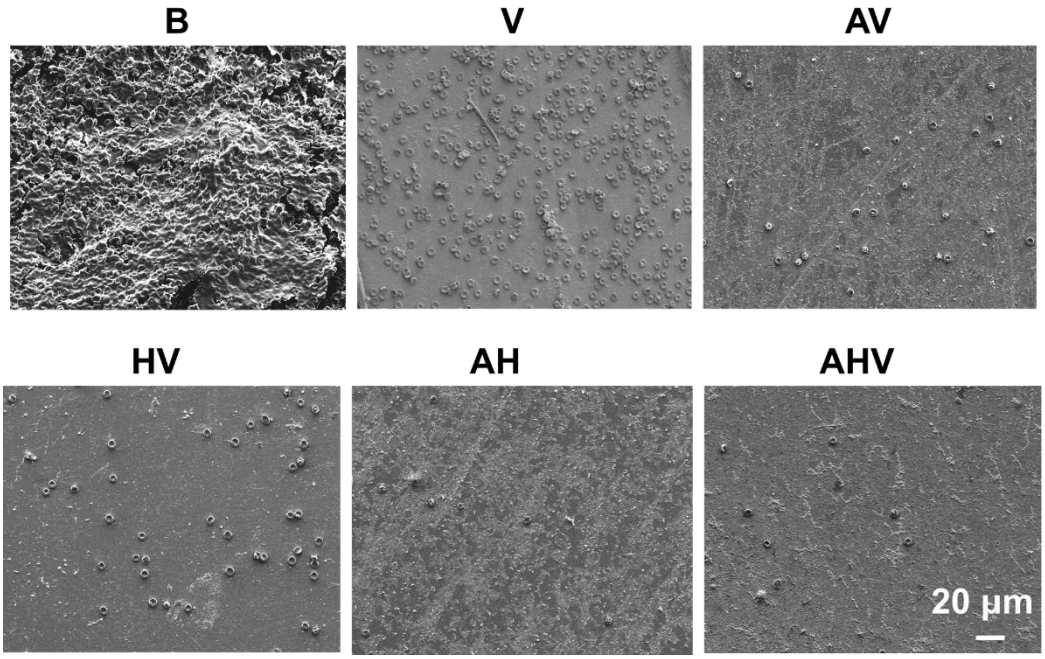

Fig. 3-24. Representative SEM images of platelet adhesion. The AHV coating had the least platelet adhesion.

Furthermore, the quantitative data showed that the weight of thrombus in each coated group was lower (V: 8.83 mg, AV: 9.23 mg, HV: 9.30 mg, AH: 4.85 mg and AHV: 3.90 mg) than that in the bare surface (~30.8 mg). Fig. 3-22 further reveals that the bare samples were fully blocked with a high occlusion rate (95.01%), whereas the AHV coating dramatically reduced the percentage of occlusion to 6.69%. The V and AV groups possessed more thrombus and higher occlusion rates among all the coated samples possibly because of increased surface adhesion by positively charged components (such as DA/HD and arginine). For HV, AH and AHV groups, the incorporation of heparin may shield the surface cations and improve blood compatibility. The reduced thrombus and occlusion benefit the blood flow as the blocked bare samples only allowed 29.16% blood flow, while the AHV had 81.06% blood flow. Overall, as evidenced by almost no occlusive thrombosis, we could conclude that the AHV coating possessed improved anti-thrombogenicity.

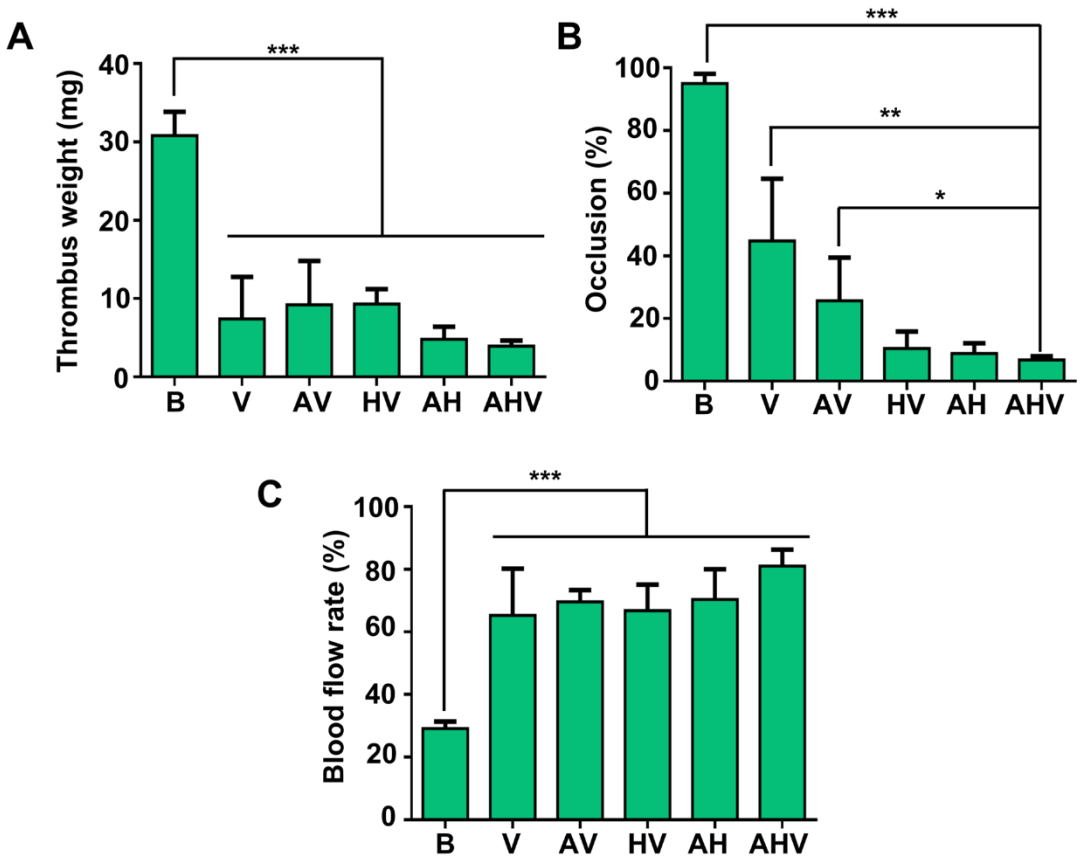

Fig. 3-25. (A) Occlusion percent and (B) the weight of blood clot. (C) The rate of blood flow in different samples.

3.3.5 Long-term anti-restenosis efficacy

To learn more about how AHV-coated stents affected reendothelialization and anti-restenosis, stenting was performed in a rabbit model (Fig. 3-26). To assess the rapid reendothelialization, SEM observation and CD31 (vascular endothelial marker) immunofluorescence staining after a 1-week implantation were carried out. In Fig. 3-27, thromboid erythrocyte deposition was observed on the commercial Primtech™ stent, whereas endothelium-like cell growth was observed on the AHV-coated stents. Subsequently, fluorescence images verified the endothelium coverage. Fig. 3-28 showed that the Primtech™ stent had limited ECs, while a compact CD31 signal was found on the AHV stents, demonstrating the AHV coating promoted the formation of an EC layer.

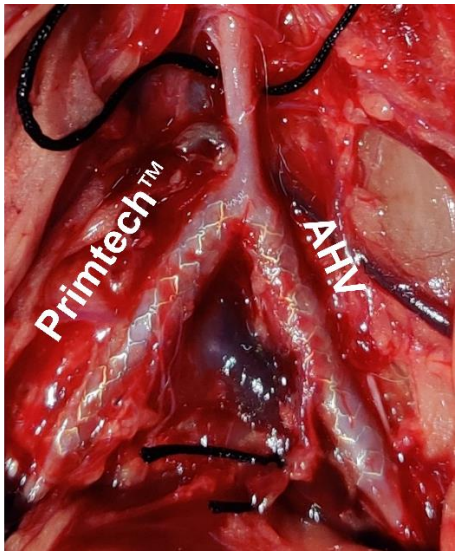

Fig. 3-26. Image of stent implantation in rabbit, where the Commercially used bare 316L SS stents and the AHV stents were implanted onto the iliofemoral arteries.

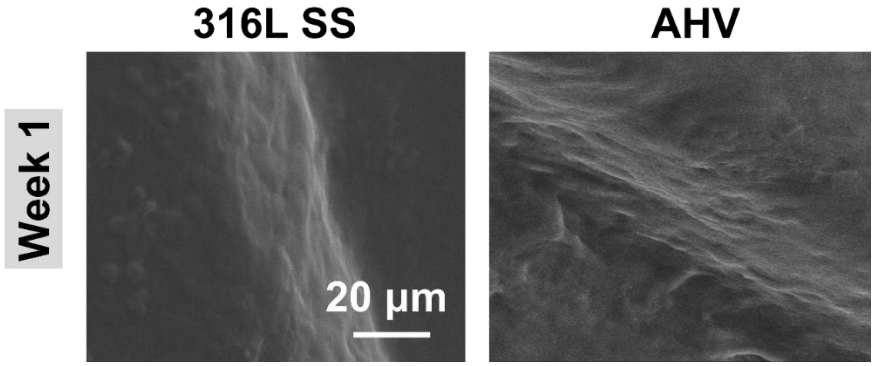

Fig. 3-27. SEM pictures after a week of stent implantation.

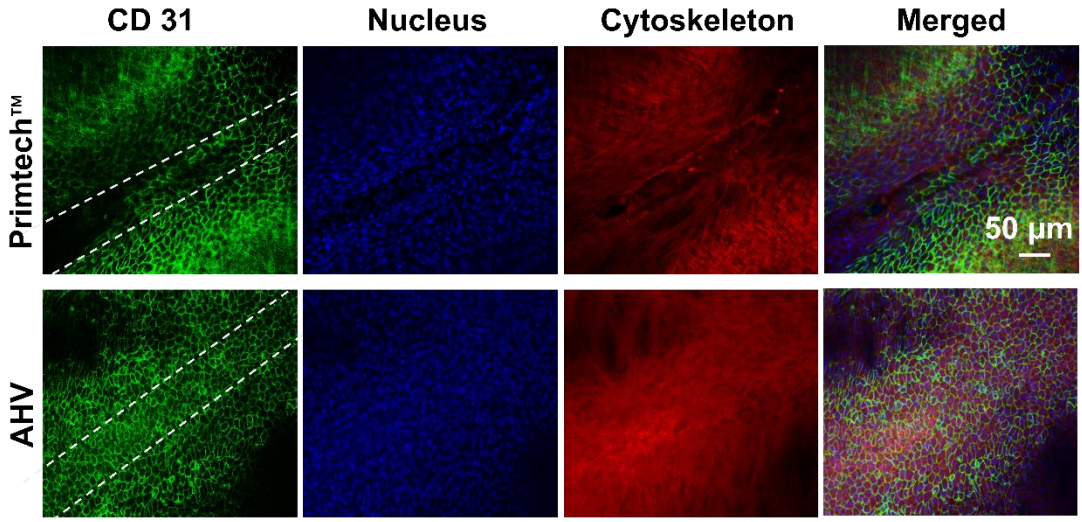

Fig. 3-28. CD31 immuno-fluorescence (green), phalloidin (red) and DAPI (blue) staining showing reendothelialization of stents at1 week.

At 4 and 12 weeks, obvious intimal hyperplasia happened in Primtech™ stent, whereas the AHV coated stents greatly decreased the hyperplasia (Fig. 3-29). Specifically, the AHV-coated stents had a significant decline in mean neointimal area (Fig. 3-30A) (0.58 mm^2 in 4 weeks and 0.52 mm^2 in 12 weeks) compared with the bare stents (1.12 mm^2 in 4 weeks and 1.99 mm^2 in 12 weeks). Accordingly, Fig. 3-30B shows the Primtech™ stents had a high neointimal stenosis ratio at 4 (18.38%) and 12 weeks (28.87%), while a significant attenuation of neointimal stenosis could be found in the AHV stents (9.45% in week 4 and 10.27% in week 12). Taken together, the AHV stents provided a friendly environment that supports fast reendothelialization, attenuates restenosis and maintains the durability of CVSs over time.

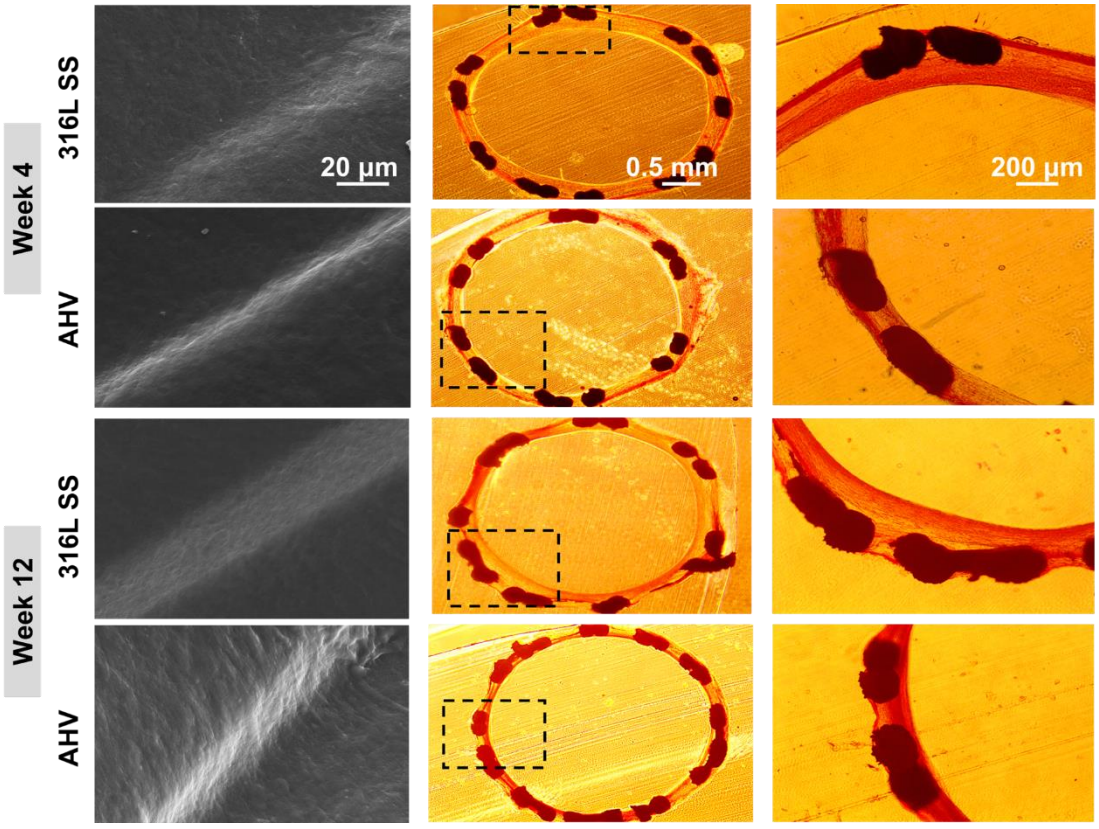

Fig. 3-29. Representative SEM images and staining analysis on restenosis of different CVSs.

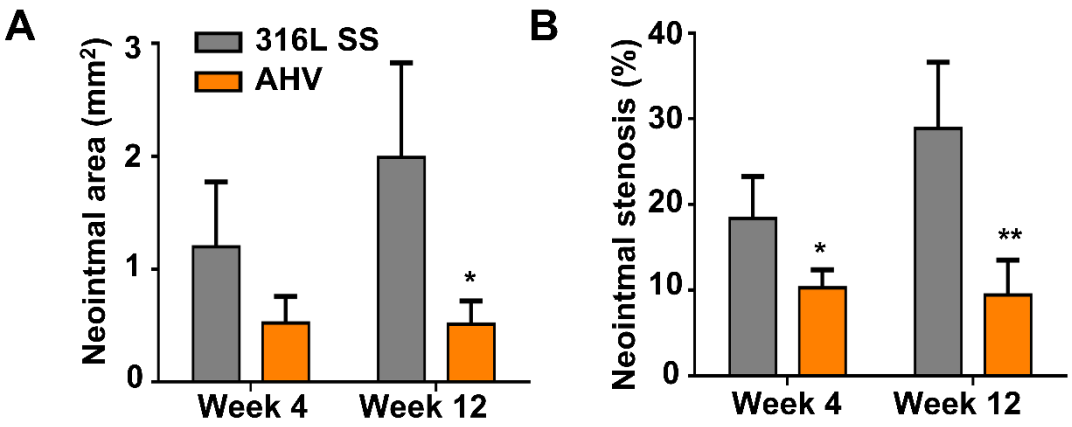

Fig. 3-30. (A) Intimal area and (B) implanted stent stenosis analysis.

3.4 Summary

Surgical interventions with CVSs are widely performed procedures nowadays for CVD treatment, but thrombosis and restenosis limit the therapeutic efficiency of CVSs. After endothelial damage during stenting, a series of cellular events occur, and an ideal stent should adapt to the physiological responses. This project developed a biomimetic stent coating (AHV) that presented therapeutic biomacromolecule VEGF and therapeutic gas NO. At the early stage of stenting, the VEGF rapidly promoted EC adhesion, thereby facilitating reendothelialization. Meanwhile, the sufficient NO production from Cu catalysis and heparin-assisted arginine decomposition sustainably inhibited platelets and SMCs, which in turn suppressed thrombosis and restenosis, respectively. Further animal experiments verified all the above results. Consequently, the AHV coating had a good potential to improve the long-term effectiveness of CVSs. Because of the catechol structure of dopamine, our proposed stent coatings have a strong mussel-mimicking adhesive effect on the surfaces of many materials. For materials with special properties, such as superelastic nitinol and degradable magnesium, our coating must be modified accordingly, so the functions of the coating warrant further investigation.

Chapter 4 Development of a NO donor-free cell-instructive bone scaffold that capturing bone and vascular cells to promote bone repairing.

4.1 Introduction

Bone defects arising from trauma, osteoarthritis, or bone tumors pose significant challenges in modern medicine. The global demand for bone grafts or substitutes has reportedly reached US$3.4 billion by 2022, placing a substantial financial burden on the healthcare system.[139] Although bone tissue possesses inherent regenerative capabilities, self-repair becomes arduous with bone defects due to complications such as chronic infection, malignant tumor invasion, and immune disorders.[140-142] Moreover, when the bone defect exceeds a critical threshold, the natural healing process fails to achieve complete bone restoration, necessitating medical intervention. Autologous or allogeneic bone grafting is a common clinical approach but the limited availability of suitable donors, delayed bone formation, and the risk of autoimmune rejection impose constraints on its utility.[143-145] Consequently, researchers have endeavored to develop various artificial bone grafts, including metal, ceramic, and synthetic bone scaffolds to facilitate bone regeneration.[146-148] Unfortunately, these conventional scaffolds primarily offer mechanical support, often neglecting the intricate physiological processes involved in bone repair.

Bone regeneration encompasses a series of interconnected processes, with continuous angiogenesis and osteogenesis playing essential roles throughout.[149] This intricate and protracted journey involves various cell types (such as vascular and bone cells), cytokines or growth factors (for example: BMP and VEGF), and other signaling molecules like NO, which collectively orchestrate the precise repair of bone defects.[150-153] Consequently, researchers have explored the integration of bioactive chemicals within bone scaffolds, such as using scaffolds to load drugs, cytokines, or developing cell-laden scaffolds to modulate the bone repair processes. Although these strategies address the challenge of slow osteogenesis, their potential pitfalls cannot be ignored. For example, drug-loaded scaffolds may encounter issues such as drug toxicity and leakage, whereas scaffolds loaded with cells and cytokines may pose

biocompatibility concerns and require careful maintenance of cell viability or bioactivity. These adverse effects hinder the safety, efficacy, and translation of bone scaffolds to clinical applications.[154, 155] Therefore, an ideal strategy that can spontaneously recruit autologous cells and generate therapeutic molecules without relying on exogenous drug regulation holds tremendous potential for reshaping the favorable bone microenvironment and expediting bone regeneration.

Cell-instructive and cell-adhesive strategies can apply peptides to interact with the integrin receptors on cell membranes, enabling the adherence of cells from the surrounding microenvironment. However, bone repair involves the coordinated actions of both osteogenic and angiogenic cells, and this non-selective and non-specific cell adhesion will lead to inefficient cell recruitment. Therefore, an ideal cell-instructive bone scaffold should selectively capture bone and vascular cells, thus coordinating osteogenesis and angiogenesis for more effective bone regeneration. Recent studies have reported a 12-amino acid polypeptide called TPSLEQRTVYAK (TPS) for its ability to specifically adhere to endothelial progenitor cell (EPC), a stem cell with the high tendency to differentiate into mature EC and facilitate angiogenesis.[156-159] Meanwhile, n-cadherin (N-CAD) is a transmembrane protein, which is thought to be a key factor in directing intercellular interactions during mesenchymal cohesion. The enhanced cell-cell interaction by N-CAD can adhere bone mesenchymal stem cells (BMSCs) and regulate osteoblast genes, thus promoting osteogenic differentiation.[160-163] Therefore, assembling TPS and N-CAD onto bone scaffolds can promote BMSC homing to the defect site, promote osteoblast differentiation and bone formation, while mediating EPC adhesion, migration and angiogenesis, leading to effective new bone formation and vascularization.

To maximize peptide modification for cell recruitment, scaffolds with large surface areas are required. Triply periodic minimal surface (TPMS) scaffold has porous and hyperboloidal structure that closely mimics natural bone architecture. Its refined connectivity, porosity, and curvature endow exceptionally large surface area and the ability to support substance exchange.[164, 165] From a macro perspective, TPMS scaffold mimics the hyperbolic geometry of trabecular bone, and such bionic topological structure can facilitate osseointegration. Microscopically, TPMS scaffold has a different Gaussian curvature at each surface point (positive curvature on the convex side and negative curvature on the concave side), and this curvature change

enables cells to undergo cytoskeletal reorganization in response to topographical stimuli, thereby regulating cell adhesion, proliferation and differentiation In our previous study, to investigate the effect of TPMS topological features on cells, we prepared scaffolds without Gaussian curvature as well as scaffolds with curvatures of -2, -4, and -6 mm^{-2} (namely G0, G2, G4, and G6), and then observed cell morphology on each scaffold. [165] The results showed that compared with G0, obvious cytoskeletal reorganization was observed on the hyperboloid surface of the G2, G4, and G6 groups. Furthermore, on curvature surfaces, this topographic stimulation deforms the nucleus through interactions between stress fibers and the nuclear membrane, thus regulating cell fate. This regulation increased with increasing curvature, with the highest cell aspect ratio and number of focal adhesion near nuclei in G6, favoring the regulation of osteogenic/angiogenic differentiation of cells. Thus, the combination of TPMS scaffolds with peptides not only mimics natural bone properties and provides mechanical support, but also enhances the grafting rate of peptides and cell recruitment. All the phenomena above combined would closely simulate and promote the bone repair process.

In this project, we attached the peptides onto the surface of TPMS scaffold by a simple two-step method through bioorthogonal click chemistry without any organic reagents or metal catalysis (Fig. 4-1). TPMS scaffolds were prepared using β-tricalcium phosphate (β-TCP, a body inherent substance) by stereolithography-based 3D printing. The bare scaffold was sequentially dipped into a polydopamine-azide (PDA-N_3) solution, then placed it into an alkyne-containing TPS-dibenzocyclooctyl (DBCO) and N-CAD-DBCO solution, where the N_3 and DBCO underwent a rapid bioorthogonal click reaction to obtain the TPMS-TPS/N-CAD scaffold.[166]

The co-adhesion of EPCs and BMSCs on the scaffold surface led to a paracrine effect, where the EPCs secreted BMP-2 to promote osteogenesis in BMSCs, while the BMSCs produced VEGF to support angiogenesis. Such intercellular contact aided both cells' development and differentiation. [167-169] Meanwhile, the aggregation of cells on the scaffold surface triggered the spontaneous production of NO, which served a regulatory role in osteogenesis-angiogenesis by stimulating the NO-cGMP pathway.

Compared with conventional bone scaffolds that require exogenous cells, growth factors or drugs, our proposed TPMS-TPS/N-CAD scaffold can achieve *in situ* recruitment of autologous cells, avoiding exogenous regulation and thus possessing a

higher biocompatibility with lower immunogenicity and cytotoxicity. In addition, this scaffold is easy to prepare, and the scaffold design mimics natural bone microenvironment, coordinating the coupling effect of osteogenesis and angiogenesis during bone repair, which has great potential for clinical applications.

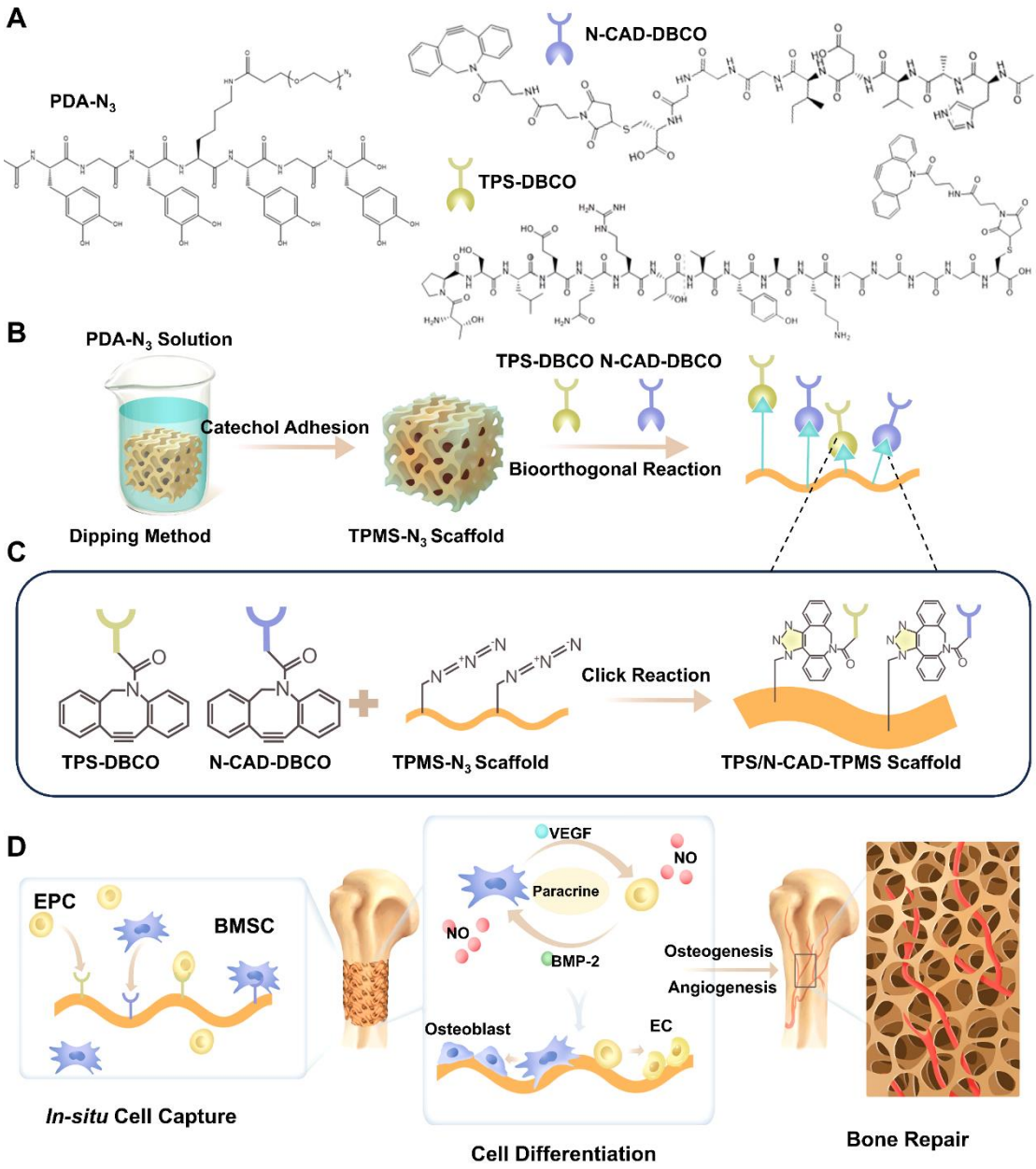

Fig. 4-1. (A) Chemical structure of PDA-N_3, N-CAD-DBCO and TPS-DBCO. (B) The TPS/N-CAD TPMS scaffold was prepared by an organic-free dipping method, where the TPMS scaffold was first dipped in PDA-N_3 solution, and then placed in a peptide mixture solution. (C) The TPS and N-CAD peptides were attached onto stent surface by click reaction between the alkynyl group and N_3 with high efficiency. (D) After *in vivo* implantation, the TPS/N-CAD TPMS scaffold could capture EPC and BMSC, and

the adherent cells would undergo paracrine effect to release therapeutic molecules NO, VEGF and BMP-2 to promote osteogenesis and angiogenesis, ultimately accelerating bone repair.

4.2 Materials and Methods

4.2.1 Fabrication and characterization of TPMS-TPS/N-CAD

A commercial slurry (50 wt.% β-TCP, 49 wt.% 1,6-hexanediol diacrylate-based resin and 1 wt.% camphorquinone) was used to prepare the TPMS scaffold by a stereolithography-based printer (Lithoz CeraFab 8500, Austria). After 3D printing, the cured scaffold was cleaned with acetone and then defatted in ambient air at 205°C for 16 h and sintered at 1200°C for 4 h to obtain the TPMS scaffold. The TPMS scaffolds had zero mean curvature and non-positive Gaussian curvature, with G0 (zero Gaussian curvature) as the control, while G6 (-6/mm^2 Gaussian curvature) represented the sample group.

An organic-free dipping method was performed to functionalize the TPMS scaffold surfaces. Briefly, the bare TPMS scaffolds were immersed into a 0.01 mg/mL PDA-N_3 solution to prepare a PDA-N_3 coating. Afterward, the coated TPMS scaffolds were incubated with a TPS-DBCO/N-CAD-DBCO solution to form the TPMS-TPS/N-CAD scaffold. To determine the suitable ratio of these two peptides, different molar ratios of TPS and N-CAD were used (0:4, 1:3, 2:2, 3:1, and 4:0, with a total concentration of 0.1 mM).[104]

To verify that the scaffold with curvature could load more peptide, fluorescently labeled peptides were modified onto the surfaces of G0 and G6 scaffolds with the protocols described above. The load efficiency was calculated by measuring the fluorescence intensity before and after modification by a microplate reader. Moreover, the surface fluorescence distribution was observed by a confocal laser scanning microscope (CLSM, Zeiss, Germany). To observe the peptide modification, FITC-labelled TPS-DBCO peptide and Cyanine 5 (Cy5)-labeled N-CAD peptides were used at ratios of 0:4, 1:3, 2:2, 3:1, and 4:0. The fluorescence distribution was observed by CLSM, while the fluorescent intensity was analyzed by ImageJ software.

4.2.2 Evaluation of *in vitro* biological properties of TPMS-TPS/N-CAD

4.2.2.1 *In vitro* EPC and BMSC capture and cell growth

A self-made cell circulation system was used to capture EPC and BMSC (Fig. 4-3). The

cell capture experiments received helps from Mr. Shuai ZHAO. Briefly, the cells were pre-labeled by cell tracker red, and the bare and coated TCP plates (PDA group and TPS:N-CAD = 0:4, 1:3, 2:2, 3:1, 4:0 groups) were placed into a chamber, and then the EPC or BMSC suspension (2×10^5 cells/mL) was driven by a peristaltic pump to flow into the chamber for 2 h Afterward, all samples were washed and observed by a fluorescence microscope. For adherent cell quantification, CCK-8 was carried out. To evaluate cell viability, after 2 h of reflux, all samples were placed into a cell incubator. After 24 and 72 h, live/dead staining was carried out, while cell growth was quantified by Picogreen DNA assay. For cell co-capture, EPCs were pre-labeled by cell tracker green, and BMSCs were stained by cell tracker red. After 2 h of reflux and 1 day of culture, the scaffolds were fixed and observed by a fluorescent microscope.[170, 171]

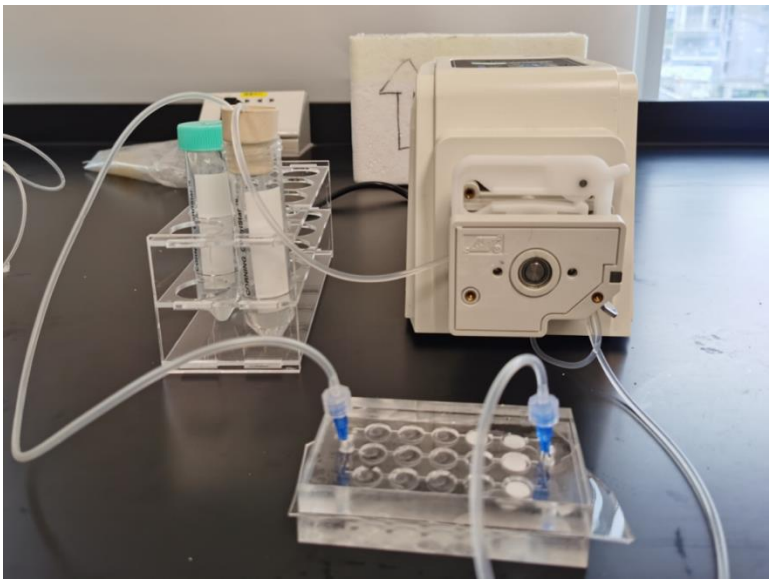

Fig. 4-3. Cell circulation equipment for cell capture.

4.2.2.2 *In vitro* osteogenic evaluation

The *in vitro* experiments received helps from Miss Yongyi MO. 5×10^4 cells/cm^2 BMSCs were seeded onto each scaffold, and non-adherent cells were washed with PBS after being cultured for 2 h. For alkaline phosphatase (ALP) staining, after 7 and 14 days, the samples were placed into BCIP/NBT working solution, and the ALP activity was determined by an ALP quantification kit at 405nm. For Alizarin Red S (ARS), after 14 and 28 days, the samples were immersed in ARS working solution and then placed in

10% alkyl pyridine chloride; the ARS levels were measured by a microplate reader at 592nm.[172, 173] Furthermore, the relative expressions of osteogenic genes (Table 1), including osteocalcin (OCN), BMP-2, ALP, and runt-related transcription factor 2 (Runx2), were tested by quantitative reverse transcription-polymerase chain reaction (qRT-PCR).[174]

Table 1. Osteogenic primers for qPCR

Target gene	Forward primer (5'-3')	Reverse primer (5'-3')
GAPDH	CTGAACGGGAAGCTCACTGGC	GAGACAACCTGGTCCTCAGTGTAGC
BMP-2	CCAGAAATGAGTGGGAAAACG	ATTAATTCGGTGCTGGAAACTACTA
Runx2	CCGATGGGACCGTGGTT	CAGCAGAGGCATTTCGTAGCT
ALP	CGGGGACATGCAGTATGAGTTGAA	AAGAAGCCTTTGGGATTCTTTGTCA
OCN	TGCATTCTGCCTCTCTGACC	ACCACCTTACTGCCCTCCTG

4.2.2.3 *In vitro* angiogenic evaluation

5×10^4 cells/cm^2 EPCs were seeded onto each scaffold, and non-adherent cells were washed with PBS after 2 h. The cells were continuously cultured for 3 days. CD31 immunostaining was performed following the manufacturer's instruction, and images were captured by a CLSM.[175, 176] Furthermore, the relative expressions of angiogenic genes (Table 2), including VEGF, CD31, angiogenin (ANG), and Von Willebrand factor (VWF), were tested by qRT-PCR.

Table 2. Angiogenic primers for qPCR

Target gene	Forward primer (5'-3')	Reverse primer (5'-3')
GAPDH	CTGAACGGGAAGCTCACTGGC	GAGACAACCTGGTCCTCAGTGTAGC
VWF	GCCTCTACCAGTGAGGTTTTGAAG	ATCTCATCTCTTCTCTGCTCCAGC
VEGF	TGCCCACCCACCAGAGTCAC	GAAGTTGGGAACGGAGGAAAGG
CD31	TCACCATCCAGAAGGAAGAGACG	GGCTAGTCTTGATCTCAGGACAATC
ANG	GCTGGCAGTACAATGACAGT	GTATCTGGGCCATCTCCGAC

4.2.2.4 *In vitro* paracrine between EPCs and BMSCs

4×10^4 cells/well of EPCs were seeded at the bottom of the transwell plate. Then, 4×10^4 BMSCs were seeded onto the TPMS scaffold, and the BMSC-seeded sample was placed in an upper chamber (Fig. 4-4A). The VEGF secretion from BMSC was measured by ELISA kit. For wound closure assay, a scratch was made in the middle of each EPC-seeded well with a scratcher; at 0 h and 24 h, EPCs were stained by Calcein AM. The cell migration distance was measured by ImageJ software. For tube formation assay, Matrigel was pre-spread on the bottom of each well to allow tube formation, and EPCs pre-labeled with cell-tracker green (4×10^4 cells/well) were seeded onto the Matrigel; the BMSC-seeded scaffold was placed in an upper chamber and co-cultured for 8 h. The tubular formation was observed under a fluorescence microscope, and total branch length and branch points were quantified by ImageJ.[177, 178]

To evaluate the paracrine effect of EPC on BMSC, 4×10^4 cells/well of BMSCs were seeded onto the TPMS scaffold at the bottom of the transwell plate. Then, 4×10^4 EPCs were seeded onto the surface of TPMS scaffolds, and the EPC-seeded sample was placed in an upper chamber (Fig. 4-4B). The BMP-2 secretion from EPCs was measured by ELISA kit. The OCN immunostaining was performed following the manufacturer's instruction, and images were captured by a CLSM. For calcium quantification, the calcium ions of BMSCs at the bottom were labeled by a fura-2 pentakis (acetoxymethyl) ester tracker and measured using a calcium colorimetric kit.[179]

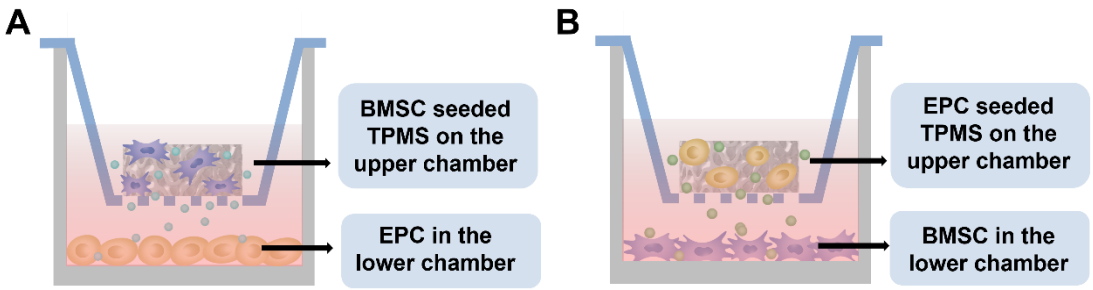

Fig. 4-4. (A) Paracrine effects of EPC on BMSC. (B) Paracrine effects of BMSC on EPC.

EPCs and BMSCs were co-cultured onto the TPMS scaffold. The NO production was measured and traced, and the NO-cGMP level was tested by an ELISA kit. The relative expressions of osteogenic (ALP and Runx-2) and angiogenic (CD31 and VWF) genes of the co-culture system were measured by qRT-PCR. Afterward, the results were standardized in a heat map to select an optimal co-grafting ratio of TPS and N-CAD to facilitate the follow-up experiments.[180, 181]

4.2.3 Evaluation of *in vivo* therapeutic efficiency of TPMS-TPS/N-CAD

The rabbit femoral defect model was used to assess *in vivo* bone healing with permission from the Ethics Committee of the Hong Kong Polytechnic University. The animal experiments were assisted by Miss Qing LIAO (from Prof. Huaiyu WANG's research group), Mr. Tianpeng XU, Mr. Shuai ZHAO, Miss Yongyi MO and Miss Xintong ZHOU. Adult male New Zealand white rabbits (3.5 - 4.0 kg) were divided into 3 groups: blank, bare-TPMS, and TPS/N-CAD-TPMS. The rabbits were anesthetized, and a 6-cm skin incision was made to expose the femoral condyle. Then, a round defect was made by a dental drill before the TPMS scaffolds (Ø5 mm × 8 mm) implantation. After 4 and 8 weeks, the rabbits were sacrificed with CO_2 suffocation, and the samples were harvested.

Bone regeneration was analyzed by a high-resolution micro-CT. To distinguish the new bone and the scaffold, different thresholding ranges (new bone = 80 ~140, scaffold = 140) were used, and 3D models were rebuilt by the NRecon software. Bone mineral density (BMD) and bone volume/total volume value (BV/TV) were calculated by CTAn software.

4.2.4 Statistical analysis

T-test and one-way ANOVA were used for statistical analysis. $p < 0.05$, 0.01, and 0.001 were denoted with *, **, and ***, respectively.

4.3 Results and discussions

4.3.1 Fabrication and characterization of TPMS-TPS/N-CAD scaffold

The TPMS-TPS/N-CAD scaffold was prepared by a simple and organic-free dipping method, where the TPS and N-CAD were attached to the TPMS by a rapid click-action between N_3 and alkynyl group. Subsequently, a comparison of grafting amount between G0-TPMS and G6-TPMS was carried out and a FITC-labeled peptide was used to visualize and quantify surface modification. As shown in Fig. 4-5A, both G0 and G6 scaffold had fluorescent signal, indicating successful peptide modification, with G6 showing strong green fluorescence even at deeper depth (~ 1200 μm). Due to larger surface area, the peptide grafting rate in G6 was higher than that in G0, indicating G6 had a larger potential for surface modification.

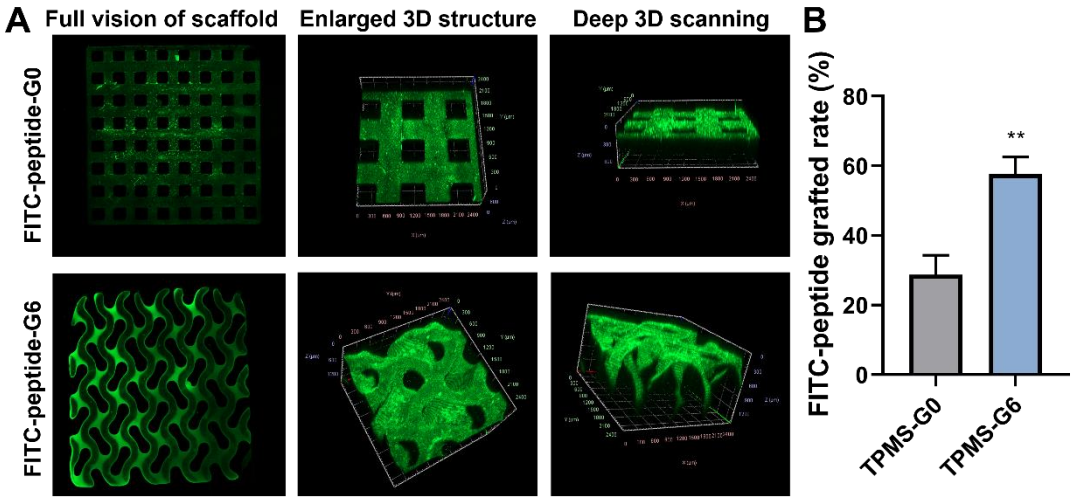

Fig. 4-5. (A) 2D and 3D images of fluorescent peptide modification onto G0 and G6 scaffold. (B) Quantification of peptide grating rate.

We then set five peptide grating ratios/groups (TPS:N-CAD = 0:4, 1:3, 2:2, 3:1 and 4:0) to find the optimal one. Two fluorescent dyes (FITC and Cy5) were used to label TPS and N-CAD, respectively. In Fig. 4-6A, the two-color fluorescence distribution displayed that green (TPS) and red (N-CAD) signals changed overall with varying ratios but were uniforms for a given ratio. In the fluorescence quantitative analysis (Fig. 4-6B), the fluorescence intensities of the two signals in each group were proportional, which was consistent with the grouping ratio we set. Afterward, to measure the surface hydrophilicity, WCA test was carried out. In Fig 4-9, the bare TCP surface was

hydrophobic with a high WCA (~61.01°); the figure dropped to around 30° in coated groups, indicating improved hydrophilicity, which was beneficial for cell growth. These results verified the successful modification of TPS and N-CAD onto G6 scaffold, providing a good potential for cell capture.

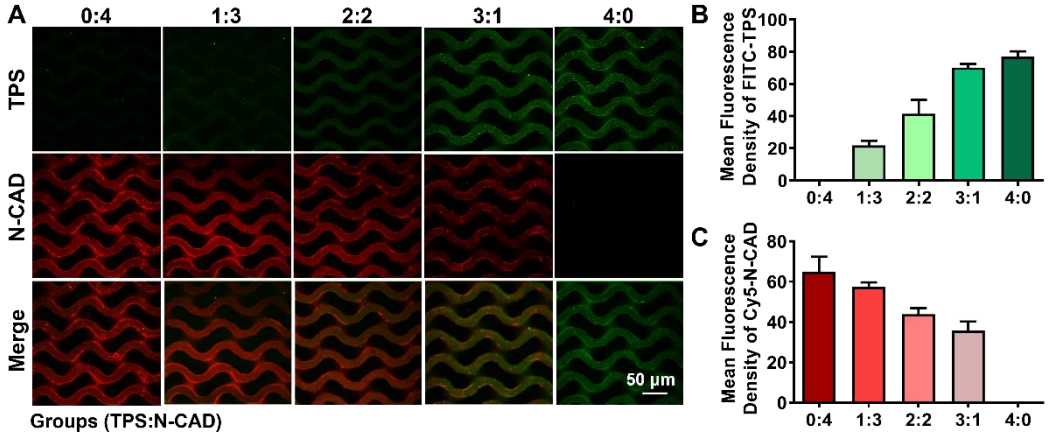

Fig. 4-6. FITC-TPS and Cy5-N-CAD distribution onto G6 scaffold with the ratio of 0:4, 1:3, 2:2, 3:1 and 4:0.

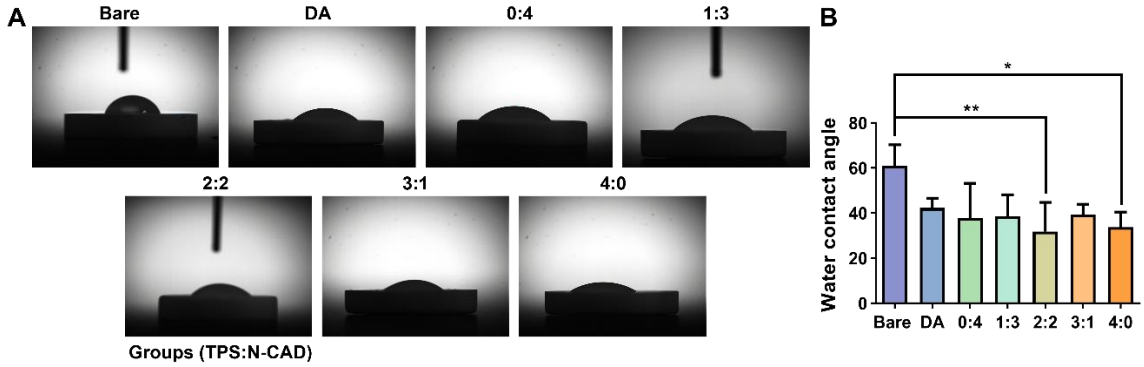

Fig. 4-7. (A) WCA images and (B) quantitative data of bare and coated samples.

4.3.2 *In vitro* biological properties of TPMS-TPS/N-CAD scaffold

4.3.2.1 *In vitro* capture of BMSC and EPC by TPMS-TPS/N-CAD scaffold

To examine the cell capture ability of TPMS-TPS/N-CAD scaffold, BMSCs and EPCs were pre-labeled with cell tracker red, and an extracorporeal circulation system was used. After refluxing for 2 h, bare surface had limited cell adhesion due to hydrophobicity, and coated surfaces had increased cell amount (Fig. 4-8A). Specifically, the N-CAD-containing groups, namely 0:4, 1:3 and 2:2 (TPS:N-CAD), had more

BMSC adhesion (2.62, 2.45, and 2.36 times higher than bare surface; 1.87, 1.75, and 1.69 times higher than DA group) (Fig. 4-8B). For EPCs, the groups with more TPS could capture more cells, and the 4:0 group has the highest cell amount (4.42 times higher than bare group), followed by the 3:1 and 2:2 groups (3.74 and 3.58 times higher than bare group). These results proved that the TPMS-TPS-N-CAD scaffold could capture surrounding BMSCs and EPCs with high efficiency.

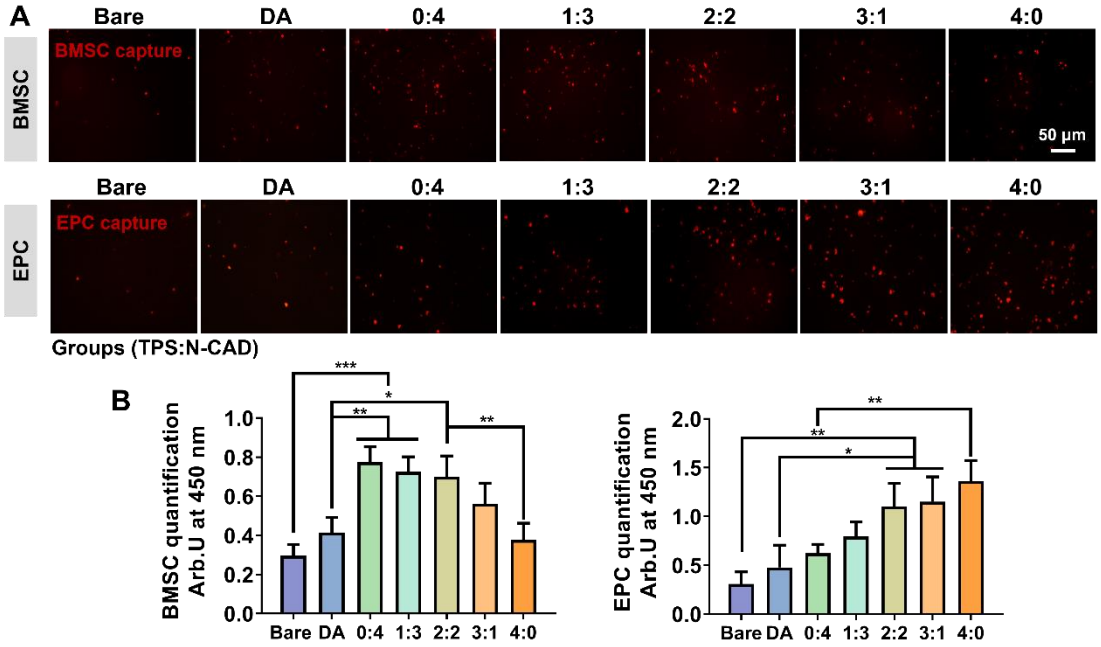

Fig. 4-8. (A) Images of captured BMSC (top) and EPC (bottom) onto each sample after circulation for 2 h. (B) Quantification of captured BMSC (left) and EPC (right) by CCK-8 assay.

All samples were cultivated for an additional 24 and 72 h after refluxing to verify cell viability. Live/dead staining and pico-green DNA quantification were carried out. As shown in Fig. 4-9A and 4-10A, almost no dead cells were on the surface of each sample, indicating low cytotoxicity. After culturing for 24 and 72 h, both BMSCs and EPCs proliferated very well on each surface. Group 0:4 (TPS:N-CAD) was covered by BMSCs at 72 h and had the highest DNA concentration (9.97 ± 0.75 μg/mL), while the 1:3 (9.97 ± 0.81 μg/mL) and 2:2 (7.91 ± 0.90 μg/mL) groups also had a considerable number of BMSCs compared with bare group (1.47 ± 0.38 μg/mL DNA) (Fig. 4-9B). The EPCs amount was positively related with the content of TPS (Fig. 4-10). Undoubtedly, the sample had the highest amount of EPC was found in 4:0 group (7.70 ± 0.62 μg/mL EPC DNA, while the 3:1 and 2:2 groups maintained high EPC number

compared with other groups.

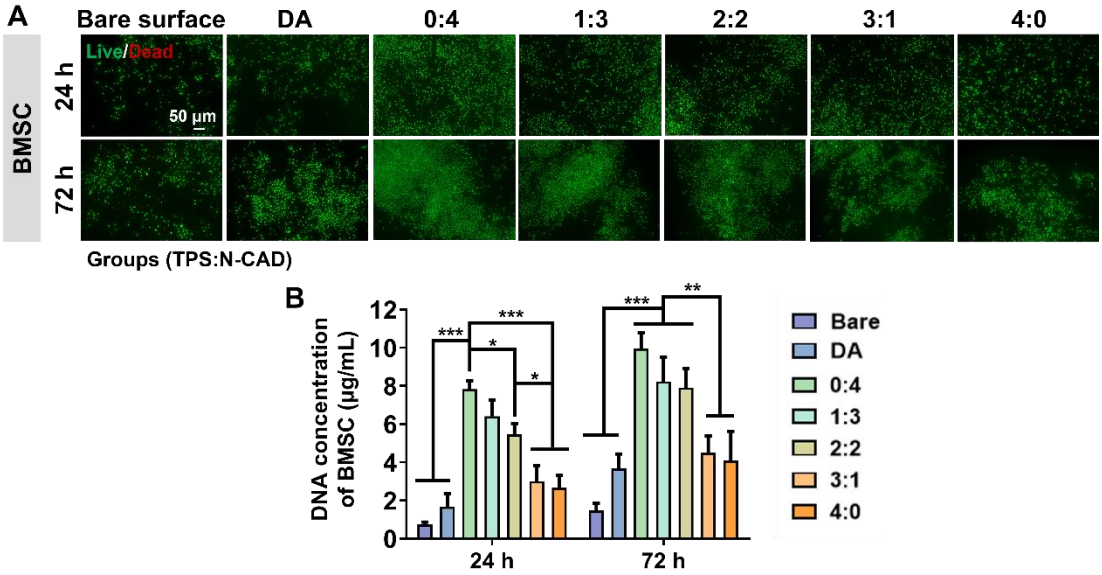

Fig. 4-9. (A) Live/Dead staining of *in vitro* captured BMSC. (B) Cell proliferation of BMSC on different groups by the Picogreen DNA assay.

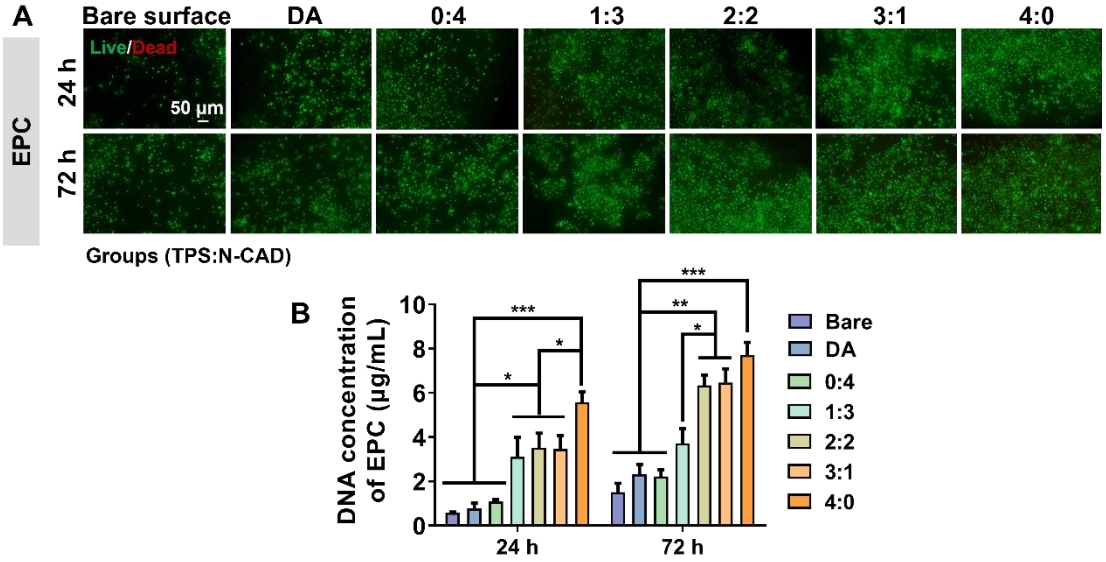

Fig. 4-10. (A) Live/Dead staining of in vitro captured BMSC. (B) Cell proliferation of BMSC on different groups by the Picogreen DNA assay.

4.3.2.2 *In vitro* co-capture of BMSCs and EPCs by TPMS-TPS/N-CAD scaffold

We further examined the ability of different ratios of TPS and N-CAD to capture EPC and BMSC simultaneously. We used cell tracker to label EPC (green) and BMSC (red)

before cell circulation. After 2 h (Fig. 4-11), the numbers of both cells in the bare (50-60 cells/mm^2) and DA (80-90 cells/mm^2) groups were relatively low, whereas the total number of cells trended upward in peptide-modified surfaces, manifested by increased fluorescence signal. Among them, the 0:4 group had the most BMSCs (~565 cells/mm^2), fewest EPCs (~148 cells/mm^2). In contrast, the 4:0 group had the most EPCs (~711 cells/mm^2) and relatively few BMSCs (~175 cells/mm^2). The 2:2 group maintained a relative balance between the two cell types (468 EPCs/mm^2 and 392 BMSCs/mm^2).

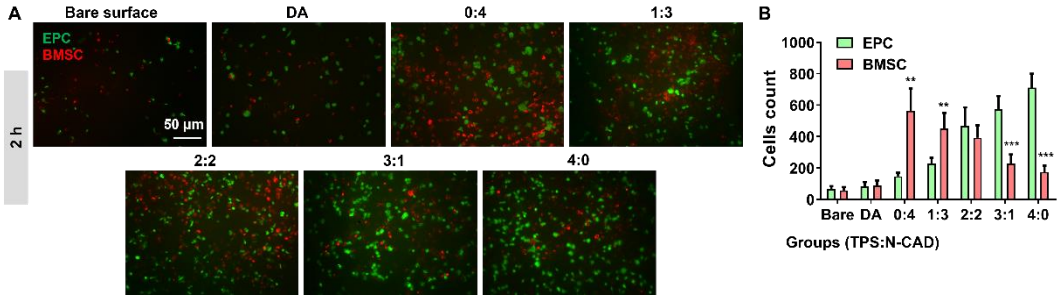

Fig. 4-11. (A) Images of captured BMSC (red) and EPC (green) onto each sample after circulation for 2 h by cell trackers. (B) Quantification of co-captured BMSCs and EPCs by cell count after circulation for 2 h.

After 24 hours of incubation, the cells began to stretch and proliferate (Fig. 4-12). The total cell numbers were still limited in bare and DA surface (~180 and ~400 cells/mm^2, respectively). In contrast, there were more cells in the peptide-modified group overall. Among them, the growth of these two cells was more uniform in the 1:3 (528 EPCs/mm^2 and 684 BMSCs/mm^2) and 2:2 groups (792 EPCs/mm^2 and 578 BMSCs/mm^2). These experimental results demonstrated that our proposed peptide-modified surface captured both BMSC and EPC simultaneously, and that both cell types could grow very well.

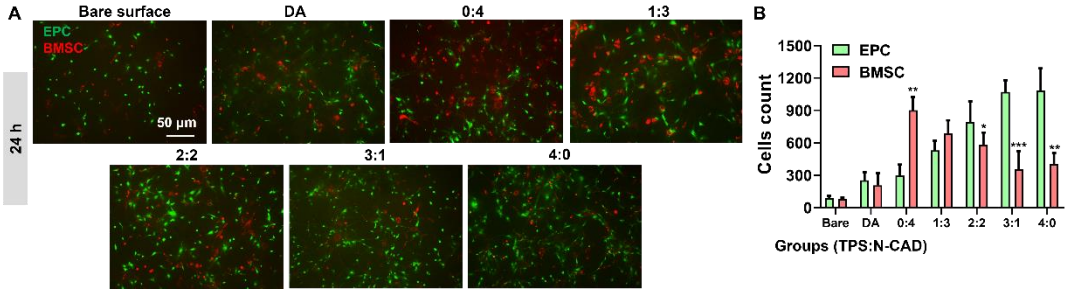

Fig. 4-12. (A) Images of captured BMSC (red) and EPC (green) onto each sample after

circulation for 24 h by cell trackers. (B) Quantification of co-captured BMSCs and EPCs by cell count after circulation for 24 h.

4.3.2.3 *In vitro* osteogenesis of TPMS-TPS/N-CAD scaffold

Because of the remarkable potential for osteogenic differentiation, BMSCs are being exploited for bone tissue regeneration.[182] The use of N-CAD is crucial in regulating osteoblast differentiation and cell-cell interaction during bone formation.[162, 163, 183]

To examine the osteogenic effect of TPMS-TPS/N-CAD scaffold, we first performed ALP analysis, which is a marker of early-stage osteogenesis.[184] Fig. 4-13 shows that the difference in ALP expressions between groups was not very significant on day 7, but the peptide-modified groups still possessed higher ALP expression. After 14 days, the groups with N-CAD had a more purple color rendering, and the ALP activity of the 0:4, 1:3, 2:2 and 3:1 (TPS:N-CAD) groups were significantly higher than that of the bare group.

Following that, we carried out ARS staining, a test for calcium mineral deposition during late osteogenesis. Fig. 4-14 shows that each group had high calcium deposition with a distinct red color. Among them, the 0:4, 1:3 and 2:2 (TPS:N-CAD) groups exhibited deeper red color, indicating more calcium deposition than the other groups.

Furthermore, qRT-PCR was performed to measure the relative expression of osteogenic genes (Fig. 4-15).[177, 185-187] The group containing N-CAD could promote the expression of these osteogenic genes, with the 0:4 group having the most superior performance, while the 1:3 and 2:2 groups showed comparable performance. The above results suggest that our proposed scaffold provided a good osteogenic microenvironment to promote osteogenic differentiation of BMSC.

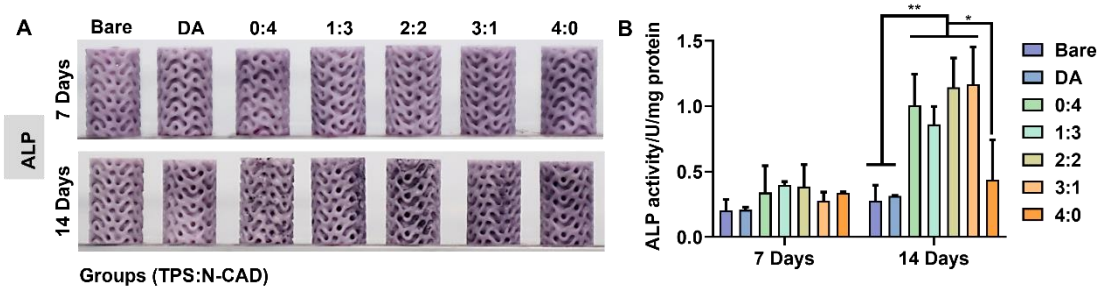

Fig. 4-13. (A) ALP images of the seeded BMSC onto each sample, which represented early-stage osteogenesis. (B) quantification of ALP activity.

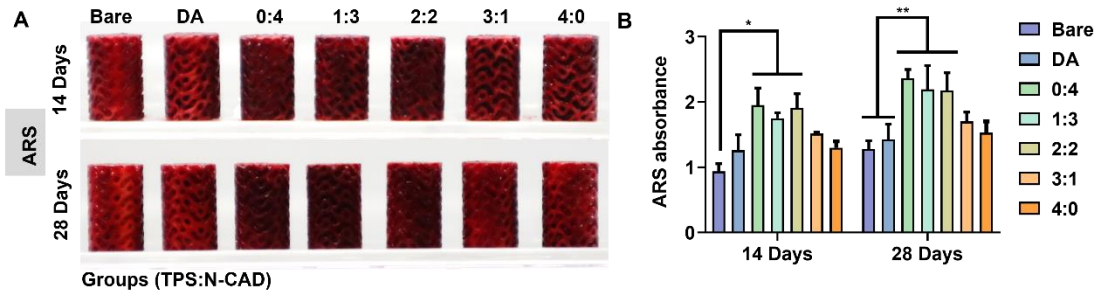

Fig. 4-14. (A) ARS images of the seeded BMSC onto each sample, which represented to late-stage osteigenesis. (B) ARS absorbance at 592 nm.

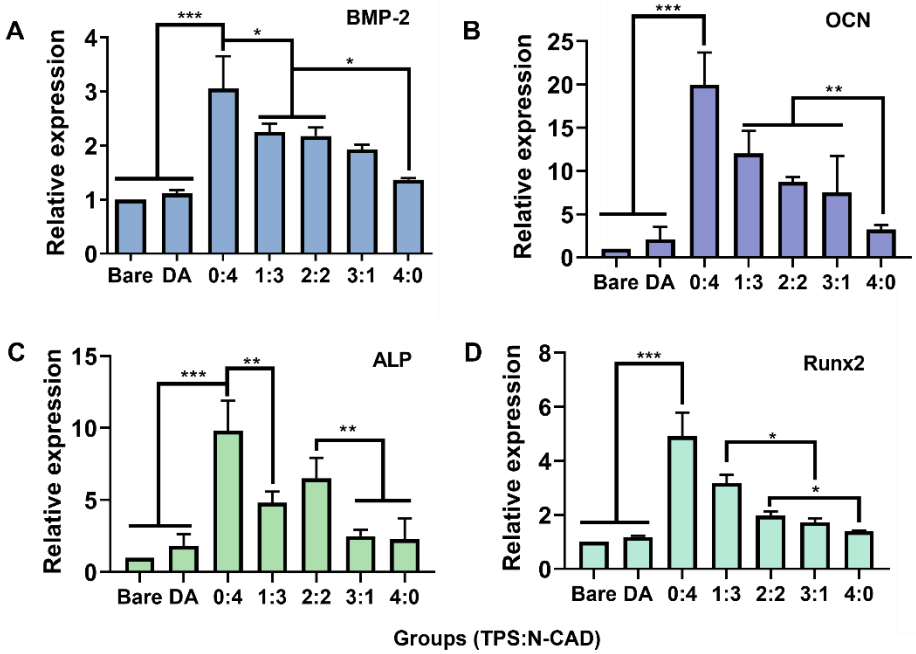

Fig. 4-15. Expression of osteogenic genes (BMP-2, OCN, ALP and Runx2).

4.3.2.4 *In vitro* angiogenesis of TPMS-TPS/N-CAD scaffold

As a highly vascularized tissue, the integrity of bone depends on the spatiotemporal connection between blood vessels and bone cells. The new blood vessels facilitates the transportation of some functional substances to the defect site, such as nutrients, oxygen, growth factors and cells.[188, 189] EPCs can be recruited to the sites that need vascular repair, and have the potential to differentiate into ECs, thereby promoting angiogenesis.[190, 191]

Here, the angiogenic effect of EPC-adhered TPMS-TPS/N-CAD scaffold was

investigated. In CD31 (an angiogenic marker) immunofluorescence staining, the group containing more TPS had higher green fluorescence. Among them, the 2:2, 3:1 and 4:0 (TPS:N-CAD) groups had 1.79 and 2.16 and 2.22 times higher fluorescence intensity than the bare group, respectively (Fig. 4-16). To further analyze the angiogenic potential, angiogenic genes CD31, VEGF, ANG and VWF were tested (Fig. 4-17).[192-194] The 4:0 group possessed the highest gene expression, while 2:2 and 3:1 group also had good angiogenic behaviors. Yet the 0:4 and 1:3 groups had relatively low gene levels among all the peptide-modified groups. Conclusively, these results reinforced the statement that the incorporation of TPS into TPMS scaffold could aid EPC adhesion and promote angiogenesis.

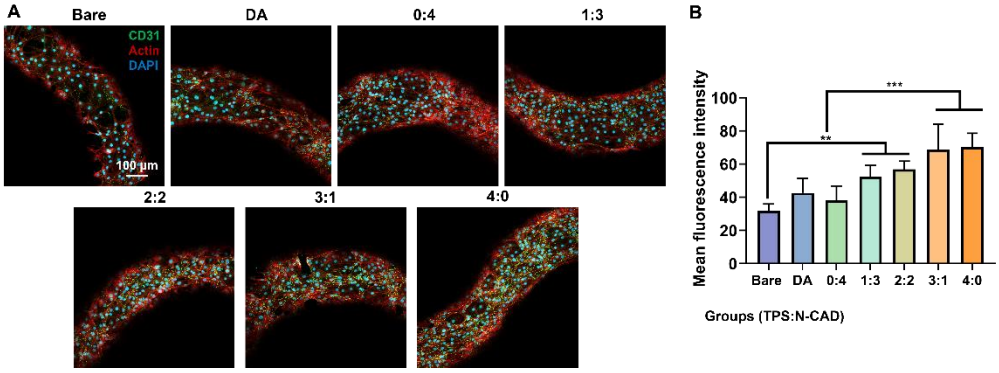

Fig. 4-16. (A) CD31 (an angiogenic marker) immunofluorescence staining of the seeded EPCs onto each sample. (B) Quantification of fluorescence intensity.

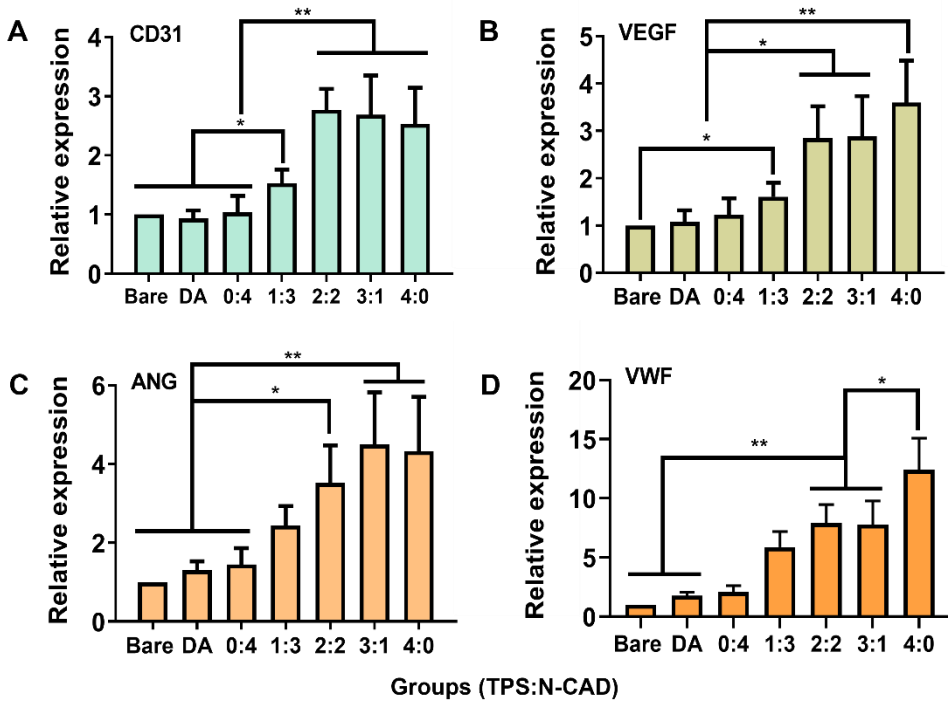

Fig. 4-17. Expression of angiogenesis-related genes (CD31, VEGF, ANG and VWF).

4.3.2.5 Paracrine signaling between BMSC and EPC in TPMS-TPC/N-CAD scaffold

Extensive research has demonstrated the significance of intercellular interactions such as paracrine signaling are essential in bone formation.[195-197] Scientists found that endothelial-like cells and bone marrow-derived cells ultimately enhance osteogenesis-related differentiation and angiogenesis through the paracrine effect by producing bio-functional substances.[198, 199] Specifically, EPCs and ECs secrete BMP-2, a major signaling molecule for cell differentiation into osteoblasts and mineral deposition, which promotes osteogenesis.[196, 200] On the other hand, osteoblasts and their precursor cells can secrete VEGF, which induces endothelial-like cell growth and differentiation to form new vessels.[201, 202] Moreover, one of the key aspects of this interplay is the spontaneous production of NO by the cells themselves; the molecule stimulates the NO-cGMP pathway to coordinate bone and vascular cell behaviors.[66, 177, 203] The mutual communication and secretion of bio-functional substances contribute to the successful formation of new bone tissue and vascular networks, facilitating the overall healing process.[195] Therefore, promoting intercellular paracrine interactions by enhancing autologous cell adhesion at the defect site is a

promising strategy. Our proposed TPMS-TPC/N-CAD scaffold could specifically enhance EPC and BMSC attachment to the scaffold and had the potential to promote their interaction. Therefore, a series of experiments on paracrine and autocrine effects were carried out.

4.3.2.5.1 Paracrine effects of BMSCs on EPCs

Since BMSCs can secrete VEGF to promote angiogenesis of EPCs, a transwell system was applied to better perform paracrine experiments, in said system, the scaffolds seeded with BMSCs were placed in the upper chamber, while EPCs spread in the lower well, with various cytokines produced in the upper chamber diffusing downward (Fig. 4-18A and B). We first measured VEGF production by BMSCs; the 0:4 and 3:1 (TPS:N-CAD) groups had high VEGF levels, which had good potential for stimulating EPC angiogenesis (Fig. 4-18C). To investigate angiogenesis effects, wound closure and tube formation assay were conducted. In Fig. 4-19, the bare, DA and 4:0 groups had weaker scratch healing effects (20%-30% healing), while the 0:4, 1:3 and 2:2 groups healed about 50% or more under the influence of VEGF. In tube formation assay (Fig. 4-20), a lot of vascular-like networks appeared in 0:4, 1:3 and 2:2 (TPS:N-CAD) group after 8 h of incubation, and the number of branch points as well as the total length (40 ± 3 points and 39.82 ± 2.61 μm in 0:4 group, 35 ± 2 points and 35.99 ± 1.10 μm in 1:3 group, 32 ± 2 points and 32.89 ± 2.76 μm in 2:2 group) of these groups were higher than others, suggesting the superior capability to form vascularized networks.

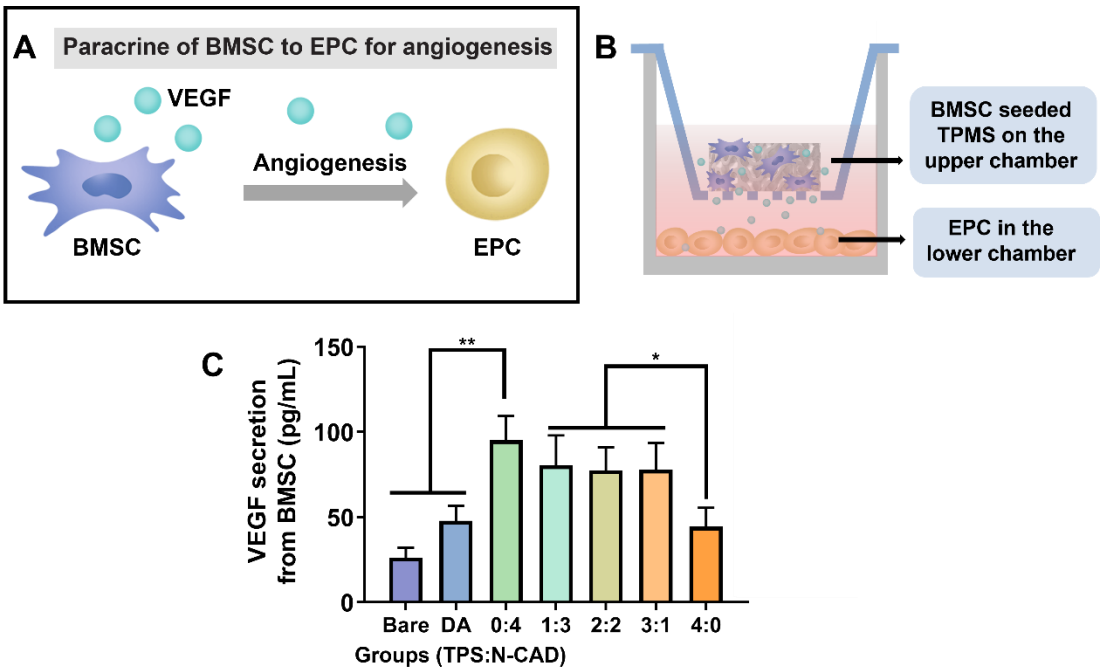

Fig. 4-18. (A) Schematic of the paracrine of BMSC to EPC for angiogenesis. (B) A transwell system was used to evaluate the paracrine of BMSC to EPC. (C) Quantification of VEGF secretion from BMSC.

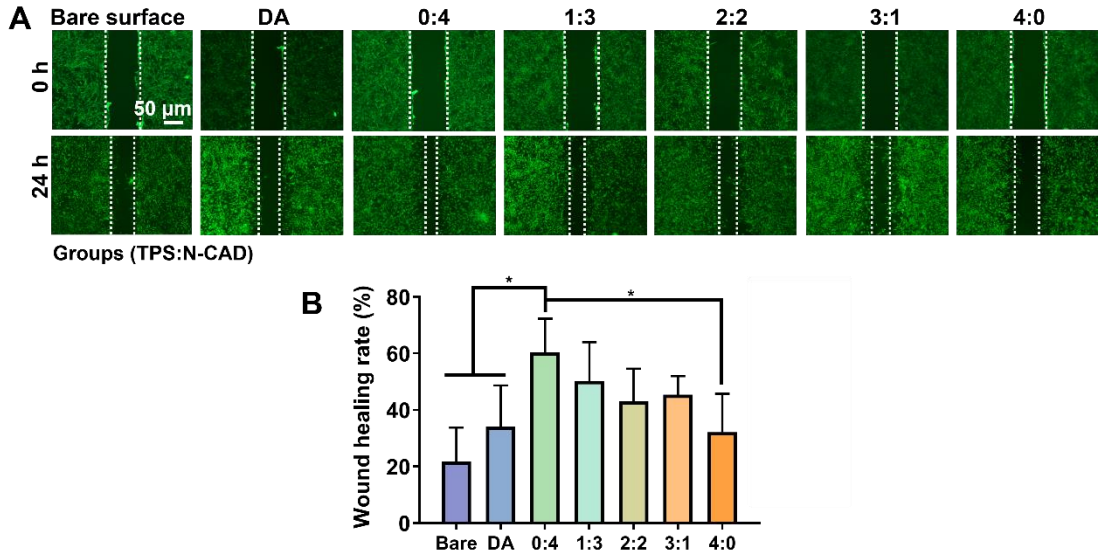

Fig. 4-19. (A) Wound closure images of 0 and 24 h of EPC. (B) Quantification of wound healing rate of EPC under the influence of BMSC. Increased EC migration could attributed to VEGF secretion.

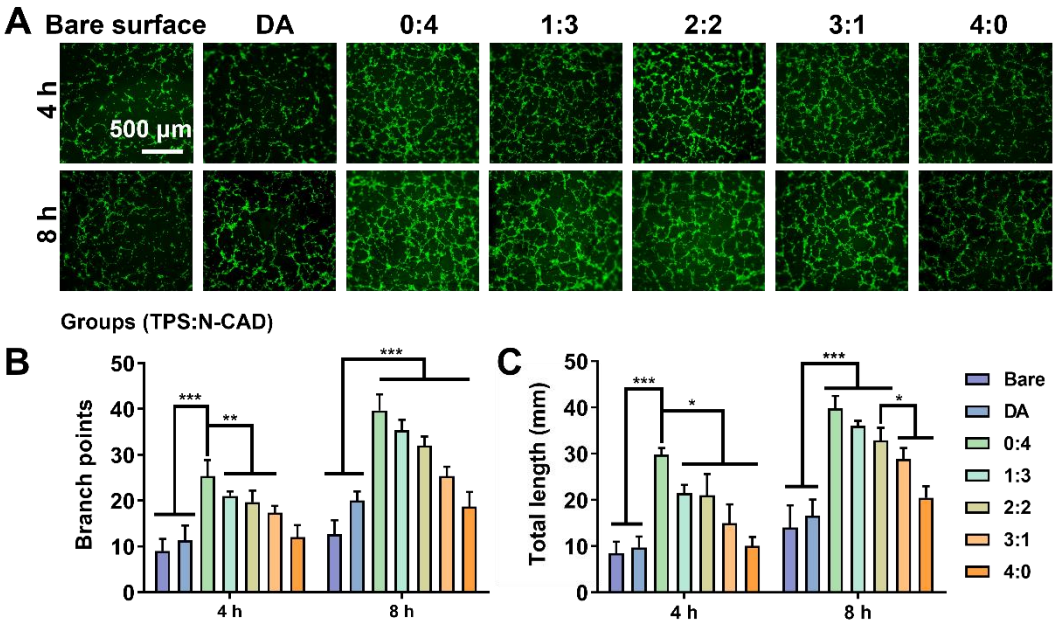

Fig. 4-20. (A) Tube formation images of 4 and 8 h of EPC under the influence of BMSC *in vitro*. (B) Branch points and (C) total length of 4 and 8 h of EPC under the influence of BMSC *in vitro*.

4.3.2.5.2 Paracrine effects of EPCs on BMSCs

BMP-2 can be secreted by EPCs to encourage osteogenic development, a transwell system was adopted, where the upper chamber housed the scaffold seeded with EPCs and the lower chamber contained BMSCs (Fig. 4-21A and B). The quantification of BMP-2 secretion (Fig. 4-21C) showed that 2:2, 3:1 and 4:0 (TPS:N-CAD) groups had greater increase in BMP-2 levels, which were around 2 times higher than bare group. Then, in OCN immunofluorescence staining (Fig. 4-22), a distinct green fluorescence around the nucleus could be found in these three groups, implying an enhanced osteogenic signal. Furthermore, we used a fluorescent probe to label the calcium ions (Fig. 4-23) and showed that the 2:2, 3:1 and 4:0 groups had a stronger fluorescent signal (1.98 times more calcium ions than the bare group). These results suggested that BMSCs could exhibit better osteogenesis in the presence of EPCs due to paracrine effects.

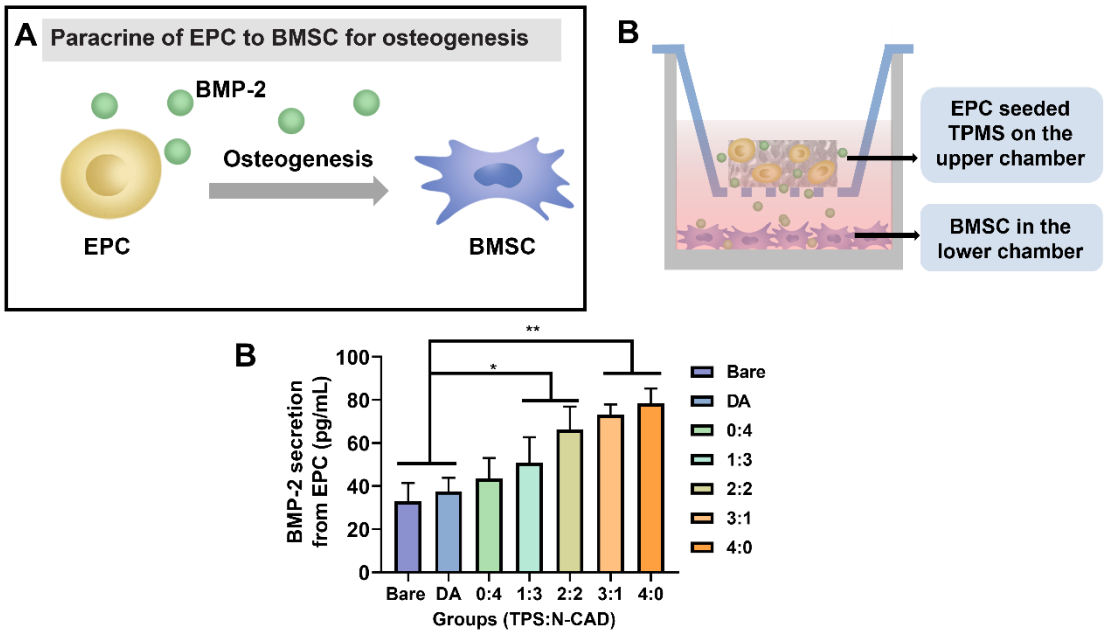

Fig. 4-21. (A) Schematic of the paracrine of EPC to BMSC for osteogenesis. (B) A transwell system was used to evaluate the paracrine of EPC to BMSC. (C) Quantification of BMP-2 secretion from EPC.

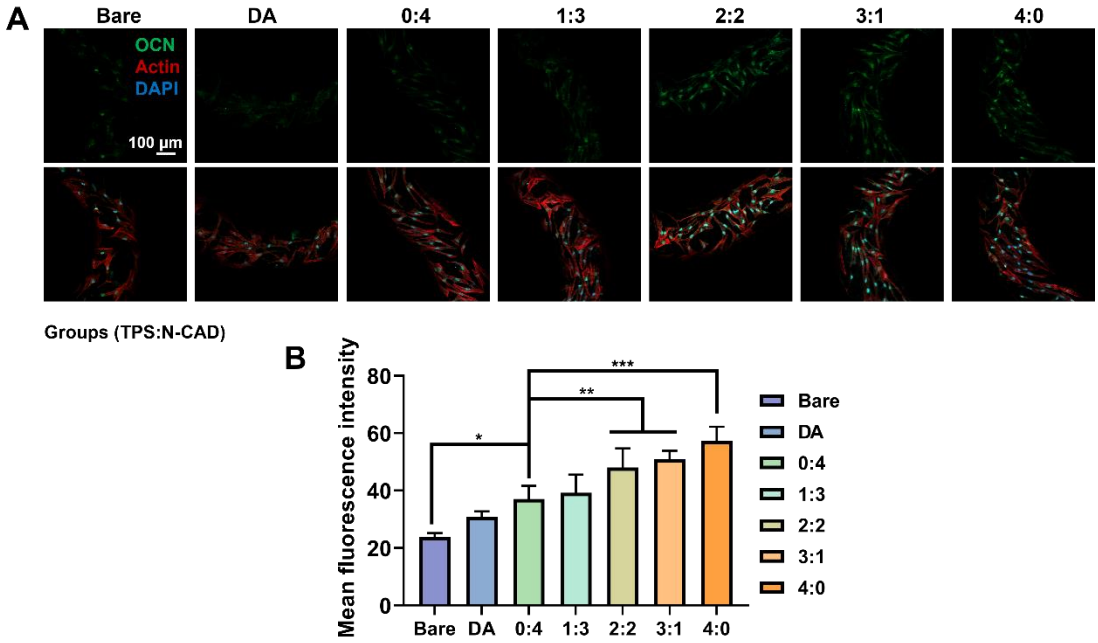

Fig. 4-22. (A) OCN (an osteogenic marker) immunofluorescence staining of the BMSC under the influence of EPC *in vitro*. (B) Quantification of fluorescence intensity.

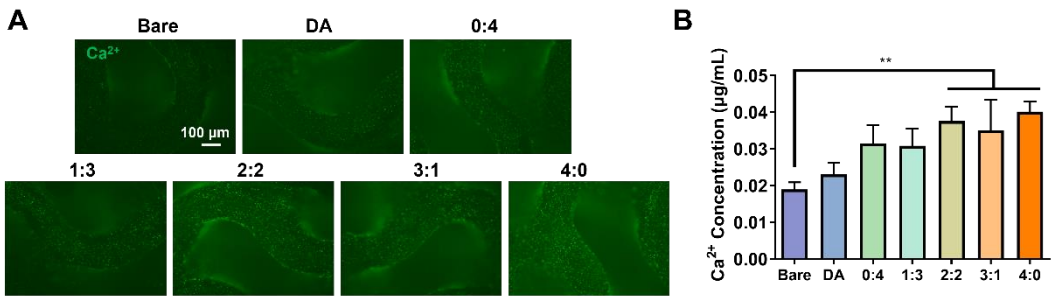

Fig. 4-23. (A) Fluorescent picture of calcium ions in BMSC. (B) Quantification of calcium ion concentrations.

4.3.2.5.3 Evaluation of NO production and osteogenic-angiogenic effects of BMSCs-EPCs co-captured scaffold

NO can coordinate osteogenesis and angiogenesis by NO-cGMP pathway (Fig. 4-24A), and our previous studies showed that the increased cell adhesion could spontaneously produce NO. Hence, we hypothesized that the scaffold could produce NO by the adherent cells.[66, 203, 204] After the co-capture of EPCs and BMSCs, the NO production in 2:2, 3:1 and 4:0 groups was higher (shown by fluorescence) compared with other groups, indicating that our proposed scaffolds can spontaneously produce NO by increasing the adhesion of EPCs and BMSCs without adding exogenous NO-producing substances (Fig. 4-24B and C). The cGMP levels in co-capture scaffolds (Fig. 4-25) had a significant increase of about 18 nM for the 2:2, 3:1 and 4:0 groups, indicating that this autologous production of NO had a synergistic osteogenic and angiogenic potential.

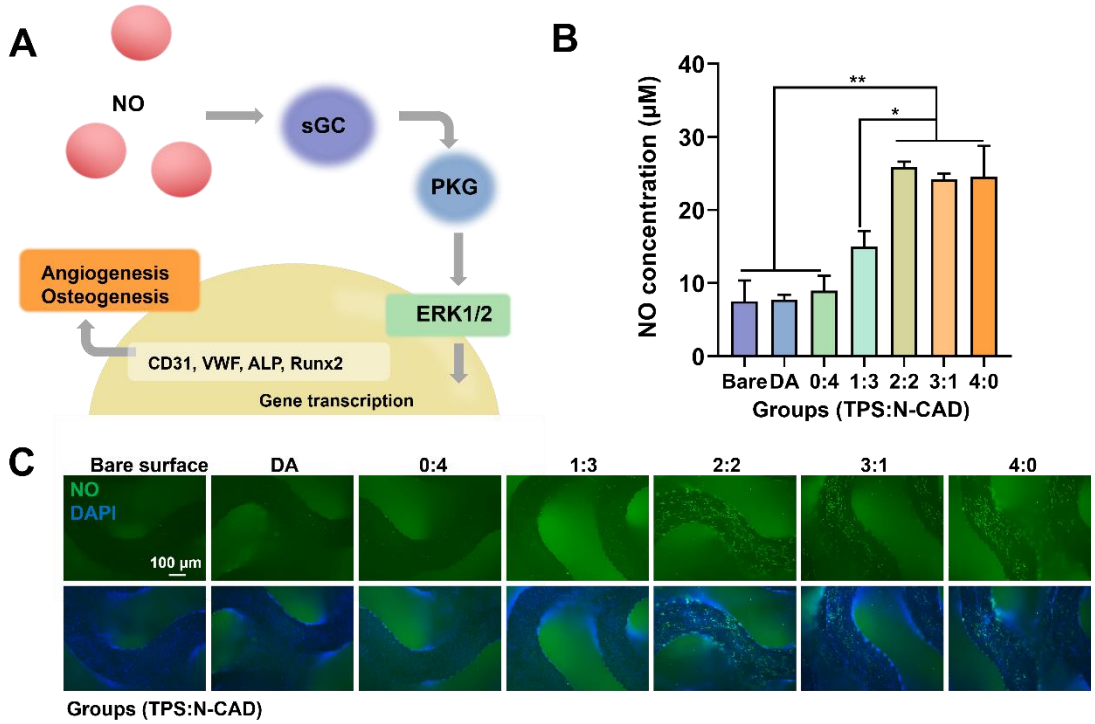

Fig. 4-24. (A) Illustration of NO-cGMP pathway to promote angiogenesis and osteogenesis. (B) NO production from EPCs, BMSCs and co-capture scaffolds. (C) Fluorescent pictures of cellular NO signals in co-capture scaffolds.

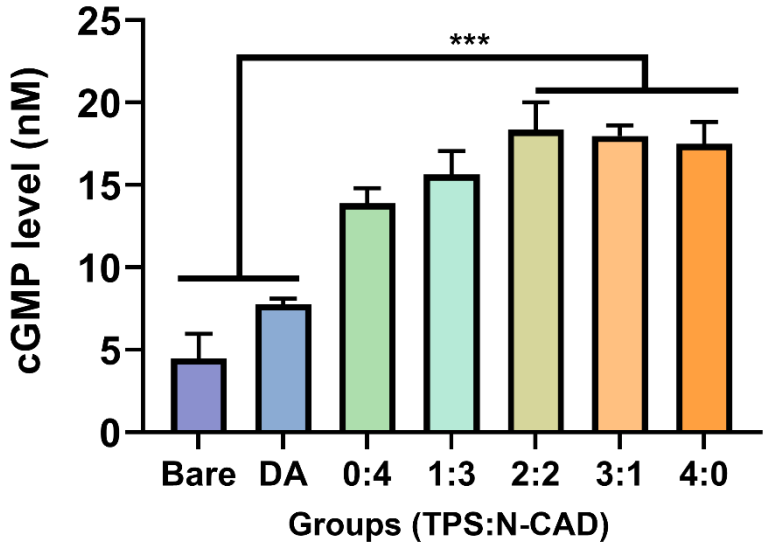

Fig. 4-25. cGMP levels in co-capture scaffolds.

From the above experiments, our TPS-N-CAD scaffold could attract both EPCs and BMSCs, which could coordinate with each other to promote osteogenesis and angiogenesis through BMP-2, VEGF and NO. Therefore, we examined the expressions

of osteogenic and angiogenic genes in the co-capture scaffold. In Fig. 4-26, different degrees of gene upregulation were found, and the 2:2 group had a relatively high expression.

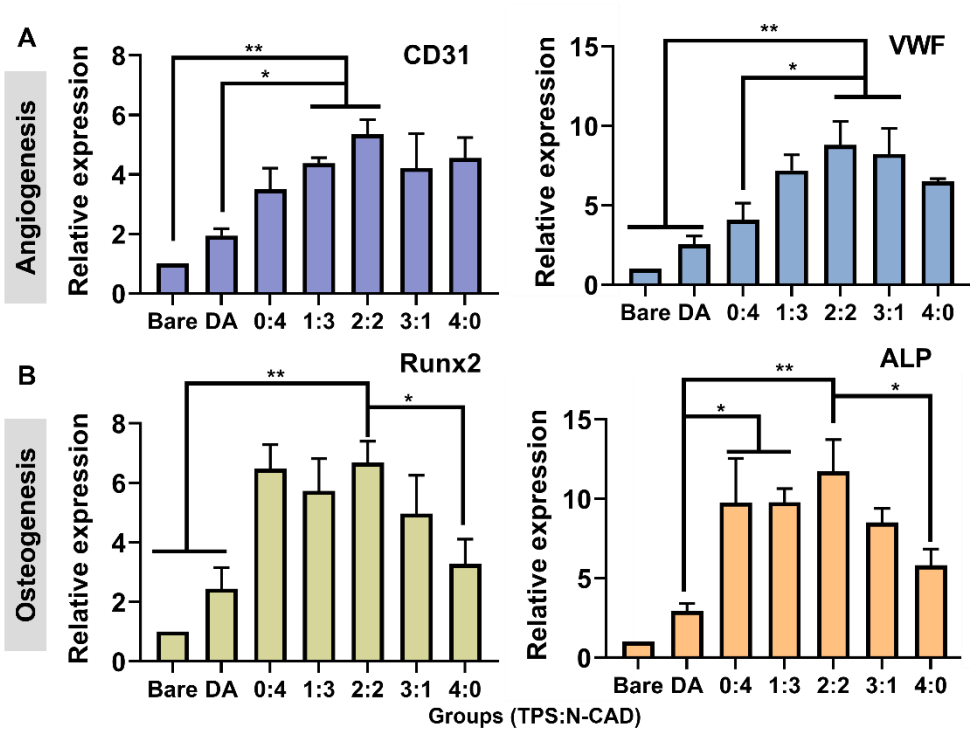

Fig. 4-26. Expressions of (A) angiogenesis and (B) osteogenesis-related genes (CD31, VWF, Runx2 and ALP).

In order to better select a grafting ratio, we scored each function of the scaffold, and put the results into a heat map, in which the blue color meant better function (Fig. 4-27). The bare and DA groups had lower scores, while the groups that had pure TPS (0:4 group) or N-CAD (4:0 group) performed well only in certain criteria, and they lacked the ability to coordinate vascularization or osteogenesis. 1:3 and 3:1 groups had low scores for many functions (such as EPC/BMSC growth and osteogenic/angiogenic ability). We finally chose the 2:2 group for the follow-up experiments; it was not the best performer in any particular functions but was able to balance osteogenesis and angiogenesis.

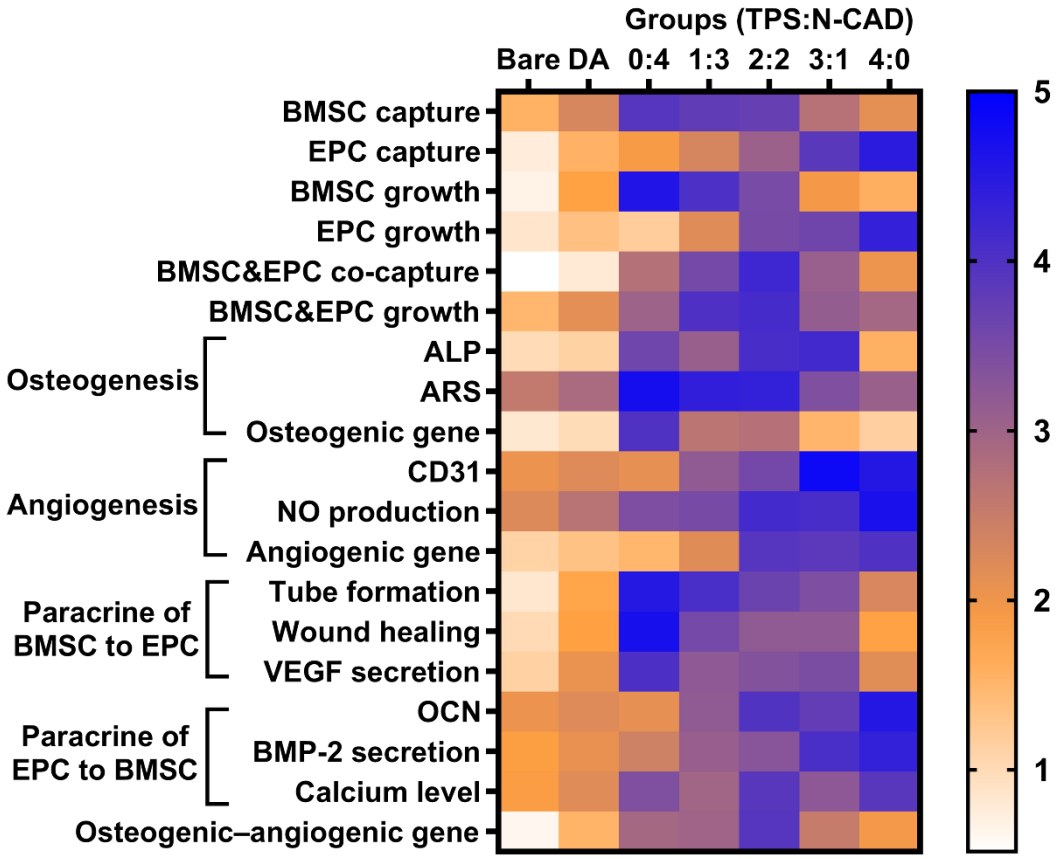

Fig. 4-27. The heat map for the evaluation of *in vitro* TPS/N-CAD-TPMS behaviors.

4.3.3 *In vivo* therapeutic efficiency of TPMS-TPS/N-CAD scaffold

To investigate the bone repair effect of TPS-N-CAD-TPMS scaffolds *in vivo*, a rabbit femoral defect model was established (Fig. 4-28). We set up three groups in total: blank groups (without scaffold implantation), bare-TPMS and TPS-N-CAD-TPMS groups. All samples were scanned with micro-CT to evaluate new bone (red) within the scaffold (green) via 3D reconstruction. As shown in Fig. 4-39A, the blank group had a small red area, representing limited new bone production, while the TPMS scaffold groups were surrounded by new bone and showed clear red signals both outside and inside the scaffolds, representing efficient bone regeneration. Furthermore, the quantitative results showed that the blank group had limited BMD (0.122 ± 0.02 g/cm^3) and BV/TV (~5.74%) at 8 weeks, while the bare-TPMS showed high BMD and BV/TV, which were 0.395 ± 0.03 g/cm^3 and 9.01%, respectively. Among all the groups, TPS-N-CAD-TPMS showed the highest values (0.499 ± 0.03 g/cm^3 BMD and 11.83% BV/TV), representing the best new bone formation and emphasizing its potential to support bone repair.

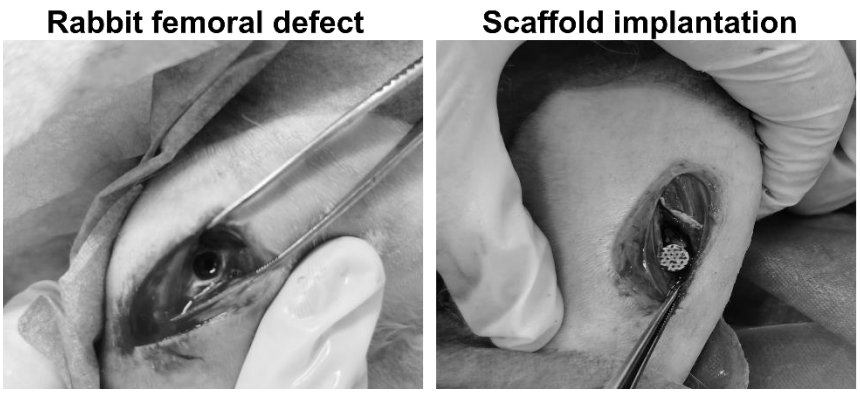

Fig. 4-28. Representative macroscopic images of rabbit femoral defect and TPMS scaffold implantation. A round defect was made onto the femoral condyle and the TPMS scaffolds (Ø5 mm × 8 mm) were implanted into the defect site.

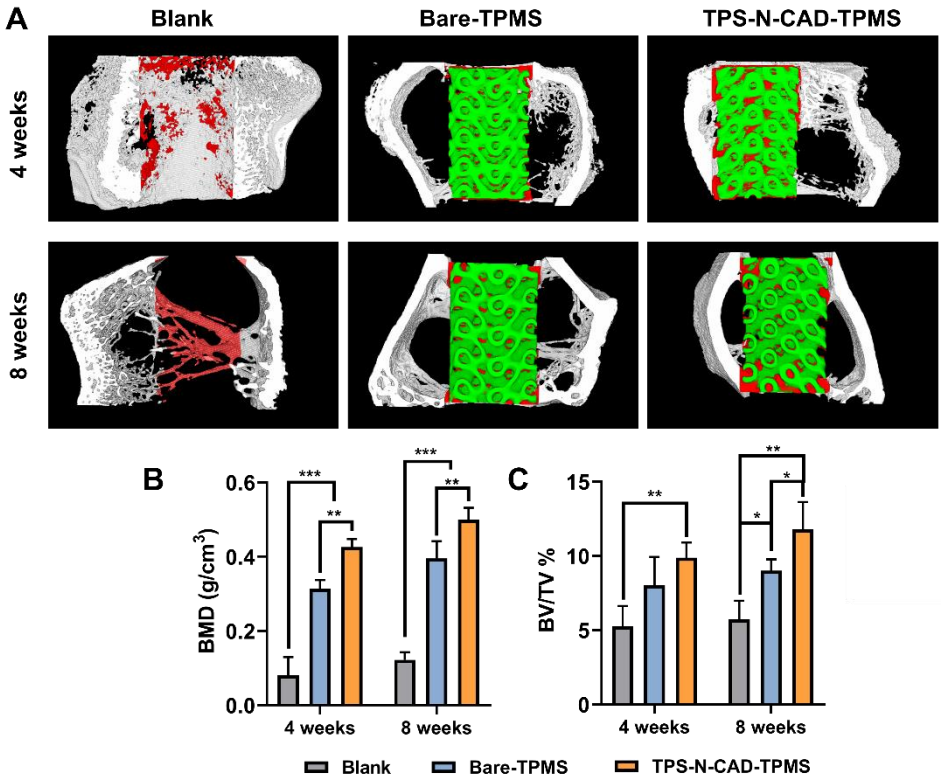

Fig. 4-29. (A) 3D images of blank, bare-TPMS and TPS-N-CAD-TPMS (red and green color represented the new bone and scaffolds). Quantification of (B) BMD and (C) BV/TV.

4.4 Summary

In this project, we constructed a TPS-N-CAD-TPMS scaffold that could capture autologous cells for osteogenesis and angiogenesis. The curvilinear helical structure of the TPMS structure provided a large surface area and more reaction sites for surface modification and cell adhesion. Then, we used a simple, green and fast bio-orthogonal click reaction to attach TPS peptide and N-CAD peptide onto the scaffold, which could selectively capture EPCs and BMSCs *in situ*. The adherent cells on the scaffold were able to produce bio-functional molecules such as VEGF, BMP-2 and NO through paracrine effects, which synergistically facilitated osteogenesis and angiogenesis. The TPS-N-CAD-TPMS scaffold provided a good growth environment for BMSCs and EPCs and showed superior ability of bone regeneration and neovascularization. Our proposed TPS-N-CAD-TPMS scaffold avoided the introduction of exogenous cells, drugs and growth factors, and rebuilt a biomimetic microenvironment by attracting autologous cells, which not only saves costs, but also improves the safety of the scaffold, making this scaffold the most promising next-generation bone repair scaffold.

Chapter 5 Conclusions and recommendations for future work

5.1 Major findings and conclusion

In the first project, we constructed a self-sustaining coating consisting of a DA-Cu network, NO precursor arginine, and the endothelial glycocalyx heparin. The DCAH coating generated NO by catalytic effect and used heparin to enhance the level of eNOS in ECs, thus promoting the release of NO from arginine and overcoming the insufficient NO production due to lack of endogenous NO donor (RSNOs) *in vivo*. Our proposed coating could continuously produce NO and promote EC growth at any conditions (with or without RSNOs), while inhibiting SMC proliferation/migration and platelet adhesion. In a rabbit model, the DCAH stent could effectively reduce thrombosis and restenosis, thereby decreasing the incidence of stenting complications.

In the second project, inspired by previous experiments, we envisioned that if more ECs adhered onto the stents, they would spontaneously produce NO and promote reendothelialization to form a natural barrier that prevented excessive SMC migration and platelet aggregation. Therefore, we introduced VEGF into the DCAH system to prepare AHV coatings. Our proposed AHV coating could rapidly recruit ECs, which corresponded to early-stage endothelium formation. Meanwhile, the AHV coating preferred EC over platelets, greatly reducing the possibility of thrombus. In *ex vivo* experiment, thrombus was reduced on the surface of the AHV coating. The subsequent *in vivo* results exhibited that the AHV coating rapidly developed an endothelial layer. Combined with the continuous production of NO in a self-sustainable manner, AHV could reduce endothelial hyperplasia, which was of great importance for vascular stents.

In the third project, based on our previous study, we designed a TPMS bone scaffold capable of selectively capture BMSCs and EPCs. The adherent cells could produce growth factors and NO to regulate osteogenesis and angiogenesis simultaneously. This scaffold avoided the introduction of exogenous cells, drugs and growth factors and could rebuild a microenvironment that mimicked natural bone by recruiting autologous cells. From the perspective of scaffold design, TPMS had a bone-

mimicking curvature structure with a large surface area that facilitated surface modification as well as cell adhesion. In terms of preparation, we adopted a simple dipping method, and used the green and fast orthogonal click reaction to attach TPS peptide and N-CAD peptide onto the scaffold surface with high reproducibility and simplicity. After scaffold implantation, TPS and N-CAD could attract EPCs and BMSCs, respectively. The increased cells adhesion to the scaffold would produce various bio-functional molecules such as VEGF, BMP-2 and NO through paracrine effects, thus synergistically promoting osteogenesis and angiogenesis. Our scaffold could capture cells in a dynamically circulating system and provided a conducive environment for cell growth. We then demonstrated the role of the scaffold in angiogenesis and osteogenesis and explored its NO production and paracrine factor secretion as well as cell-cell interactions. At last, we confirmed that the TPS-N-CAD-TPMS scaffold could promote bone repair, serving as a benchmark for the clinical application of bone scaffolds.

Overall, we have explored the multiple strategies of NO production, studied cell behaviors under the regulation of NO in these three projects and investigated NO application in cardiovascular diseases and bone repair. Our designed NO-producing materials are simple, feasible and easily scalable for clinical translation and subsequent commercialization, providing a new way to accelerate disease treatment and tissue repair.

5.2 Recommendations for future work

Although we have designed a series of NO production platforms and achieved good therapeutic effects, it is undeniable that there are still some shortcomings. For example, we should also explore the application of stents in cardiovascular disease modeling, which is difficult. Future experiments should use disease animals to systematically investigate the therapeutic effects of stents in actual pathological situations. In addition, for the TPMS bone scaffold project, we should also investigate the captured of cells *in vivo*. However, the differentiation of EPCs and BMSCs may lead to the loss of certain protein expressions, so it is difficult to label the adherent cells with specific antibodies of EPCs and BMSCs, which would confuse the final staining effect. Future experiments

should explore more convenient methods to examine the scaffold behaviors *in vivo*.

Furthermore, the demand for NO in the lesion site is not always urgent or needed, and the required amounts of NO are also different. For example, in some diseases dominated by inflammation, NO is a double-edged sword since its uncontrolled production prolongs the inflammatory response, which is detrimental to disease treatment. Additionally, for implants, an initially high flux of NO is beneficial for antibacterial purposes, while a small amount of NO at a later stage is conducive for regulating cell behaviors. Meanwhile, for tumor therapy, a minor amount of NO promotes cancer, while only a high concentration of NO can suppress tumors. Therefore, future work should develop a smart platform to release NO on-demand in accordance with the pathological development. In addition, NO can regulate energy and metabolism, which determines cell growth, proliferation, migration and differentiation, and is highly relevant to various diseases. Hence, the role of NO should be further explored in such context, and the advancement of knowledge will help deepen the understanding of the effects of NO on cell behaviors.

In conclusion, there are still many unresolved concerns in NO-producing platforms, but we believe that with continuous research, we will be able to apply these materials to benefit a variety of disease treatments.

References:

[1] F. Murad, Discovery of some of the biological effects of nitric oxide and its role in cell signaling (Nobel lecture), Angewandte Chemie International Edition 38(13-14) (1999) 1856-1868.
[2] J. Chen, R. Yang, M. Buzanowski, J. Cichanowicz, Cold selective catalytic reduction of nitric oxide for flue gas applications, Industrial & engineering chemistry research 29(7) (1990) 1431-1435.
[3] G. Goldenbaum, R. Dickerson, Nitric oxide production by lightning dischargininees, Journal of Geophysical Research: Atmospheres 98(D10) (1993) 18333-18338.
[4] M. Nicholls, Nitric oxide discovery Nobel Prize winners: Robert F. Furchgott, Louis J. Ignarro, and Ferid Murad shared the Noble Prize in 1998 for their discoveries concerning nitric oxide as a signalling molecule in the cardiovascular system, European Heart Journal 40(22) (2019) 1747-1749.
[5] R. SoRelle, Nobel prize awarded to scientists for nitric oxide discoveries, Circulation 98(22) (1998) 2365-2366.
[6] D.E. Koshland Jr, The molecule of the year, Science 258(5090) (1992) 1861-1861.
[7] M. Tirone, V. Conti, F. Manenti, P.A. Nicolosi, C. D'Orlando, E. Azzoni, S. Brunelli, Nitric oxide donor molsidomine positively modulates myogenic differentiation of embryonic endothelial progenitors, Plos one 11(10) (2016) e0164893.
[8] Y. Sagi, M. Heiman, J.D. Peterson, S. Musatov, M. Scarduzio, S.M. Logan, M.G. Kaplitt, D.J. Surmeier, N. Heintz, P. Greengard, Nitric oxide regulates synaptic transmission between spiny projection neurons, Proceedings of the National Academy of Sciences 111(49) (2014) 17636-17641.
[9] C. Bogdan, Nitric oxide synthase in innate and adaptive immunity: an update, Trends in immunology 36(3) (2015) 161-178.
[10] J. Lei, Y. Vodovotz, E. Tzeng, T.R. Billiar, Nitric oxide, a protective molecule in the cardiovascular system, Nitric Oxide 35 (2013) 175-185.
[11] S. Kashiwagi, Y. Izumi, T. Gohongi, Z.N. Demou, L. Xu, P.L. Huang, D.G. Buerk, L.L. Munn, R.K. Jain, D. Fukumura, NO mediates mural cell recruitment and vessel morphogenesis in murine melanomas and tissue-engineered blood vessels, The Journal of clinical investigation 115(7) (2005) 1816-1827.
[12] S. Moncada, A. Higgs, The L-arginineinine-nitric oxide pathway, New England journal of medicine 329(27) (1993) 2002-2012.
[13] F.J. Corpas, S. González-Gordo, J.M. Palma, Nitric oxide and hydrogen sulfide modulate the NADPH-generating enzymatic system in higher plants, Journal of Experimental Botany 72(3) (2021) 830-847.
[14] T.M. Paravicini, R.M. Touyz, NADPH oxidases, reactive oxygen species, and hypertension: clinical implications and therapeutic possibilities, Diabetes care 31(Supplement_2) (2008) S170-S180.
[15] M. Li, Y. Fan, X. Zhang, W. Hou, Z. Tang, Fruit and vegetable intake and risk of type 2 diabetes mellitus: meta-analysis of prospective cohort studies, BMJ open 4(11) (2014) e005497.

[16] J.L. Zweier, P. Wang, A. Samouilov, P. Kuppusamy, Enzyme-independent formation of nitric oxide in biological tissues, Nature medicine 1(8) (1995) 804-809.
[17] J.O. Lundberg, E. Weitzberg, Nitric oxide signaling in health and disease, Cell 185(16) (2022) 2853-2878.
[18] C.T. Yeo, J.S. Stancill, B.J. Oleson, J.K. Schnuck, J.D. Stafford, A. Naatz, P.A. Hansen, J.A. Corbett, Regulation of ATR-dependent DNA damage response by nitric oxide, Journal of Biological Chemistry 296 (2021).
[19] D. Fukumura, S. Kashiwagi, R.K. Jain, The role of nitric oxide in tumour progression, Nature Reviews Cancer 6(7) (2006) 521-534.
[20] J. Emerit, C. Beaumont, F. Trivin, Iron metabolism, free radicals, and oxidative injury, Biomedicine & pharmacotherapy 55(6) (2001) 333-339.
[21] A.W. Carpenter, M.H. Schoenfisch, Nitric oxide release: Part II. Therapeutic applications, Chemical Society Reviews 41(10) (2012) 3742-3752.
[22] Y. Qian, R. Kumar, M.K. Chug, H. Massoumi, E.J. Brisbois, Therapeutic delivery of nitric oxide utilizing saccharide-based materials, ACS applied materials & interfaces 13(44) (2021) 52250-52273.
[23] N. Sayed, D.D. Kim, X. Fioramonti, T. Iwahashi, W.N. Durán, A. Beuve, Nitroglycerin-induced S-nitrosylation and desensitization of soluble guanylyl cyclase contribute to nitrate tolerance, Circulation research 103(6) (2008) 606-614.
[24] A. Daiber, N. Xia, S. Steven, M. Oelze, A. Hanf, S. Kröller-Schön, T. Münzel, H. Li, New therapeutic implications of endothelial nitric oxide synthase (eNOS) function/dysfunction in cardiovascular disease, International journal of molecular sciences 20(1) (2019) 187.
[25] H. Strijdom, N. Chamane, A. Lochner, Nitric oxide in the cardiovascular system: a simple molecule with complex actions, Cardiovascular journal of Africa 20(5) (2009) 303-310.
[26] J. Yang, J.W. Clark, R.M. Bryan, C.S. Robertson, Mathematical modeling of the nitric oxide/cGMP pathway in the vascular smooth muscle cell, American Journal of Physiology-Heart and Circulatory Physiology 289(2) (2005) H886-H897.
[27] C.K.B. Ferrari, E. Luzia França, A.C. Honorio-França, Nitric oxide, health and disease, Journal of Applied Biomedicine 7(4) (2009) 163-173.
[28] M. Carlstrom, M. Montenegro, Therapeutic value of stimulating the nitrate-nitrite-nitric oxide pathway to attenuate oxidative stress and restore nitric oxide bioavailability in cardiorenal disease, Journal of internal medicine 285(1) (2019) 2-18.
[29] S.J. Wimalawansa, Rationale for using nitric oxide donor therapy for prevention of bone loss and treatment of osteoporosis in humans, Annals of the New York Academy of Sciences 1117(1) (2007) 283-297.
[30] S. Corbett, M. Hukkanen, J. Batten, I. McCarthy, J. Polak, S. Hughes, Nitric oxide in fracture repair: Differential localisation, expression and activity of nitric oxide synthases, The Journal of Bone and Joint Surgery. British volume 81(3) (1999) 531-537.
[31] S.J. Wimalawansa, Nitric oxide: novel therapy for osteoporosis, Expert opinion on pharmacotherapy 9(17) (2008) 3025-3044.
[32] O. Hudlicka, M.D. Brown, Adaptation of skeletal muscle microvasculature to

increased or decreased blood flow: role of shear stress, nitric oxide and vascular endothelial growth factor, Journal of vascular research 46(5) (2009) 504-512.
[33] S. Mocellin, V. Bronte, D. Nitti, Nitric oxide, a double edged sword in cancer biology: searching for therapeutic opportunities, Medicinal research reviews 27(3) (2007) 317-352.
[34] S.-C. Wu, C.-Y. Lu, Y.-L. Chen, F.-C. Lo, T.-Y. Wang, Y.-J. Chen, S.-S. Yuan, W.-F. Liaw, Y.-M. Wang, Water-soluble dinitrosyl iron complex (DNIC): a nitric oxide vehicle triggering cancer cell death via apoptosis, Inorganic Chemistry 55(18) (2016) 9383-9392.
[35] D. Hirst, T. Robson, Nitric oxide in cancer therapeutics: interaction with cytotoxic chemotherapy, Current pharmaceutical design 16(4) (2010) 411-420.
[36] M.J. Malone-Povolny, S.E. Maloney, M.H. Schoenfisch, Nitric oxide therapy for diabetic wound healing, Advanced healthcare materials 8(12) (2019) 1801210.
[37] S. Frank, H. Kämpfer, C. Wetzler, J. Pfeilschifter, Nitric oxide drives skin repair: novel functions of an established mediator, Kidney international 61(3) (2002) 882-888.
[38] M.C. Jen, M.C. Serrano, R. Van Lith, G.A. Ameer, Polymer-based nitric oxide therapies: Recent insights for biomedical applications, Advanced functional materials 22(2) (2012) 239-260.
[39] T. Kitano, H. Yamada, M. Kida, Y. Okada, S. Saika, M. Yoshida, Impaired healing of a cutaneous wound in an inducible nitric oxide synthase-knockout mouse, Dermatology Research and Practice 2017 (2017).
[40] D.D. Thomas, Breathing new life into nitric oxide signaling: a brief overview of the interplay between oxygen and nitric oxide, Redox biology 5 (2015) 225-233.
[41] J. Ye, J. Jiang, Z. Zhou, Z. Weng, Y. Xu, L. Liu, W. Zhang, Y. Yang, J. Luo, X. Wang, Near-Infrared Light and Upconversion Nanoparticle Defined Nitric Oxide-Based Osteoporosis Targininеeting Therapy, ACS Nano 15(8) (2021) 13692-13702.
[42] A. Koh, A.W. Carpenter, D.L. Slomberg, M.H. Schoenfisch, Nitric oxide-releasing silica nanoparticle-doped polyurethane electrospun fibers, ACS Appl Mater Interfaces 5(16) (2013) 7956-64.
[43] L.N. Dong Wang, Zeng-Ying Qiao, Dong-Bing Cheng, Jiefei Wang, Yong Zhong, Feng Bai, Hao Wang, and Hongyou Fan, Synthesis of Self-Assembled Porphyrin Nanoparticle Photosensitizers, ACS Nano 12(4) (2018) 3796-3803.
[44] C. Oliveira, S. Benfeito, C. Fernandes, F. Cagide, T. Silva, F. Borges, NO and HNO donors, nitrones, and nitroxides: Past, present, and future, Medicinal research reviews 38(4) (2018) 1159-1187.
[45] T. Yang, A.N. Zelikin, R. Chandrawati, Progress and promise of nitric oxide-releasing platforms, Advanced Science 5(6) (2018) 1701043.
[46] S. Hwang, M.E. Meyerhoff, Polyurethane with tethered copper (II)–cyclen complex: preparation, characterization and catalytic generation of nitric oxide from S-nitrosothiols, Biomaterials 29(16) (2008) 2443-2452.
[47] P.C. Ford, Photochemical delivery of nitric oxide, Nitric oxide 34 (2013) 56-64.
[48] T. Suzuki, O. Nagae, Y. Kato, H. Nakagawa, K. Fukuhara, N. Miyata, Photoinduced nitric oxide release from nitrobenzene derivatives, Journal of the American Chemical Society 127(33) (2005) 11720-11726.

[49] J.-S. Huang, L.-Y. Chuang, J.-Y. Guh, Y.-J. Huang, Effects of nitric oxide and antioxidants on advanced glycation end products-induced hypertrophic growth in human renal tubular cells, Toxicological sciences 111(1) (2009) 109-119.
[50] R. Chandrawati, J.Y. Chang, E. Reina-Torres, C. Jumeaux, J.M. Sherwood, W.D. Stamer, A.N. Zelikin, D.R. Overby, M.M. Stevens, Localized and controlled delivery of nitric oxide to the conventional outflow pathway via enzyme biocatalysis: toward therapy for glaucoma, Advanced Materials 29(16) (2017) 1604932.
[51] Z. Wang, Y. Lu, K. Qin, Y. Wu, Y. Tian, J. Wang, J. Zhang, J. Hou, Y. Cui, K. Wang, Enzyme-functionalized vascular grafts catalyze in-situ release of nitric oxide from exogenous NO prodrug, Journal of Controlled Release 210 (2015) 179-188.
[52] M. Kushwaha, J.M. Anderson, C.A. Bosworth, A. Andukuri, W.P. Minor, J.R. Lancaster Jr, P.G. Anderson, B.C. Brott, H.-W. Jun, A nitric oxide releasing, self assembled peptide amphiphile matrix that mimics native endothelium for coating implantable cardiovascular devices, Biomaterials 31(7) (2010) 1502-1508.
[53] Q. Zhao, J. Zhang, L. Song, Q. Ji, Y. Yao, Y. Cui, J. Shen, P.G. Wang, D. Kong, Polysaccharide-based biomaterials with on-demand nitric oxide releasing property regulated by enzyme catalysis, Biomaterials 34(33) (2013) 8450-8458.
[54] H. Kleinert, J. Art, A. Pautz, Regulation of the expression of inducible nitric oxide synthase, Nitric Oxide (2010) 211-267.
[55] S. McIlhenny, P. Zhang, T. Tulenko, J. Comeau, S. Fernandez, A. Policha, M. Ferroni, E. Faul, G. Bagameri, I. Shapiro, eNOS transfection of adipose-derived stem cells yields bioactive nitric oxide production and improved results in vascular tissue engineering, Journal of tissue engineering and regenerative medicine 9(11) (2015) 1277-1285.
[56] I. Fishbein, D.T. Guerrero, I.S. Alferiev, J.B. Foster, N.G. Minutolo, M. Chorny, A.M. Monteys, K.H. Driesbaugh, C. Nagaswami, R.J. Levy, Stent-based delivery of adeno-associated viral vectors with sustained vascular transduction and iNOS-mediated inhibition of in-stent restenosis, Gene therapy 24(11) (2017) 717-726.
[57] X. Li, H. Qiu, P. Gao, Y. Yang, Z. Yang, N. Huang, Synergetic coordination and catecholamine chemistry for catalytic generation of nitric oxide on vascular stents, NPG Asia Materials 10(6) (2018) 482-496.
[58] Z. Yang, Y. Yang, L. Zhang, K. Xiong, X. Li, F. Zhang, J. Wang, X. Zhao, N. Huang, Mussel-inspired catalytic selenocystamine-dopamine coatings for long-term generation of therapeutic gas on cardiovascular stents, Biomaterials 178 (2018) 1-10.
[59] F. Zhang, Q. Zhang, X. Li, N. Huang, X. Zhao, Z. Yang, Mussel-inspired dopamine-CuII coatings for sustained in situ generation of nitric oxide for prevention of stent thrombosis and restenosis, Biomaterials 194 (2019) 117-129.
[60] J. Pant, M.J. Goudie, S.P. Hopkins, E.J. Brisbois, H. Handa, Tunable nitric oxide release from S-nitroso-N-acetylpenicillamine via catalytic copper nanoparticles for biomedical applications, ACS applied materials & interfaces 9(18) (2017) 15254-15264.
[61] A. Mondal, M. Douglass, S.P. Hopkins, P. Singha, M. Tran, H. Handa, E.J. Brisbois, Multifunctional S-Nitroso-N-acetylpenicillamine-incorporated medical-grade polymer with selenium interface for biomedical applications, ACS applied materials & interfaces 11(38) (2019) 34652-34662.

[62] Y. Yang, P. Gao, J. Wang, Q. Tu, L. Bai, K. Xiong, H. Qiu, X. Zhao, M.F. Maitz, H. Wang, Endothelium-mimicking multifunctional coating modified cardiovascular stents via a stepwise metal-catechol-(amine) surface engineering strategy, Research 2020 (2020).
[63] M.A. Elnaggar, S.H. Seo, S. Gobaa, K.S. Lim, I.H. Bae, M.H. Jeong, D.K. Han, Y.K. Joung, Nitric Oxide Releasing Coronary Stent: A New Approach Using Layer-by-Layer Coating and Liposomal Encapsulation, Small 12(43) (2016) 6012-6023.
[64] Y. Chen, P. Gao, L. Huang, X. Tan, N. Zhou, T. Yang, H. Qiu, X. Dai, S. Michael, Q. Tu, A tough nitric oxide-eluting hydrogel coating suppresses neointimal hyperplasia on vascular stent, Nature communications 12(1) (2021) 7079.
[65] X. Zhang, J. Chen, B.C. Brott, P.G. Anderson, P.T. Hwang, J. Sherwood, G. Huskin, Y.-s. Yoon, R. Virmani, H.-W. Jun, Pro-Healing Nanomatrix-Coated Stent Analysis in an In Vitro Vascular Double-Layer System and in a Rabbit Model, ACS Applied Materials & Interfaces 14(46) (2022) 51728-51743.
[66] Y. Yang, T. Xu, Q. Zhang, Y. Piao, H.P. Bei, X. Zhao, Biomimetic, stiff, and adhesive periosteum with osteogenic–angiogenic coupling effect for bone regeneration, Small 17(14) (2021) 2006598.
[67] J.K. Lee, D.S. Kim, S.Y. Park, S.W. Baek, J.W. Jung, T.H. Kim, D.K. Han, Nitric Oxide-Releasing Bioinspired Scaffold for Exquisite Regeneration of Osteoporotic Bone via Regulation of Homeostasis, Advanced Science 10(6) (2023) 2205336.
[68] Q. Yang, H. Yin, T. Xu, D. Zhu, J. Yin, Y. Chen, X. Yu, J. Gao, C. Zhang, Y. Chen, Engineering 2D mesoporous Silica@ MXene-integrated 3D-printing scaffolds for combinatory osteosarcoma therapy and NO-augmented bone regeneration, Small 16(14) (2020) 1906814.
[69] M. Li, J. Li, J. Chen, Y. Liu, X. Cheng, F. Yang, N. Gu, Platelet membrane biomimetic magnetic nanocarriers for targinineeted delivery and in situ generation of nitric oxide in early ischemic stroke, ACS nano 14(2) (2020) 2024-2035.
[70] H. Li, J. Yan, D. Meng, R. Cai, X. Gao, Y. Ji, L. Wang, C. Chen, X. Wu, Gold nanorod-based nanoplatform catalyzes constant NO generation and protects from cardiovascular injury, ACS nano 14(10) (2020) 12854-12865.
[71] P. Joseph, D. Leong, M. McKee, S.S. Anand, J.-D. Schwalm, K. Teo, A. Mente, S. Yusuf, Reducing the global burden of cardiovascular disease, part 1: the epidemiology and risk factors, Circulation research 121(6) (2017) 677-694.
[72] T.R. Frieden, M.G. Jaffe, Saving 100 million lives by improving global treatment of hypertension and reducing cardiovascular disease risk factors, The Journal of Clinical Hypertension 20(2) (2018) 208.
[73] T. Dave, J. Ezhilan, H. Vasnawala, V. Somani, Plaque regression and plaque stabilisation in cardiovascular diseases, Indian journal of endocrinology and metabolism 17(6) (2013) 983.
[74] J. Mehilli, J. Pache, M. Abdel-Wahab, S. Schulz, R.A. Byrne, K. Tiroch, J. Hausleiter, M. Seyfarth, I. Ott, T. Ibrahim, Drug-eluting versus bare-metal stents in saphenous vein graft lesions (ISAR-CABG): a randomised controlled superiority trial, The Lancet 378(9796) (2011) 1071-1078.
[75] K. Lo, C. Chan, Characteristics and outcomes of patients with percutaneous

coronary intervention for unprotected left main coronary artery disease: a Hong Kong experience, Hong Kong Med J 20(3) (2014) 187-93.
[76] R. Sethi, C.H. LEE, Endothelial progenitor cell capture stent: safety and effectiveness, Journal of interventional cardiology 25(5) (2012) 493-500.
[77] R. Simon-Walker, R. Romero, J.M. Staver, Y. Zang, M.M. Reynolds, K.C. Popat, M.J. Kipper, Glycocalyx-inspired nitric oxide-releasing surfaces reduce platelet adhesion and activation on titanium, ACS Biomaterials Science & Engineering 3(1) (2017) 68-77.
[78] S. Hauser, F. Jung, J. Pietzsch, Human endothelial cell models in biomaterial research, Trends in Biotechnology 35(3) (2017) 265-277.
[79] D.J. Suchyta, H. Handa, M.E. Meyerhoff, A nitric oxide-releasing heparinarin conjugate for delivery of a combined antiplatelet/anticoagulant agent, Molecular pharmaceutics 11(2) (2014) 645-650.
[80] B. Wu, B. Gerlitz, B.W. Grinnell, M.E. Meyerhoff, Polymeric coatings that mimic the endothelium: combining nitric oxide release with surface-bound active thrombomodulin and heparinarin, Biomaterials 28(28) (2007) 4047-4055.
[81] T. Yang, Z. Du, H. Qiu, P. Gao, X. Zhao, H. Wang, Q. Tu, K. Xiong, N. Huang, Z. Yang, From surface to bulk modification: plasma polymerization of amine-bearing coating by synergic strategy of biomolecule grafting and nitric oxide loading, Bioactive materials 5(1) (2020) 17-25.
[82] S. Yuan, C.G. Kevil, Nitric oxide and hydrogen sulfide regulation of ischemic vascular remodeling, Microcirculation 23(2) (2016) 134-145.
[83] Q. Tu, X. Zhao, S. Liu, X. Li, Q. Zhang, H. Yu, K. Xiong, N. Huang, Z. Yang, Spatiotemporal dual-delivery of therapeutic gas and growth factor for prevention of vascular stent thrombosis and restenosis, Applied Materials Today 19 (2020) 100546.
[84] Q. Tu, X. Shen, Y. Liu, Q. Zhang, X. Zhao, M.F. Maitz, T. Liu, H. Qiu, J. Wang, N. Huang, A facile metal–phenolic–amine strategy for dual-functionalization of blood-contacting devices with antibacterial and anticoagulant properties, Materials Chemistry Frontiers 3(2) (2019) 265-275.
[85] C. Heiss, T. Lauer, A. Dejam, P. Kleinbongard, S. Hamada, T. Rassaf, S. Matern, M. Feelisch, M. Kelm, Plasma nitroso compounds are decreased in patients with endothelial dysfunction, Journal of the American College of Cardiology 47(3) (2006) 573-579.
[86] C. Gaucher, A. Boudier, F. Dahboul, M. Parent, P. Leroy, S-nitrosation/denitrosation in cardiovascular pathologies: facts and concepts for the rational design of S-nitrosothiols, Current pharmaceutical design 19(3) (2013) 458-472.
[87] L. Liu, Y. Yan, M. Zeng, J. Zhang, M.A. Hanes, G. Ahearn, T.J. McMahon, T. Dickfeld, H.E. Marshall, L.G. Que, Essential roles of S-nitrosothiols in vascular homeostasis and endotoxic shock, Cell 116(4) (2004) 617-628.
[88] B. Zhang, R. Yao, C. Hu, M.F. Maitz, H. Wu, K. Liu, L. Yang, R. Luo, Y. Wang, Epigallocatechin gallate mediated sandwich-like coating for mimicking endothelium with sustained therapeutic nitric oxide generation and heparinarin release, Biomaterials 269 (2021) 120418.
[89] N. Lyu, Z. Du, H. Qiu, P. Gao, Q. Yao, K. Xiong, Q. Tu, X. Li, B. Chen, M. Wang,

Mimicking the Nitric Oxide-Releasing and Glycocalyx Functions of Endothelium on Vascular Stent Surfaces, Advanced Science 7(21) (2020) 2002330.
[90] L. Wen, S. Feil, M. Wolters, M. Thunemann, F. Regler, K. Schmidt, A. Friebe, M. Olbrich, H. Langer, M. Gawaz, A shear-dependent NO-cGMP-cGKI cascade in platelets acts as an auto-regulatory brake of thrombosis, Nature communications 9(1) (2018) 4301.
[91] M. Thunemann, K. Schmidt, C. de Wit, X. Han, R.K. Jain, D. Fukumura, R. Feil, Correlative intravital imaging of cGMP signals and vasodilation in mice, Frontiers in physiology 5 (2014) 394.
[92] H. Wu, Q. He, L. Li, L. Li, Z. Zhou, N. Chen, M. Yang, Q. Luo, B. Zhang, R. Luo, A facile and versatile superhydrophilic coating on biodegradable PLA stent with stepwise assembly of metal/phenolic networks for mimicking endothelium function, Chemical Engineering Journal 427 (2022) 130932.
[93] D. Wang, Y. Xu, L. Wang, X. Wang, S. Yan, G. Yilmaz, Q. Li, L.-S. Turng, Long-term nitric oxide release for rapid endothelialization in expanded polytetrafluoroethylene small-diameter artificial blood vessel grafts, Applied Surface Science 507 (2020) 145028.
[94] R. Luo, J. Zhang, W. Zhuang, L. Deng, L. Li, H. Yu, J. Wang, N. Huang, Y. Wang, Multifunctional coatings that mimic the endothelium: surface bound active heparinarin nanoparticles with in situ generation of nitric oxide from nitrosothiols, Journal of Materials Chemistry B 6(35) (2018) 5582-5595.
[95] H. Qiu, P. Qi, J. Liu, Y. Yang, X. Tan, Y. Xiao, M.F. Maitz, N. Huang, Z. Yang, Biomimetic engineering endothelium-like coating on cardiovascular stent through heparinarin and nitric oxide-generating compound synergistic modification strategy, Biomaterials 207 (2019) 10-22.
[96] D. Suo, J. Rao, H. Wang, Z. Zhang, P.H.-M. Leung, H. Zhang, X. Tao, X. Zhao, A universal biocompatible coating for enhanced lubrication and bacterial inhibition, Biomaterials Science 10(13) (2022) 3493-3502.
[97] H. Yu, S. Yu, H. Qiu, P. Gao, Y. Chen, X. Zhao, Q. Tu, M. Zhou, L. Cai, N. Huang, Nitric oxide-generating compound and bio-clickable peptide mimic for synergistically tailoring surface anti-thrombogenic and anti-microbial dual-functions, Bioactive Materials 6(6) (2021) 1618-1627.
[98] H. Yu, H. Qiu, W. Ma, M.F. Maitz, Q. Tu, K. Xiong, J. Chen, N. Huang, Z. Yang, Endothelium-Mimicking Surface Combats Thrombosis and Biofouling via Synergistic Long-and Short-Distance Defense Strategy, Small 17(24) (2021) 2100729.
[99] X. Li, J. Liu, T. Yang, H. Qiu, L. Lu, Q. Tu, K. Xiong, N. Huang, Z. Yang, Mussel-inspired “built-up” surface chemistry for combining nitric oxide catalytic and vascular cell selective properties, Biomaterials 241 (2020) 119904.
[100] T. Xia, W. Guan, J. Fu, X. Zou, Y. Han, C. Chen, L. Zhou, C. Zeng, W.E. Wang, Tirofiban induces vasorelaxation of the coronary artery via an endothelium-dependent NO-cGMP signaling by activating the PI3K/Akt/eNOS pathway, Biochemical And Biophysical Research Communications 474(3) (2016) 599-605.
[101] J.-l. Wang, B.-c. Li, Z.-j. Li, K.-f. Ren, L.-j. Jin, S.-m. Zhang, H. Chang, Y.-x. Sun, J. Ji, Electropolymerization of dopamine for surface modification of complex-

shaped cardiovascular stents, Biomaterials 35(27) (2014) 7679-7689.
[102] J. Yang, Y. Zeng, C. Zhang, Y.-X. Chen, Z. Yang, Y. Li, X. Leng, D. Kong, X.-Q. Wei, H.-F. Sun, The prevention of restenosis in vivo with a VEGF gene and paclitaxel co-eluting stent, Biomaterials 34(6) (2013) 1635-1643.
[103] M. Alagem-Shafir, E. Kivovich, I. Tzchori, N. Lanir, M. Falah, M. Flugelman, U. Dinnar, R. Beyar, N. Lotan, S. Sivan, The formation of an anti-restenotic/anti-thrombotic surface by immobilization of nitric oxide synthase on a metallic carrier, Acta Biomaterialia 10(5) (2014) 2304-2312.
[104] Z. Yang, X. Zhao, R. Hao, Q. Tu, X. Tian, Y. Xiao, K. Xiong, M. Wang, Y. Feng, N. Huang, Bioclickable and mussel adhesive peptide mimics for engineering vascular stent surfaces, Proceedings of the National Academy of Sciences 117(28) (2020) 16127-16137.
[105] Z. Yang, Q. Tu, J. Wang, N. Huang, The role of heparinarin binding surfaces in the direction of endothelial and smooth muscle cell fate and re-endothelialization, Biomaterials 33(28) (2012) 6615-6625.
[106] J.S. Pober, W.C. Sessa, Evolving functions of endothelial cells in inflammation, Nature Reviews Immunology 7(10) (2007) 803-815.
[107] P. Gresele, S. Momi, G. Guglielmini, Nitric oxide-enhancing or-releasing agents as antithrombotic drugs, Biochemical pharmacology 166 (2019) 300-312.
[108] P.A. Cahill, E.M. Redmond, Vascular endothelium–gatekeeper of vessel health, Atherosclerosis 248 (2016) 97-109.
[109] M.S. Kim, L.S. Dean, In-stent restenosis, Cardiovascular therapeutics 29(3) (2011) 190-198.
[110] H. Chang, K.-f. Ren, J.-l. Wang, H. Zhang, B.-l. Wang, S.-m. Zheng, Y.-y. Zhou, J. Ji, Surface-mediated functional gene delivery: An effective strategy for enhancing competitiveness of endothelial cells over smooth muscle cells, Biomaterials 34(13) (2013) 3345-3354.
[111] T.R. Roberts, M.R. Garren, S.N. Wilson, H. Handa, A.I. Batchinsky, Development and In vitro whole blood hemocompatibility screening of endothelium-mimetic multifunctional coatings, ACS applied bio materials 5(5) (2022) 2212-2223.
[112] R. Devine, M.J. Goudie, P. Singha, C. Schmiedt, M. Douglass, E.J. Brisbois, H. Handa, Mimicking the endothelium: dual action heparinarinized nitric oxide releasing surface, ACS applied materials & interfaces 12(18) (2020) 20158-20171.
[113] Z. Zhou, M.E. Meyerhoff, Preparation and characterization of polymeric coatings with combined nitric oxide release and immobilized active heparinarin, Biomaterials 26(33) (2005) 6506-6517.
[114] J.M. Walenga, W.P. Jeske, J. Fareed, Short-and long-acting synthetic pentasaccharides as antithrombotic agents, Expert Opinion on Investigational Drugs 14(7) (2005) 847-858.
[115] K.-S. Park, S.N. Kang, D.H. Kim, H.-B. Kim, K.S. Im, W. Park, Y.J. Hong, D.K. Han, Y.K. Joung, Late endothelial progenitor cell-capture stents with CD146 antibody and nanostructure reduce in-stent restenosis and thrombosis, Acta biomaterialia 111 (2020) 91-101.
[116] Y. Yang, X. Li, H. Qiu, P. Li, P. Qi, M.F. Maitz, T. You, R. Shen, Z. Yang, W. Tian,

Polydopamine modified TiO2 nanotube arrays for long-term controlled elution of bivalirudin and improved hemocompatibility, ACS applied materials & interfaces 10(9) (2017) 7649-7660.
[117] C. Chaabane, F. Otsuka, R. Virmani, M.-L. Bochaton-Piallat, Biological responses in stented arteries, Cardiovascular research 99(2) (2013) 353-363.
[118] C. Liang, Y. Hu, H. Wang, D. Xia, Q. Li, J. Zhang, J. Yang, B. Li, H. Li, D. Han, Biomimetic cardiovascular stents for in vivo re-endothelialization, Biomaterials 103 (2016) 170-182.
[119] M. Joner, A.V. Finn, A. Farb, E.K. Mont, F.D. Kolodgie, E. Ladich, R. Kutys, K. Skorija, H.K. Gold, R. Virmani, Pathology of drug-eluting stents in humans: delayed healing and late thrombotic risk, Journal of the American College of Cardiology 48(1) (2006) 193-202.
[120] C.C. Mohan, A.M. Cherian, S. Kurup, J. Joseph, M.B. Nair, M. Vijayakumar, S.V. Nair, D. Menon, Stable titania nanostructures on stainless steel coronary stent surface for enhanced corrosion resistance and endothelialization, Advanced Healthcare Materials 6(11) (2017) 1601353.
[121] S. Weinbaum, J.M. Tarbell, E.R. Damiano, The structure and function of the endothelial glycocalyx layer, Annu. Rev. Biomed. Eng. 9 (2007) 121-167.
[122] A. de Mel, G. Jell, M.M. Stevens, A.M. Seifalian, Biofunctionalization of biomaterials for accelerated in situ endothelialization: a review, Biomacromolecules 9(11) (2008) 2969-2979.
[123] M. Yin, Y. Yuan, C. Liu, J. Wang, Development of mussel adhesive polypeptide mimics coating for in-situ inducing re-endothelialization of intravascular stent devices, Biomaterials 30(14) (2009) 2764-2773.
[124] G. Li, P. Yang, W. Qin, M.F. Maitz, S. Zhou, N. Huang, The effect of coimmobilizing heparinarin and fibronectin on titanium on hemocompatibility and endothelialization, Biomaterials 32(21) (2011) 4691-4703.
[125] T.R. Carlson, Y. Feng, P.C. Maisonpierre, M. Mrksich, A.O. Morla, Direct cell adhesion to the angiopoietins mediated by integrins, Journal of Biological Chemistry 276(28) (2001) 26516-26525.
[126] H. Hutchings, N. Ortega, J. Plouët, Extracellular matrix-bound vascular endothelial growth factor promotes endothelial cell adhesion, migration, and survival through integrin ligation, The FASEB Journal 17(11) (2003) 1-27.
[127] X. Wu, Y. Zhao, C. Tang, T. Yin, R. Du, J. Tian, J. Huang, H. Gregersen, G. Wang, Re-endothelialization study on endovascular stents seeded by endothelial cells through up-or downregulation of VEGF, ACS applied materials & interfaces 8(11) (2016) 7578-7589.
[128] X. Wang, X. Fu, S. Zhao, X. Fu, H. Zhang, L. Shao, G. Li, C. Fan, Antiangiogenic properties of caudatin in vitro and in vivo by suppression of VEGF-VEGFR2-AKT/FAK signal axis, Molecular medicine reports 16(6) (2017) 8937-8943.
[129] S. Sinha, S. Khan, S. Shukla, A.D. Lakra, S. Kumar, G. Das, R. Maurya, S.M. Meeran, Cucurbitacin B inhibits breast cancer metastasis and angiogenesis through VEGF-mediated suppression of FAK/MMP-9 signaling axis, The international journal

of biochemistry & cell biology 77 (2016) 41-56.
[130] Y. Deng, X. Zhang, M. Simons, Molecular controls of lymphatic VEGFR3 signaling, Arteriosclerosis, thrombosis, and vascular biology 35(2) (2015) 421-429.
[131] T. Iwasaki, Y. Takeda, K. Maruyama, Y. Yokosaki, K. Tsujino, S. Tetsumoto, H. Kuhara, K. Nakanishi, Y. Otani, Y. Jin, Deletion of tetraspanin CD9 diminishes lymphangiogenesis in vivo and in vitro, Journal of Biological Chemistry 288(4) (2013) 2118-2131.
[132] N. Tang, L. Shi, Z. Yu, P. Dong, C. Wang, X. Huo, B. Zhang, S. Huang, S. Deng, K. Liu, Gamabufotalin, a major derivative of bufadienolide, inhibits VEGF-induced angiogenesis by suppressing VEGFR-2 signaling pathway, Oncotarginineet 7(3) (2016) 3533.
[133] F. Lewis, P. Horny, P. Hale, S. Turgeon, M. Tatoulian, D. Mantovani, Study of the adhesion of thin plasma fluorocarbon coatings resisting plastic deformation for stent applications, Journal of Physics D: Applied Physics 41(4) (2008) 045310.
[134] S. Jana, Endothelialization of cardiovascular devices, Acta biomaterialia 99 (2019) 53-71.
[135] C.K. Poh, Z. Shi, T.Y. Lim, K.G. Neoh, W. Wang, The effect of VEGF functionalization of titanium on endothelial cells in vitro, Biomaterials 31(7) (2010) 1578-1585.
[136] Y.M. Shin, Y.B. Lee, S.J. Kim, J.K. Kang, J.-C. Park, W. Jang, H. Shin, Mussel-inspired immobilization of vascular endothelial growth factor (VEGF) for enhanced endothelialization of vascular grafts, Biomacromolecules 13(7) (2012) 2020-2028.
[137] X. Wu, Y. Yin, Y. Liu, X. Liu, Z. Liu, T. Li, R. Huang, Z. Ruan, Z. Deng, Effect of dietary arginineinine and N-carbamoylglutamate supplementation on reproduction and gene expression of eNOS, VEGFA and PlGF1 in placenta in late pregnancy of sows, Animal reproduction science 132(3-4) (2012) 187-192.
[138] S.H. Javanmard, M. Nematbakhsh, F. Mahmoodi, M.R. Mohajeri, l-Arginineinine supplementation enhances eNOS expression in experimental model of hypercholesterolemic rabbits aorta, Pathophysiology 16(1) (2009) 9-13.
[139] C. Gao, W.T. Sow, Y. Wang, Y. Wang, D. Yang, B.H. Lee, D. Matičić, L. Fang, H. Li, C. Zhang, Hydrogel composite scaffolds with an attenuated immunogenicity component for bone tissue engineering applications, Journal of Materials Chemistry B 9(8) (2021) 2033-2041.
[140] L. Claes, S. Recknagel, A. Ignatius, Fracture healing under healthy and inflammatory conditions, Nature Reviews Rheumatology 8(3) (2012) 133-143.
[141] M. Thomas, D. Puleo, Infection, inflammation, and bone regeneration: a paradoxical relationship, Journal of dental research 90(9) (2011) 1052-1061.
[142] Y. Zeng, Z. Pan, J. Yuan, Y. Song, Z. Feng, Z. Chen, Z. Ye, Y. Li, Y. Bao, Z. Ran, Inhibiting Osteolytic Breast Cancer Bone Metastasis by Bone-Targinineeted Nanoagent via Remodeling the Bone Tumor Microenvironment Combined with NIR-II Photothermal Therapy, Small (2023) 2301003.
[143] W. Wang, K.W. Yeung, Bone grafts and biomaterials substitutes for bone defect repair: A review, Bioactive materials 2(4) (2017) 224-247.
[144] H. Shegarfi, O. Reikeras, Bone transplantation and immune response, Journal of

Orthopaedic Surgery 17(2) (2009) 206-211.
[145] R. Zamborsky, A. Svec, M. Bohac, M. Kilian, M. Kokavec, Infection in bone allograft transplants, Exp Clin Transplant 14(5) (2016) 484-490.
[146] M.J. Javid-Naderi, J. Behravan, N. Karimi-Hajishohreh, S. Toosi, Synthetic polymers as bone engineering scaffold, Polymers for Advanced Technologies (2023).
[147] X. Wang, S. Xu, S. Zhou, W. Xu, M. Leary, P. Choong, M. Qian, M. Brandt, Y.M. Xie, Topological design and additive manufacturing of porous metals for bone scaffolds and orthopaedic implants: A review, Biomaterials 83 (2016) 127-141.
[148] Q. Fu, E. Saiz, M.N. Rahaman, A.P. Tomsia, Toward strong and tough glass and ceramic scaffolds for bone repair, Advanced functional materials 23(44) (2013) 5461-5476.
[149] F. Cui, Y. Zhang, H. Wen, X. Zhu, Microstructural evolution in external callus of human long bone, Materials Science and Engineering: C 11(1) (2000) 27-33.
[150] L. Mendes, H. Katagiri, W. Tam, Y. Chai, L. Geris, S. Roberts, F. Luyten, Advancing osteochondral tissue engineering: bone morphogenetic protein, transforming growth factor, and fibroblast growth factor signaling drive ordered differentiation of periosteal cells resulting in stable cartilage and bone formation in vivo, Stem cell research & therapy 9 (2018) 1-13.
[151] C.-J. Wang, K.D. Yang, J.-Y. Ko, C.-C. Huang, H.-Y. Huang, F.-S. Wang, The effects of shockwave on bone healing and systemic concentrations of nitric oxide (NO), TGF-β1, VEGF and BMP-2 in long bone non-unions, Nitric oxide 20(4) (2009) 298-303.
[152] L. Wu, Y. Gu, L. Liu, J. Tang, J. Mao, K. Xi, Z. Jiang, Y. Zhou, Y. Xu, L. Deng, Hierarchical micro/nanofibrous membranes of sustained releasing VEGF for periosteal regeneration, Biomaterials 227 (2020) 119555.
[153] M.K. Murphy, D.J. Huey, J.C. Hu, K.A. Athanasiou, TGF-β1, GDF-5, and BMP-2 stimulation induces chondrogenesis in expanded human articular chondrocytes and marrow-derived stromal cells, Stem cells 33(3) (2015) 762-773.
[154] Y. Yang, J. Rao, H. Liu, Z. Dong, Z. Zhang, H.-P. Bei, C. Wen, X. Zhao, Biomimicking design of artificial periosteum for promoting bone healing, Journal of Orthopaedic Translation 36 (2022) 18-32.
[155] K. Wu, B. Yu, D. Li, Y. Tian, Y. Liu, J. Jiang, Recent advances in nanoplatforms for the treatment of osteosarcoma, Frontiers in Oncology 12 (2022) 241.
[156] Q. Ji, S. Zhang, J. Zhang, Z. Wang, J. Wang, Y. Cui, L. Pang, S. Wang, D. Kong, Q. Zhao, Dual functionalization of poly (ε-caprolactone) film surface through supramolecular assembly with the aim of promoting in situ endothelial progenitor cell attachment on vascular grafts, Biomacromolecules 14(11) (2013) 4099-4107.
[157] M. Avci-Adali, G. Ziemer, H.P. Wendel, Induction of EPC homing on biofunctionalized vascular grafts for rapid in vivo self-endothelialization—a review of current strategies, Biotechnology advances 28(1) (2010) 119-129.
[158] J. Fang, J. Zhang, J. Du, Y. Pan, J. Shi, Y. Peng, W. Chen, L. Yuan, S.-H. Ye, W.R. Wagner, Orthogonally functionalizable polyurethane with subsequent modification with heparinarin and endothelium-inducing peptide aiming for vascular reconstruction, ACS Applied Materials & Interfaces 8(23) (2016) 14442-14452.

[159] S. Li, D. Sengupta, S. Chien, Vascular tissue engineering: from in vitro to in situ, Wiley Interdisciplinary Reviews: Systems Biology and Medicine 6(1) (2014) 61-76.
[160] L. Bian, M. Guvendiren, R.L. Mauck, J.A. Burdick, Hydrogels that mimic developmentally relevant matrix and N-cadherin interactions enhance MSC chondrogenesis, Proceedings of the National Academy of Sciences 110(25) (2013) 10117-10122.
[161] J.C. Vega L, M.K. Lee, J.H. Jeong, C.E. Smith, K.Y. Lee, H.J. Chung, D.E. Leckband, H. Kong, Recapitulating cell–cell adhesion using n-cadherin biologically tethered to substrates, Biomacromolecules 15(6) (2014) 2172-2179.
[162] R. Li, J. Xu, D.S.H. Wong, J. Li, P. Zhao, L. Bian, Self-assembled N-cadherin mimetic peptide hydrogels promote the chondrogenesis of mesenchymal stem cells through inhibition of canonical Wnt/β-catenin signaling, Biomaterials 145 (2017) 33-43.
[163] M. Zhu, K. Zhang, L. Feng, S. Lin, Q. Pan, L. Bian, G. Li, Surface decoration of development-inspired synthetic N-cadherin motif via Ac-BP promotes osseointegration of metal implants, Bioactive Materials 6(5) (2021) 1353-1364.
[164] Z. Dong, X. Zhao, Application of TPMS structure in bone regeneration, Engineered Regeneration 2 (2021) 154-162.
[165] Y. Yang, T. Xu, H.-P. Bei, L. Zhang, C.-Y. Tang, M. Zhang, C. Xu, L. Bian, K.W.-K. Yeung, J.Y.H. Fuh, Gaussian curvature–driven direction of cell fate toward osteogenesis with triply periodic minimal surface scaffolds, Proceedings of the National Academy of Sciences 119(41) (2022) e2206684119.
[166] Z. Wang, H.W. An, D. Hou, M. Wang, X. Zeng, R. Zheng, L. Wang, K. Wang, H. Wang, W. Xu, Addressable peptide self-assembly on the cancer cell membrane for sensitizing chemotherapy of renal cell carcinoma, Advanced Materials 31(11) (2019) 1807175.
[167] H. Qi, K. Wang, M. Li, Y. Zhang, K. Dong, S. Heise, A.R. Boccaccini, T. Lu, Co-culture of BMSCs and HUVECs with simvastatin-loaded gelatin nanosphere/chitosan coating on Mg alloy for osteogenic differentiation and vasculogenesis, International Journal of Biological Macromolecules 193 (2021).
[168] X. Huang, C. Li, B. Zhu, H. Wang, X. Luo, L. Wei, Co-cultured h BMSC s and HUVEC s on human bio-derived bone scaffolds provide support for the long-term ex vivo culture of HSC/HPC s, Journal of biomedical materials research Part A 104(5) (2016) 1221-1230.
[169] L. Liu, Y. Liu, C. Feng, J. Chang, R. Fu, T. Wu, F. Yu, X. Wang, L. Xia, C. Wu, Lithium-containing biomaterials stimulate bone marrow stromal cell-derived exosomal miR-130a secretion to promote angiogenesis, Biomaterials 192 (2019) 523-536.
[170] Y. Wang, W. Cui, X. Zhao, S. Wen, Y. Sun, J. Han, H. Zhang, Bone remodeling-inspired dual delivery electrospun nanofibers for promoting bone regeneration, Nanoscale 11(1) (2019) 60-71.
[171] X. Zhao, Q. Lang, L. Yildirimer, Z.Y. Lin, W. Cui, N. Annabi, K.W. Ng, M.R. Dokmeci, A.M. Ghaemmaghami, A. Khademhosseini, Photocrosslinkable gelatin hydrogel for epidermal tissue engineering, Advanced healthcare materials 5(1) (2016) 108-118.

[172] X. Zhao, S. Liu, L. Yildirimer, H. Zhao, R. Ding, H. Wang, W. Cui, D. Weitz, Injectable stem cell-laden photocrosslinkable microspheres fabricated using microfluidics for rapid generation of osteogenic tissue constructs, Advanced Functional Materials 26(17) (2016) 2809-2819.
[173] Y. Yang, Q. Zhang, T. Xu, H. Zhang, M. Zhang, L. Lu, Y. Hao, J.H. Fuh, X. Zhao, Photocrosslinkable nanocomposite ink for printing strong, biodegradable and bioactive bone graft, Biomaterials 263 (2020) 120378.
[174] X. Zhao, S. Jiang, S. Liu, S. Chen, Z.Y.W. Lin, G. Pan, F. He, F. Li, C. Fan, W. Cui, Optimization of intrinsic and extrinsic tendon healing through controllable water-soluble mitomycin-C release from electrospun fibers by mediating adhesion-related gene expression, Biomaterials 61 (2015) 61-74.
[175] X. Sun, Q. Lang, H. Zhang, L. Cheng, Y. Zhang, G. Pan, X. Zhao, H. Yang, Y. Zhang, H.A. Santos, Electrospun photocrosslinkable hydrogel fibrous scaffolds for rapid in vivo vascularized skin flap regeneration, Advanced Functional Materials 27(2) (2017) 1604617.
[176] T.X. Yuhe Yang, Ho Pan Bei, Yuanjin Zhao, Xin Zhao, Sculpting Bio-Inspired Surface Textures: An Adhesive Janus Periosteum, Advanced Functional Materials 31(37) 2104636.
[177] T. Xu, Y. Yang, D. Suo, H.P. Bei, X. Xu, X. Zhao, Electrosprayed Regeneration-Enhancer-Element Microspheres Power Osteogenesis and Angiogenesis Coupling, Small 18(36) (2022) 2200314.
[178] Y.H. Choi, S.-H. Kim, I.-S. Kim, K. Kim, S.K. Kwon, N.S. Hwang, Gelatin-based micro-hydrogel carrying genetically engineered human endothelial cells for neovascularization, Acta Biomaterialia 95 (2019) 285-296.
[179] H.-w. Cheng, K.D. Luk, K.M. Cheung, B.P. Chan, In vitro generation of an osteochondral interface from mesenchymal stem cell–collagen microspheres, Biomaterials 32(6) (2011) 1526-1535.
[180] C. Sonnet, C.L. Simpson, R.M. Olabisi, K. Sullivan, Z. Lazard, Z. Gugala, J.F. Peroni, J.M. Weh, A.R. Davis, J.L. West, Rapid healing of femoral defects in rats with low dose sustained BMP2 expression from PEGDA hydrogel microspheres, Journal of orthopaedic research 31(10) (2013) 1597-1604.
[181] A. Oryan, A. Kamali, A. Moshiri, M. Baghaban Eslaminejad, Role of mesenchymal stem cells in bone regenerative medicine: what is the evidence?, Cells Tissues Organs 204(2) (2017) 59-83.
[182] S.-C. Huo, B. Yue, Approaches to promoting bone marrow mesenchymal stem cell osteogenesis on orthopedic implant surface, World Journal of Stem Cells 12(7) (2020) 545.
[183] C.F. Lai, S.L. Cheng, G. Mbalaviele, C. Donsante, M. Watkins, G.L. Radice, R. Civitelli, Accentuated ovariectomy-induced bone loss and altered osteogenesis in heterozygous N-cadherin null mice, Journal of Bone and Mineral Research 21(12) (2006) 1897-1906.
[184] C. Hoemann, H. El-Gabalawy, M. McKee, In vitro osteogenesis assays: influence of the primary cell source on alkaline phosphatase activity and mineralization, Pathologie Biologie 57(4) (2009) 318-323.

[185] M.T. Tsai, W.J. Li, R.S. Tuan, W.H. Chang, Modulation of osteogenesis in human mesenchymal stem cells by specific pulsed electromagnetic field stimulation, Journal of orthopaedic research 27(9) (2009) 1169-1174.
[186] Z. Cao, H. Wang, J. Chen, Y. Zhang, Q. Mo, P. Zhang, M. Wang, H. Liu, X. Bao, Y. Sun, Silk-based hydrogel incorporated with metal-organic framework nanozymes for enhanced osteochondral regeneration, Bioactive Materials 20 (2023) 221-242.
[187] T. Wu, X. Zhang, Y. Liu, C. Cui, Y. Sun, W. Liu, Wet adhesive hydrogel cardiac patch loaded with anti-oxidative, autophagy-regulating molecule capsules and MSCs for restoring infarcted myocardium, Bioactive Materials 21 (2023) 20-31.
[188] C. Maes, T. Kobayashi, M.K. Selig, S. Torrekens, S.I. Roth, S. Mackem, G. Carmeliet, H.M. Kronenberg, Osteoblast precursors, but not mature osteoblasts, move into developing and fractured bones along with invading blood vessels, Developmental cell 19(2) (2010) 329-344.
[189] S. Portal Núñez, D. Lozano, P. Esbrit, Role of angiogenesis on bone formation, (2012).
[190] S.L. Calzi, M.B. Neu, L.C. Shaw, J.L. Kielczewski, N.I. Moldovan, M.B. Grant, EPCs and pathological angiogenesis: when good cells go bad, Microvascular research 79(3) (2010) 207-216.
[191] J. Rouwkema, P.E. Westerweel, J. De Boer, M.C. Verhaar, C.A. Van Blitterswijk, The use of endothelial progenitor cells for prevascularized bone tissue engineering, Tissue Engineering Part A 15(8) (2009) 2015-2027.
[192] Y. Miao, Y. Chen, J. Luo, X. Liu, Q. Yang, X. Shi, Y. Wang, Black phosphorus nanosheets-enabled DNA hydrogel integrating 3D-printed scaffold for promoting vascularized bone regeneration, Bioactive Materials 21 (2023) 97-109.
[193] X. Wei, W. Zhou, Z. Tang, H. Wu, Y. Liu, H. Dong, N. Wang, H. Huang, S. Bao, L. Shi, Magnesium surface-activated 3D printed porous PEEK scaffolds for in vivo osseointegration by promoting angiogenesis and osteogenesis, Bioactive Materials 20 (2023) 16-28.
[194] L. Li, Q. Li, L. Gui, Y. Deng, L. Wang, J. Jiao, Y. Hu, X. Lan, J. Hou, Y. Li, Sequential gastrodin release PU/n-HA composite scaffolds reprogram macrophages for improved osteogenesis and angiogenesis, Bioactive Materials 19 (2023) 24-37.
[195] M. Grellier, L. Bordenave, J. Amedee, Cell-to-cell communication between osteogenic and endothelial lineages: implications for tissue engineering, Trends in biotechnology 27(10) (2009) 562-571.
[196] H. Matsubara, D.E. Hogan, E.F. Morgan, D.P. Mortlock, T.A. Einhorn, L.C. Gerstenfeld, Vascular tissues are a primary source of BMP2 expression during bone formation induced by distraction osteogenesis, Bone 51(1) (2012) 168-180.
[197] K.W. Hongfei Qi, Meng Li, Yanni Zhang, Kai Dong, Svenja Heise, Aldo R. Boccaccini, Tingli Lu, Co-culture of BMSCs and HUVECs with simvastatin-loaded gelatin nanosphere/chitosan coating on Mg alloy for osteogenic differentiation and vasculogenesis, International Journal of Biological Macromolecules 193 2021-2028.
[198] U. Bulnheim, P. Müller, H.G. Neumann, K. Peters, R.E. Unger, C.J. Kirkpatrick, J. Rychly, Endothelial cells stimulate osteogenic differentiation of mesenchymal stem cells on calcium phosphate scaffolds, Journal of Tissue Engineering and Regenerative

Medicine 8(10) (2014) 831-840.
[199] H. Li, K. Xue, N. Kong, K. Liu, J. Chang, Silicate bioceramics enhanced vascularization and osteogenesis through stimulating interactions between endothelia cells and bone marrow stromal cells, Biomaterials 35(12) (2014) 3803-3818.
[200] J. He, X. Han, S. Wang, Y. Zhang, X. Dai, B. Liu, L. Liu, X. Zhao, Cell sheets of co-cultured BMP-2-modified bone marrow stromal cells and endothelial progenitor cells accelerate bone regeneration in vitro, Experimental and Therapeutic Medicine 18(5) (2019) 3333-3340.
[201] J. Lv, P. Xiu, J. Tan, Z. Jia, H. Cai, Z. Liu, Enhanced angiogenesis and osteogenesis in critical bone defects by the controlled release of BMP-2 and VEGF: implantation of electron beam melting-fabricated porous Ti6Al4V scaffolds incorporating growth factor-doped fibrin glue, Biomedical materials 10(3) (2015) 035013.
[202] S.M. Nassiri, R. Rahbargininehazi, Interactions of mesenchymal stem cells with endothelial cells, Stem cells and development 23(4) (2014) 319-332.
[203] J.E. Won, W.J. Kim, J.S. Shim, J.J. Ryu, Guided Bone Regeneration with a Nitric-Oxide Releasing Polymer Inducing Angiogenesis and Osteogenesis in Critical-Sized Bone Defects, Macromolecular Bioscience 22(10) (2022) 2200162.
[204] Y. Li, Q. Pan, N. Zhang, B. Wang, Z. Yang, J.T. Ryaby, E.I. Waldorff, W.Y.-W. Lee, G. Li, A novel pulsed electromagnetic field promotes distraction osteogenesis via enhancing osteogenesis and angiogenesis in a rat model, Journal of Orthopaedic Translation 25 (2020) 87-95.